Structure-Property Relationships of Polymer-Based Nanocomposites with Polyhedral Oligomeric Silsesquioxanes as Nanofillers

Vorgelegt von
Master of Polymer Science
Ning Hao
aus Beijing, V. R. China

von der Fakultät II – Mathematik und Naturwissenschaften
der Technischen Universität Berlin
zur Erlangung des akademischen Grades
Doktor der Naturwissenschaften
Dr. rer. nat.
genehmigte Dissertation

Promotionsausschuss :
Vorsitzender: Prof. Dr. Michael Gradzielski
Berichter: Prof. Dr. Reinhard Schomäcker
Berichter: Priv.-Doz. Dr. habil. Andreas Schönhals
Tag der wissenschaftlichen Aussprache: 12.06.2007

Berlin 2007
D83

Abstract

Polymer-based nanocomposites were prepared by blending Polyhedral Oligomeric Silsesquioxane (POSS) with different sidegroups, PhenethylPOSS and Chloropropyl-POSS, into Poly(bisphenol A carbonate) (PBAC) and polystyrene (PS) respectively. The samples were obtained by film-casting under optimized conditions. The structure-property relationships of the nanocomposites were investigated by dielectric relaxation spectroscopy and gas transport measurements.

PhenethylPOSS can be blended into PBAC on a molecular level up to a concentration of about 10 wt%. Below this concentration, the dynamic glass transition process of the nanocomposites shifts to lower temperatures as the concentration of PhenethylPOSS increases. For concentrations higher than 10 wt%, the α-relaxation splits into two peaks. Moreover, close to the α-relaxation of PhenethylPOSS, a third process is observed. These results indicate a phase separation into a PBAC-rich domain with a few percents of molecularly dissolved POSS and PhenethylPOSS-rich domains. The POSS-rich domains are surrounded by interfacial layers of PBAC having a higher concentration of POSS than PBAC-rich phase. A phase diagram is deduced to describe the miscibility of POSS in PBAC matrix. Further analysis based on the Maxwell-Wagner-Sillars polarization proves that the average domain size of the POSS-rich phases increases with the concentration of POSS. The gas permeability of the samples is constant at lower concentrations but increases above 20 wt% of POSS. That is because the diffusion process of the gas molecule is faster inside the PhenethylPOSS-rich phase than in PBAC matrix. Corresponding changes are also observed for the activation energy of diffusion and the heat of sorption. The sorption isotherms of the nanocomposites can be well described by the Dual Mode Sorption Model (DMSM). The change of the DMSM parameters with the concentration of POSS implies that the fraction of fluctuating and 'frozen-in' free volume of the nanocomposites is reduced as the concentration of POSS increases. Blending PhenethylPOSS into PS shifts the α-relaxation process to lower temperatures. In contrast to PBAC-based PhenethylPOSS nanocomposites, no phase separation is observed up to 30 wt % of POSS. It is presumed that the phenethyl sidegroup of POSS have a stronger interaction with the phenyl rings in the side groups of PS than with the main chain phenyl rings of PBAC. This interaction behavior also influences the gas sorption properties of the nanocomposites. Blending ChloropropylPOSS into PBAC does not change the α- and the β-relaxation processes of the bulk PBAC significantly. Instead, it is observed that the crystallinity of the sample is increased with the content of POSS. It is presumed that the ChloropropylPOSS molecules form separate crystalline domains inside the PBAC matrix. These domains have no influence on the molecular mobility of the PBAC matrix.

Zusammenfassung

Polymerbasierte Nanokomposite wurden hergestellt durch Mischen von Polyhedral Oligomeric Silsesquioxane (POSS) mit verschiedenen Seitengruppen, PhenetylPOSS und ChloropropylPOSS mit Poly(bisphenol A carbonate) (PBAC) und Polystyrol (PS). Die Blends wurden als Filme unter optimierten Bedingungen gegossen. Die Struktur-Eigenschaftsbeziehungen der Nanokomposite wurden mit Hilfe Dielektrischer Spektroskopie und Gastransportmessungen untersucht.

PhenethylPOSS kann in PBAC auf molekularer Ebene dispergiert werden bis zu einer Konzentration von etwa 10 Gew.%. Unterhalb dieser Konzentration verschiebt sich die dynamische Glasübergangstemperatur mit steigender Konzentration zu niedrigeren Temperaturen. Bei Konzentrationen oberhalb 10 Gew.% spaltet sich der Peak der a-Relaxation auf. Ausserdem wird nahe der α-Relaxation von PhenetylPOSS ein dritter Relaxationsprozess beobachtet. Dieses Ergebnis deutet auf eine Phasenseparation in eine PBAC reiche Phase mit wenigen Prozent molekular gelösten POSS und eine PhenetylPOSS-reiche Phase hin. Die POSS-reichen Domänen sind umgeben von einer Grenzschicht aus PBAC, die eine höhere Konzentration an POSS aufweist als die PBAC-reiche Phase. Ein Phasendiagramm wurde abgeleitet um die Löslichkeit von POSS in der PBAC Matrix zu beschreiben. Eine weitergehende Analyse auf Basis der Maxwell-Wagner-Sillars Polarisation zeigt, daß die mittlere Domänengröße der POSS reichen Phasen mit der POSS Konzentration steigt. Die Gaspermeabilität der Proben ist bei niedrigen POSS Konzentrationen konstant und steigt ab einer Konzentration von 20 Gew.% POSS. Grund dafür ist die höhere Diffusionsgeschwindigkeit der Gasmoleküle in der PhenetylPOSS reichen Phase gegenüber der in der Polymermatrix. Entsprechende Veränderungen werden auch für die Aktivierungsenergie der Diffusion und die Lösungsenthalpie beobachtet. Die Sorptionsisothermen der Nanokomposite werden durch das Dual Mode Sorption Modell (DMSM) gut beschrieben. Die Änderung der DMSM Parameter mit der Konzentration von POSS kann im Rahmen des Modells als Reduktion des Anteils des fluktuierenden und des eingefrorenen Freien Volumens der Nanokomposite mit steigender POSS Konzentration gedeutet werden. Die Zugabe von PhenetylPOSS zu PS verschiebt die α-Relaxation zu niedrigeren Temperaturen. Im Gegensatz zu den PBAC basierten PhenetylPOSS Nanokompositen wird bis zu einer Konzentration von 30 Gew.% keine Phasenseparation beobachtet. Es wird angenommen, daß die Phenetyl Seitengruppen eine stärkere Wechselwirkung mit den Phenylringen des PS eingehen als mit den Phenylringen der Hauptkette des PBAC. Diese Wechselwirkung beeinflußt auch die Gassorptionseigenschaften der Nanokomposite. Das Einbringen von ChloropropylPOSS in PBAC ändert die α- und β-Relaxation der reinen PBAC Matrix nicht wesentlich. Stattdessen wird beobachtet, daß sich der Kristallinitätsgrad mit steigeneder POSS Konzentration erhöht. Es wird davon ausgegangen, daß die ChloropropylPOSS Moleküle separate kristalline Domänen innerhalb der Polymermatrix bilden. Diese Dömänen haben keinerlei Einfluß auf die Mobilität der PBAC Matrix.

Acknowledgement

My sincere gratitude goes to my advisors, PD. Dr. A. Schönhals and Dr. M. Böhning, for their thoughtful guidance and encouragement during the past four years. I also want to thank Prof. Dr. R. Schomäcker and Prof. Dr. M. Gradzielski of the Technical University of Berlin for the productive and constructive discussions about my Ph. D. research and dissertation.

The presented research for this dissertation was funded by the Ph. D. student program of the Federal Institute of Materials Research and Testing (BAM). I would like to take this opportunity to express my gratitude to Prof. Dr. M. Hennecke, Prof. Dr. J. Friedrich and the administrative staff of BAM. Their extraordinary efforts on the organization and the administration of the program are much appreciated.

Besides my advisors, I would like to send my best regards to all of the coworkers and colleagues in BAM research group VI.53. Many thanks to Dr. H. Goering, Dr. A. Fritz, Dr. S. Frunza, Dr. L. Frunza, Dr. G. Turky, Mr. B. Audi, Ms. A. Bertus and Ms. D. Labahn for their help with the experimental works. In addition, I owe my special thanks to my colleague Mr. O. Hölck for his generous assistance during the preparation of the manuscript.

Thanks to the experts of BAM who kindly participated in this research. Dr. E. Rikowski and Dr. R. Mach provided nanofillers, while Dr. J. Falkenhagen and Dr. P. Krüger (┼ 2007) measured the molar mass of samples by Gel Permeation Chromatography and MALDI-TOF Mass Spectroscopy. The infrared analysis was performed under the instruction of Dr. R. Mix. Ms. K. Brademann-Jock and Ms. A. Sobotta spent a lot of time helping with the preparation of the Density Gradient Column. I am very grateful to Mr. D. Neubert for analyzing the thermal properties of the samples.

Last but not least, this thesis would not have been feasible without the loving support from my family and friends. Their invaluable support never fails me.

Table of Content

1 Introduction

During the past decades, studies of polymer-based nanocomposites have extended the application of these materials to many new aspects.[1] Recent progress, including electric,[2] optical,[3] magnetic,[4] and mechanical properties[5] of nanocomposites, is widely reported in the literature. In addition, polymer-based nanocomposites often show remarkable transport properties of small penetrants, which can be favourable either for barrier applications, e.g. packaging, or as selective membrane materials for molecular separation processes.[6]

The mechanisms of these improving desirable properties are still under discussion. Many papers have attributed the significant enhancements of the material properties to the extremely high surface to volume ratio of the filler particles. The small size of the nanoparticle leads to a high interfacial region close to its surface. Within this interfacial region, the length-scale of the interaction corresponds to a size of several segmental units of the polymer. This unique interaction behavior at the interfaces modifies the segmental mobility and changes the packing structure of the matrix polymer. Macroscopically, such modification plays a decisive role for the performance of the nanocomposite material.

In general, nanoparticles can be introduced to the polymer matrix by two different ways. The nanoparticles with functional units can be linked to the polymer backbone by chemical reactions,[7-9] while the blending process is favorable for commercial reasons.[10-16] One of the major problems of the physical blending method is the possible agglomeration of the filler nanoparticles in the polymer matrix. In order to improve the solution compatibility of the nanofillers, a great deal of efforts, such as surface treatment of the nanofillers or the introduction of nanoparticles with core-shell structures, has

been applied.[17] Polyhedral Oligomeric Silsesquioxane (POSS) * has been discussed for its distinct core-shell structure. Surrounded by its bulky side-groups, the POSS molecule can be regarded as one of the smallest silica nanoparticles covered by an organic surface[18-21] (shown in Fig. 2- 2). This unique interfacial structure modifies the intermolecular interactions between the filler particles and the polymer segments in the microscopic scale and improves the properties of polymer in the macroscopic scale. Many research groups have reported that adding POSS molecules into polymers changes the glass transition temperature of the materials and improves the solution compatibility of silica particles to the polymer matrix.[22]

The changes of the segmental motions of the nanocomposites can be analyzed by broadband dielectric relaxation spectroscopy (BDRS, section 3.1).[23-26] Furthermore, since the ionic conductivity and polarization effects caused by the (partial) blocking of mobile charge carriers in inhomogeneous materials strongly influence the dielectric spectra (Maxwell-Wager-Sillars polarization, section 2.3.4), BDRS is suitable to investigate the micro-morphology of the nanocomposites as well. On the other hand, gas transport measurements (section 2.4) can be used to investigate the changes on the mobility and the packing structure of polymer chains, because the diffusion coefficient of the gas molecules is related to the molecular mobility of the polymer materials (section 2.4.2).[6,27-29] In addition, the solubility as well as the concentration of the penetrants depends on the fraction of the free volume of the nanocomposites (see section 2.4.3.2).

This thesis summarizes the results of recent investigations on the structure-property relationship of polymer-based nanocomposites with POSS molecules as nanofillers. The theories concerning the experimental techniques are presented in Chapter 2 and Chapter 3. The nanocomposite films were prepared by solution casting under optimized conditions. In order to characterize the impact of the interfacial properties of the filler molecules, POSS molecules

* POSS and PhenethylPOSS are trade marks for Polyhedral Oligomeric Silsesquioxane and phenethyl silsesquioxane (MS0870) of Hybrid Plastics Inc. (Hattiesburg, MS, USA), respectively. www.hybridplastics.com

with different sidegroup-polarity, the PhenethylPOSS and the Chloropropyl-POSS were incorperated into the matrix polymers. On the other hand, poly-(bisphenol A carbonate) and polystyrene were used as matrix polymers. It is assumed that these matrix polymers form different packing structures around the POSS molecules due to their chain flexibility and sidegroup mobility. The change of the dynamic mobility of the polymer in dependence of the POSS concentration was characterized by analysis of the dielectric spectra and interpretation of the gas sorption isotherm curves. In addition, conventional investigation methods such as Density Gradient Column (DGC, section 3.3.1), Differential Scanning Calorimetry (DSC, Chapter 3) and Fourier Transform Infrared Spectroscopy (FTIR, section 3.3.2) were used to characterize the properties of the nanocomposite samples. The related discussions are presented in the Chapter 4 and Chapter 5.

2 Fundamental

2.1 Polymer-based POSS Nanocomposites

The term ‘polymer-based nanocomposites’ refers to the group of polymer-inorganic hybrid materials containing two or more phases, in which at least one of them is in the nanometer scale. During the past decades, the research on polymer-based nanocomposites attracts tremendous attention for their various applications not only in the field of conventional engineering, but increasingly also in the fields of microelectronics, organic batteries, optics and catalysis. Related to the small size of the filler particles, polymer-based nanocomposites exhibit remarkable property improvements such as enhanced tensile properties, reduced gas permeability, reduced solvent uptake and improved thermal stability, when compared to conventional polymer-filler composites. In order to design new nanocomposites with desirable properties, an explicit understanding of the structure-property relationship of the polymer-nanofiller system is required. Many research groups have attributed the obtained improvements on material properties to the extremely high surface to volume ratio of the nanofillers (see Chapter 1).

Many nanoparticles, such as silica nanoparticles,[30,31] layered silicate clays,[32] nanosized metal particles[33] or carbon nanotubes[15,34,35] are reported as nanofillers to prepare polymer-based nanocomposites. Recently, there is a growing interest on preparing nanocomposites with Polyhedral Oligomeric Silsesquioxanes (POSS) as nanofillers.[11-13,16,19,20,36-46] As shown in Fig. 2- 1, The nearly exponential increase in the number of publications of POSS has made it one of the top nanomaterials in the field of nanoscience and nanotechnology.

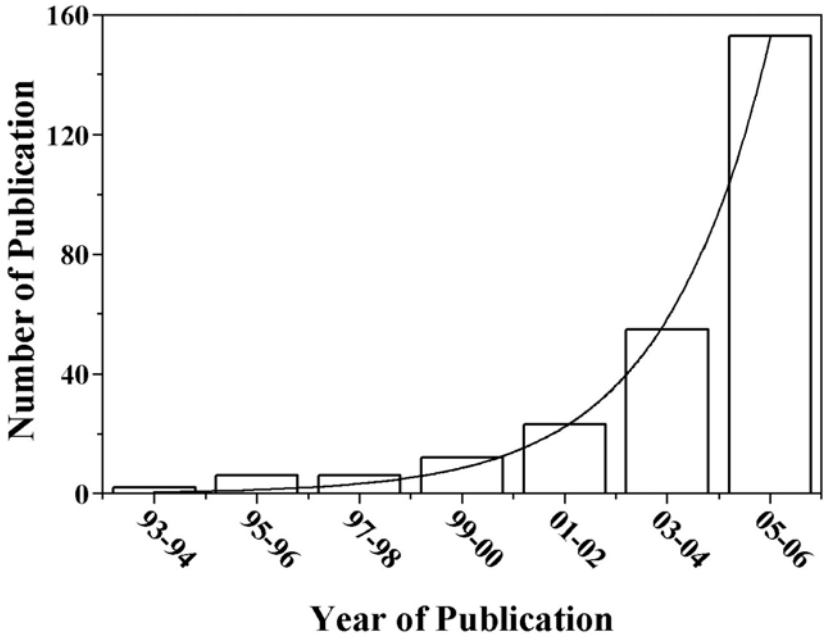

Fig. 2- 1 Number of POSS publication versus the year in which they were published. The number of publication is obtained from ISI web of knowledge by using "Polyhedral Oligomeric Silsesquioxane" as keyword. The curve shows an exponential growth of the number of publication.

As the structure presented in Fig. 2- 2 shows, the name silsesquioxane is derived from the Latin word 'Sesqui', which means 'one and a half', corresponding to its empirical formula $T_i=(RSiO_{1.5})_i$. Using conventional synthesis methods, such as the controlled hydrolysis of trichloro-oxysilanes or trialk-oxysilanes, a high yield of POSS can be obtained.[18,47]

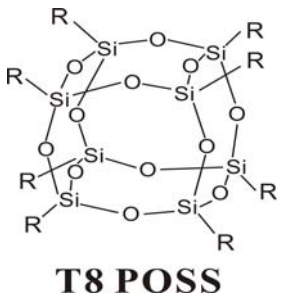

Fig. 2- 2 The chemical structure of a T8 POSS molecule. R is the sidegroup of POSS

POSS can be regarded as a particular hybrid organic-inorganic material with a core-shell structure. The average size of the silica core is about 0.5 nm containing eight, ten or twelve Silicon atoms. In addition to each of the Silicon atoms, an organic side group is attached (-R in Fig. 2- 2). These sidegroups

form a bulky organic surface outside of the silica core, which enhances the compatibility of POSS with the organic polymer matrix.[10,21,48]

Tab. 2- 1 The influence of POSS molecules on the physical properties of the polymer

Polymer	POSS molecules	Description	
PBAC	trisilanol-POSS	improved solution compatibility	[16]
PBAC	octaphenyl-POSS	reduced optical transparency,	[16]
PBAC	Al-phenyl-POSS Al-isobutyl-POSS	colored films with bubbles	[16]
PBAC	trisilanolisooctyl-POSS	slightly reduced T_g	[16]
PBAC	trisilanolphenyl-POSS	high solution compatibility transparent film up to 5 wt%	[16]
PET	isooctyl-POSS trisilanolisooctyl-POSS propanediolisobutyl-POSS	enhanced tensile modulus enhanced tensile strengths enhanced compressive strengths	[46]
PMMA	cyclohexyl-POSS methacryl-POSS	enhanced PMMA toughness	[11]
PMMA	acrylic-POSS	decreased T_g values	[11-13,20]
PP	Al-POSS Zn-POSS	improved thermal stability	[38]
PP	octamethyl-POSS	enhanced crystallization rate	[40,49]
PP	octaisobutyl-POSS	improved thermoxidative stability	[40]
PS	phenethyl-POSS	improved solution compatibility	[36,37,42,45]
PVE	octaisobutyl-POSS	reduced storage modulus	[44]
PVE	dodecaphenyl-POSS	enhanced storage modulus	[44]

The chemistry of POSS is quite flexible. By introducing organic sidegroup R with functional groups (e.g. double bond), POSS particles can also be incorporated into the polymer chains by covalent chemical bonds.[21] Compared to the synthesis method, this route offers a simple and inexpensive way to obtain polymer-based nanocomposites. Up to now, POSS was successfully blended into many polymer materials, such as polypropylene (PP),[48] high density polyethylene (HDPE),[10,19] poly(methyl methacrylate) (PMMA),[11-13,20] poly(vinyl chloride) (PVC),[14] Poly(ethylene terephthalate) (PET),[46,50,51] poly-styrene (PS),[36,37] poly(vinylester) (PVE)[44,49] and poly(bisphenol A carbonate) (PBAC).[16,42] Related improvements, including the modifications of the transparency, thermal stability and mechanical properties of the matrix polymer, were frequently discussed in the literature and summarized in the following table.

A critical problem of the physical blending method is the possible phase separation due to the agglomeration or even crystallization of POSS molecules in the nanocomposite. Many research teams have observed phase separation of the polymer-based POSS nanocomposites via microscopic or spectroscopic methods.[11-14,16,19-21,36-46,49,52] Blanski investigated micromorphology of PS-based nanocomposites by transmission electron microscopy (TEM), assumed that the solution compatibility of the POSS molecules in PS depends on the polarity of the sidegroups.[36,37] However, this assumption is not valid for all polymer-based POSS systems. According to the recently published results of Kopesky et al., the POSS molecules aggregated when the volume fraction of acrylic-POSS in PMMA was higher than 0.2.[11-13,20] Furthermore, the POSS aggregates may affect the material properties of the nanocomposites as well. By atomistic simulation, Capaldi[53] demonstrated that the phase separation of the cyclopentylPOSS/PE system was induced due to thermodynamic driving forces. The author showed that an additional polymer-rich domain with different molecular mobility close to the surface of the POSS aggregates existed. All these evidences give reasonable explanation on the modification of the composites materials.

2.2 Glass Transition Phenomena of Polymers

The glass transition process is regarded as one of the most important properties of polymer-based materials since it relates to the morphology and the segmental mobility of the polymer matrix. The basic concepts of the glass transition theory are discussed in section 2.2.1. Based on the double minimum potential model, the fluctuation of the matrix polymer can be described by dynamic relaxation models (section 2.2.2), such as the Free Volume interpretation (FV, section 2.2.2.1) and the Cooperative Rearrange Region (CRR, section 2.2.2.2). Theses models give phenomenological explanations of the glass transition processes.

2.2.1 Glass Transition Temperature

If an amorphous polymer is heated up from the glassy state, typically the shear modulus G of the material drops by a factor of 10^3 within a small

temperature range of 20~30 K (Fig. 2- 3). In practice, the material becomes softer and more flexible. This and other characteristic change of sample properties is named 'glass transition'[54] and can be observed for most of glassy materials, including amorphous polymers and semicrystalline polymers.

The glass transition is characterized by the so-called glass transition temperature (T_g). Many experimental methods are suitable to investigate the glass transition temperature of a polymer at a specific condition. By the dilatometric method, T_g is determined as the discontinuity from the volume-temperature plot (Fig. 2- 4A). By Differential Scanning Calorimetry (DSC), T_g can be obtained as the temperature point at the inflection point of the heat capacity (C_p) changes (Fig. 2- 4B). These methods investigate the glass transition temperature of the polymer in the isochronal scale with a characteristic frequency of ca. 10^{-2} Hz.[55]

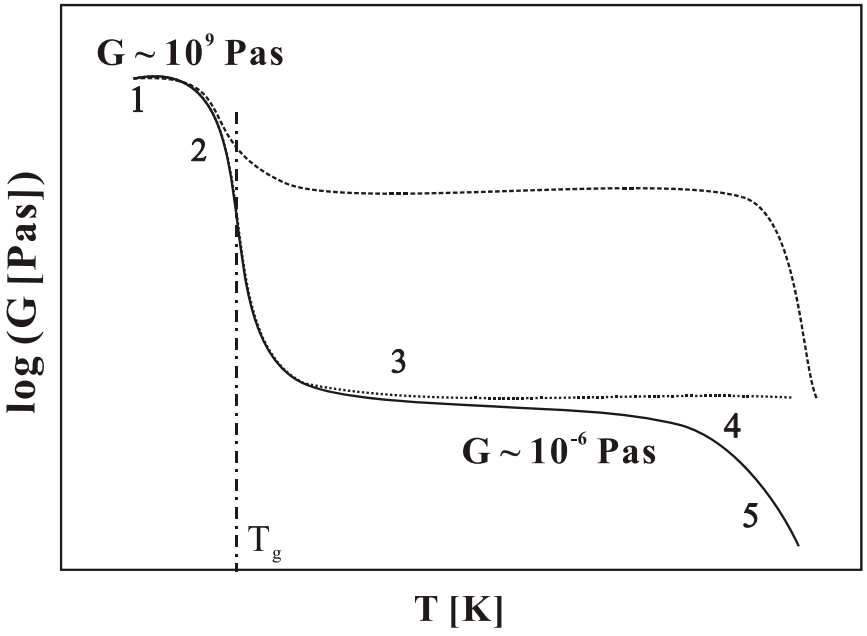

Fig. 2- 3 The typical temperature dependence of the shear modulus G of an amorphous polymer (solid line). Five regions of viscoelastic behavior can be observed. 1: glassy region; 2: glass transition region; 3: rubbery plateau region; 4: rubbery flow region; 5: liquid flow region. The effect of crystallinity (dashed line) and crosslinks (dotted line) are also presented in the same plot. The glass transition temperature T_g is measured as the temperature at the inflection point of the shear modulus changes.

On the other hand, the glass transition temperature can be determined by the relaxation methods, such as dynamic-mechanical analysis, (DMA)[56] light[57] and neutron scattering,[58] nuclear magnetic resonance (NMR)[59] and especially the broadband dielectric relaxation spectroscopy (BDRS)[23-26]. Fig. 2- 4C and Fig.

2- 4D demonstrates the typical results of DMA and BDRS measurements. In the glass transition region, the real part of the complex shear modulus (G′) and complex dielectric function (ε′) show a stepwise decrease versus temperature (Fig. 2- 4C), while the imaginary parts (shown as G′′ and ε′′ in Fig. 2- 4D) show a peak-like structure in the temperature domain.

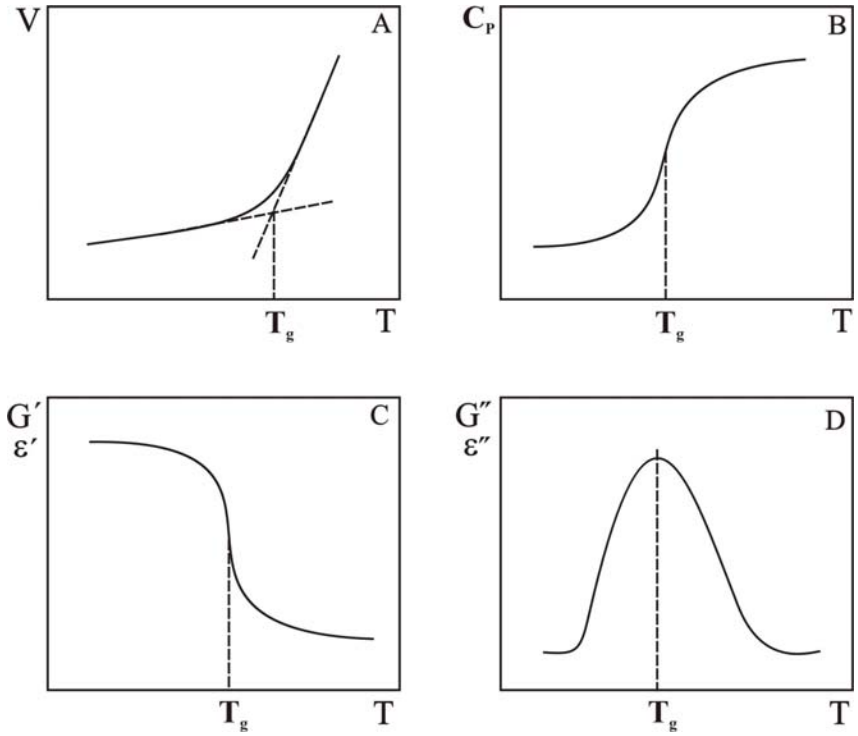

Fig. 2- 4 Schematic drawings of property changes at the glass transition temperature as obtained by A: dilatometric method; B: DSC; C and D: DMA and BDRS.

Considering the time or frequency effect of the measurement, the prominent feature of the glass transition process is the rapid increase of the characteristic relaxation time τ of the relaxation function. In general, the characteristic time of the relaxation increases as the temperature decreases. This effect is given by the Vogel-Fulcher-Tammann-Hesse function (VFTH, Eq. 2- 1):[60-62]

$$f(T) = f_{\infty} \cdot \exp\left(\frac{-A_0}{T - T_0^{id}}\right). \qquad \textbf{Eq. 2- 1}$$

In Eq. 2- 1, A_0 is a constant and f_∞ is a pre-exponential factor. T_0^{id} is termed as the ideal glass transition temperature. Empirically, the value of T_0^{id} is found to be about 30-70 K lower than T_g in the calorimetric and the viscometric measurements.

The VFTH function explains the experimental observation that varying the characteristic frequency or time of the measurements leads to a shift T_g values. Kovacs[63] showed that the heating and cooling rate of the experiment directly relates to the measured T_g values. For poly(vinyl acetate) (PVA), it is found that decreasing the cooling rate by a factor of 50 reduces T_g by about 8 K. This result reveals that the glass transition process is not only a thermodynamic property but depends strongly on the dynamic history (such as the time or frequency of the measurements) of the sample as well.

2.2.2 Molecular Dynamics of Pure Polymers

Assuming that the potential barrier of the molecular fluctuation is temperature independent, the simplest case of molecular fluctuation is described by jumps of segments in a double minimum potential model. The frequency-dependent fluctuation in a polymer material is determined by the dynamic equilibrium of two neighboring sub-states.[26,64] These fluctuation processes are named following the Greek alphabet sequence. The typical relaxation spectra of polymer at different temperature ($T_1 < T_2 < T_g$) is shown in Fig. 2- 5a.

The dynamic glass transition process (the α-relaxation) is located at lower frequencies in Fig. 2- 5a and shifts to the higher frequencies with increasing temperature. According to the Cooperative Approach presented in section 2.2.2.2, the α-relaxation is assigned to the cooperative segmental motion of the polymer chains. The temperature dependence of its relaxation rate f_p follows the VFTH function (Eq. 2- 1, Fig. 2- 5b).

As shown in Fig. 2- 5a, the β-relaxation processes can be observed at higher frequencies than the α-relaxation. Compared to the α-relaxation processes, such relaxation peaks can be identified by their broad and symmetric shape. The β-relaxation processes are usually related to localized segmental motions of the matrix polymer. Its relaxation rate $f_p(T)$ depends on the temperature according to the Arrhenius function (Fig. 2- 5b):

$$f_p(T) = f_\infty \exp\left(\frac{-E_A}{k_B T}\right). \qquad \textbf{Eq. 2- 2}$$

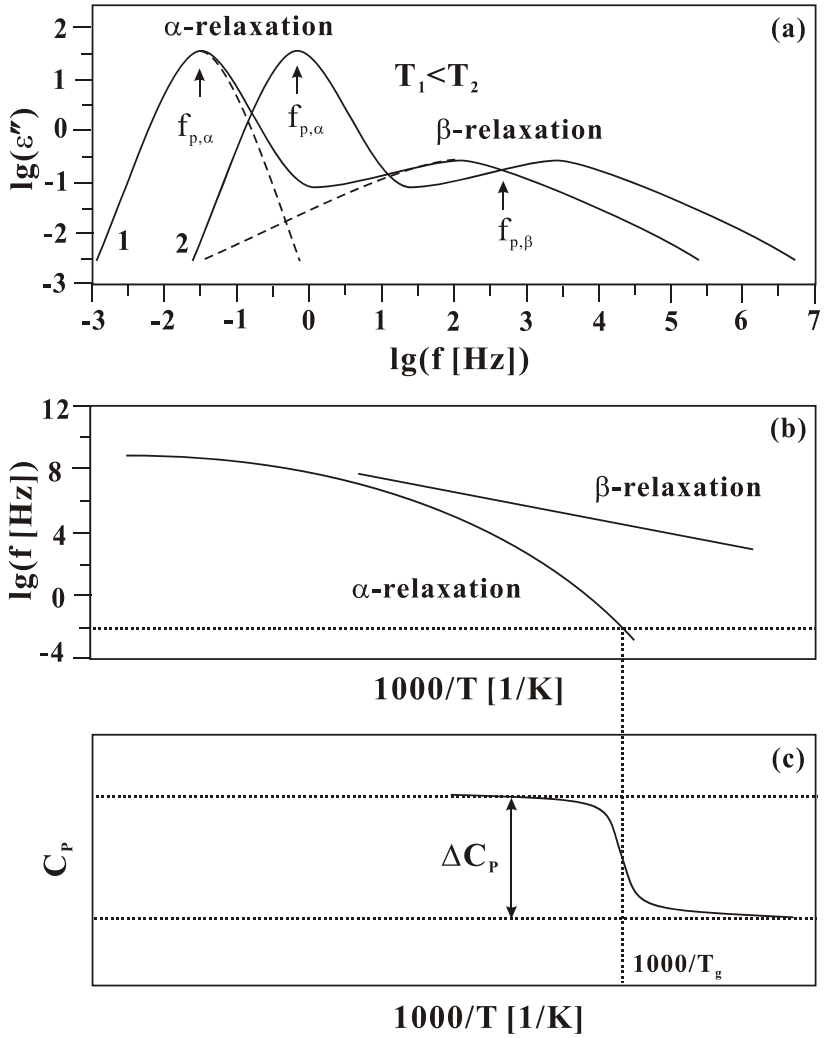

Fig. 2- 5 Schematic illustrations of the molecular dynamics of amorphous polymers around glass transition. (a): The dielectric loss versus frequency for two temperatures T_1 and T_2. Two relaxation processes, the α-relaxation (dynamic glass transition) and the β-relaxation, can be observed. (b): Temperature dependence of the α- and of the β-relaxation. The former can be described by the VFTH function (Eq. 2- 1) and the latter follows the Arrhenius function (Eq. 2- 3). (c): Calorimetric glass transition temperature is determined as the temperature at the inflection point of point of the heat capacity (C_p) changes.

In Eq. 2- 2 k_B is the Boltzmann constant ($k_B=1.381\times10^{-23}$ m^2 kg s^{-2} K^{-1}) and E_A is the activation energy of β-relaxation. f_∞ is the pre-exponential factor of the β-relaxation. For glassy polymers, the description of the molecular dynamics is complex in the temperature region close to the calorimetric glass transition temperature. Different concepts and theories have been developed to describe the glass transition based on the thermodynamic and kinetic considerations. In the following sections, two of the most popular interpretations, the free volume model and the cooperative approach will be discussed separately.

2.2.2.1 Free Volume Model

The concept of Free Volume (FV) was initially developed as a model to describe the molecular motion in pure polymers based on the presence of vacancies. These vacancies are named the free volume.[65] Doolittle and Cohen[66,67] attributed the free volume as the result of the inefficient packing of disordered polymer chains as the following assumptions state:

1. A specified volume V_S is attributed to every segment of the polymer chain. The 'free volume' V_f is defined as the difference between V_S and the occupied volume V_0:

$$V_f = V_S - V_0. \qquad \textbf{Eq. 2- 4}$$

2. The movement of the segments of the polymer chains is due to 'jump' processes between the vacancies.

3. The 'jump' of the segments does not 'cost' free energy.

Therefore, the characteristic time τ of a 'jump' follows relationship:[68,69]

$$\frac{1}{\tau} \sim \exp\left(-\frac{V^*}{\overline{V_f}}\right). \qquad \textbf{Eq. 2- 5}$$

In Fig. 2- 6, $\overline{V_f}$ is the average free volume and V* is the minimum free volume required for the 'jump' of a polymer segment. Assuming the change of fraction of the free volume $\overline{V_f}/V_s$ depends linearly on temperature, as Fig. 2- 6 showed:

$$\frac{\overline{V_f}}{V_S} = \frac{V_g}{V_S} + \alpha_f (T - T_g). \qquad \textbf{Eq. 2- 6}$$

The term V_g/V_S indicates the relative free volume at the glass transition. α_f is the thermal expansion coefficient. Inserting Eq. 2- 6, Eq. 2- 5 transforms to:

$$\frac{1}{\tau} \sim \exp\left[-\frac{\frac{V^*}{V_S\alpha_f}}{\frac{V_g}{V_S\alpha_f} + (T - T_g)}\right]. \qquad \textbf{Eq. 2- 7}$$

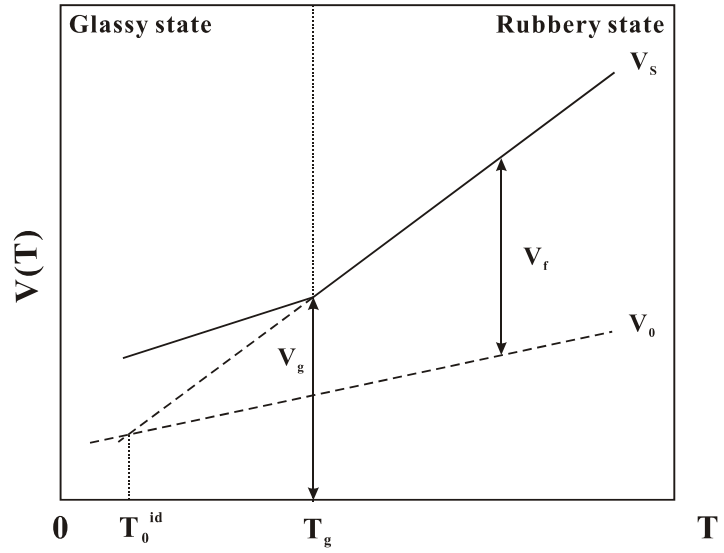

Fig. 2- 6 Schematic variations of specific volume, occupied volume and free volume versus temperature.

From Eq. 2- 7, the VFTH function (Eq. 2- 1) can be derived. Here, T_0^{id} refers to the temperature when $V_f = 0$. The free volume model establishes a simple correlation between the free volume and the temperature dependence of the relaxation time of the dynamic glass transition. However, it needs to be mentioned that in this simple model no characteristic length scale is involved. Furthermore all transport properties should have the same temperature dependence because the 'jump' of the polymer segments is the only transport mechanism. Thus the decoupling of rotational and translational diffusion as found experimentally can not be explained within this model.[26,64]

2.2.2.2 Cooperative Approach

Adam and Gibbs explained the temperature dependence of the relaxation of glass-forming polymers by the "temperature-dependent cooperatively rearrange region (CRR)".[64] According to the model, the CRR is a subsystem of the polymer matrix, which can be rearranged into another configuration independent from its environment. Assuming z(T)* is the number of segments in the CRR, the following relationship for the characteristic relaxation time τ is obtained:

$$\frac{1}{\tau(T)} \sim \exp\left(\frac{\Delta E \cdot z^*(T)}{k_B T}\right). \qquad \textbf{Eq. 2- 8}$$

Here, ΔE denotes the energy barrier for one molecular segment. The subsequent works by Donth showed that the cooperative length ξ of the CRR varies with the temperature as:[70]

$$\xi \sim \frac{1}{(T - T_0)^{\frac{2}{3}}}. \qquad \text{Eq. 2- 9}$$

The concept of cooperative fluctuations can be used to describe the molecular dynamics of the polymer close to its glass transition. In the glassy state, the polymer molecules are immobile and frozen in their local positions. In other words, the mobility of the polymer chains is restricted in a close space of its neighbors. As the temperature increases, the polymer chains acquire enough thermal energy to overcome the energy barrier. Therefore, the mobility of the polymer segment is enhanced and the glass transition can be observed.

Besides the above-mentioned theoretical assumptions, further models have been developed to discuss the particular property-temperature relationship of polymer materials around the glass transition temperature. Some of them, such as the energy landscape model,[71] the molecular-coupling theory (MCT)[72] and the avoid critical point model[73] act as effective tools to describe the glass transition process.

2.3 Theory of Dielectric Relaxation Spectroscopy

The dielectric relaxation spectroscopy is a powerful tool to study the molecular dynamics of polymers. This is due to the fact that a broad dynamical range from 10^{-3} to 10^{9} Hz can be covered by this method. Therefore the motional processes, which take place in polymer-based systems on extremely different time scales, can be investigated in a broad time and temperature range. Moreover, the motional process depends on the morphology and micro-morphology of the system under investigation. Thus, the information on the structural state of the materials can be indirectly extracted by taking molecular mobility as probe for the structure.

In this section, the theory of dielectric relaxation spectroscopy is discussed based on the knowledge of electrostatics and linear response theory. Empirical

functions are discussed to describe the relaxation properties in the temperature or frequency domains.

2.3.1 Polarization

For a small electric field with field strength **E**, the dielectric displacement (**D**) can be expressed as:

$$\mathbf{D} = \varepsilon_0 \varepsilon^* \mathbf{E}. \qquad \textbf{Eq. 2- 10}$$

In Eq. 2- 10, ε_0=8.854×10^{-12} As/(Vm) is the dielectric permittivity in vacuum.[24] ε^* is the complex dielectric function (Eq. 2- 11), which consists of the real (ε') and imaginary (ε'') part.

$$\varepsilon^* = \varepsilon' - i\varepsilon''. \qquad \textbf{Eq. 2- 11}$$

Applying an electric field causes orientation of the dipolar units in a material. In macroscopic scale, such orientation is characterized by the polarization **P**:

$$\mathbf{P} = \mathbf{D} - \varepsilon_0 \mathbf{E} = (\varepsilon^* - 1)\varepsilon_0 \mathbf{E}. \qquad \textbf{Eq. 2- 12}$$

The polarization of a material can have permanent or induced characters:

$$\mathbf{P} = \frac{1}{V_S}\sum \boldsymbol{\mu}_i + \mathbf{P}_\infty = \frac{N}{V_S}\langle \boldsymbol{\mu} \rangle + \mathbf{P}_\infty. \qquad \textbf{Eq. 2- 13}$$

In Eq. 2- 13, N/V_S is the volume density of dipoles. The permanent polarization is caused by the orientation of the permanent dipoles $\boldsymbol{\mu}_i$. The induced polarization $\mathbf{P}_\infty$ is caused by the local electric field, which distorts a neutral distribution of charges. It has different origins:

1. Electronic polarization: This resonant process occurs when the electron cloud of an atom (or molecule) is shifted with respect to the positive nucleus.
2. Atomic polarization: This process is observed when an agglomeration of positive and negative ions is deformed under the force of the applied field. This is also a resonant process.

Each of the above mentioned processes has specific features in the frequency dependence on ε^*. Applying a periodical electric field to the sample

causes the orientation of the dipolar units. The electronic and atomic polarizations are resonant processes. The characteristic time of these processes is about 10^{-14} to 10^{-15} s. In contrast, the reorientation of a permanent dipole is a relaxation process. Its characteristic time is in a broad time scale from nanoseconds to even hours.

In addition, the separation of moving charge carriers at the boundaries of separated phases or at the external electrodes contacting the sample induces polarization processes as well. These two effects are named Maxwell-Wagner-Sillars (MWS) polarization and electrode polarization, respectively. Both processes are not resonant processes. The detail of MWS polarization will be discussed in section 2.3.4.

Onsager[74] gave the most general expression of the relaxation strength $\Delta\varepsilon$ of the dielectric relaxation process by the theory of reaction field for the non-associating organic system. Furthermore, Kirkwood[75] and Fröhlich[76] extended Onsager's function to the following form:

$$\Delta\varepsilon = \varepsilon_S - \varepsilon_\infty = \frac{1}{3\varepsilon_0} Fg \frac{\boldsymbol{\mu}^2 N}{k_B T V}. \qquad \textbf{Eq. 2- 14}$$

In Eq. 2- 14, ε_S and ε_∞, describe the limits of dielectric storage ε' for low and high frequencies. The parameter k_B is the Boltzmann constant. The dielectric relaxation strength $\Delta\varepsilon$ is affected by the Kirkwood/Fröhlich correlation factor g, describing the interactions of a selected dipole with dipoles in its immediate vicinity. The influence of the unspecific Onsager factor F, which considers internal field effects in condensed systems, can be neglected for the systems under investigation[24].

2.3.2 Dielectric Relaxation

The dielectric relaxation process for small electric field strength is a special case of linear response theory.[24,77,78] The linear response theory for the isotropic systems describes the time dependent response of the system following a disturbance. For the dielectric relaxation processes, the disturbance is the time dependent external electrical field **E**(t), while the response of the system is the polarization **P**(t):

$$\mathbf{P}(t) = \mathbf{P}_\infty + \varepsilon_0 \int_{-\infty}^{t} \varepsilon(t-t') \frac{d\mathbf{E}(t')}{dt'} dt'. \qquad \textbf{Eq. 2- 15}$$

where ε(t) denotes the time dependent dielectric function and $\mathbf{P}_\infty$ covers all contributions arising from induced polarization. ε(t) can be measured directly as the time dependent response caused by an instantaneous change on the external electric field $d\mathbf{E}(t)/dt=\mathbf{E}_0\delta(t)$. The corresponding dielectric function has the form: $\varepsilon(t)=[\mathbf{P}(t)-\mathbf{P}_\infty]/\mathbf{E}_0\varepsilon_0$. The time dependence of the electric field and the time dependent relaxation function are sketched in Fig. 2- 7.

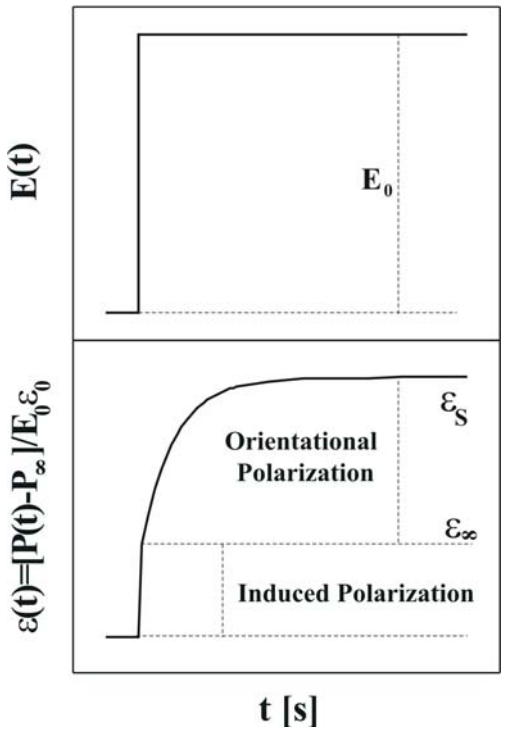

Fig. 2- 7 A schematic illustration of the time dependence between the electric field E(t) and the polarization P(t).

When a periodical electric field $\mathbf{E}(\omega)= \mathbf{E}_0\exp(-i\omega t)$ is applied to the dielectric material, Eq. 2- 15 transforms to:

$$\mathbf{P}(\omega) = \varepsilon_0(\varepsilon^*(\omega)-1)\mathbf{E}(\omega), \qquad \textbf{Eq. 2- 16}$$

with

$$\varepsilon^*(\omega) = \varepsilon'(\omega) - i\varepsilon''(\omega). \qquad \textbf{Eq. 2- 17}$$

where ε*(ω) is the complex dielectric function. ε′(ω) and ε′′(ω) are the real and imaginary parts of the complex dielectric function respectively. Here, ω is

the angular frequency with $\omega=2\pi f$ (f: the frequency of the periodical electric field). In this case, Eq. 2- 15 transformed to:

$$\varepsilon^*(\omega) = \varepsilon_\infty + \int_0^\infty \frac{d\varepsilon(t)}{dt}\exp(-i\omega t)dt\,. \qquad \textbf{Eq. 2- 18}$$

The function Eq. 2- 18 is a one-side Fourier transformation. The correlation $\varepsilon'(\omega) \sim d\varepsilon''(\omega)$ are related by the Kramers-Kronig relation (KK)[79,80]:

$$\varepsilon'(\omega_0) = \varepsilon_\infty + \frac{2}{\pi}\omega_0 \oint_C \frac{\omega\varepsilon''(\omega)}{\omega^2-\omega_0^2}d\omega\,, \qquad \textbf{Eq. 2- 19}$$

$$\varepsilon''(\omega_0) = \frac{2}{\pi}\omega_0 \oint_C \frac{\varepsilon'(\omega)-\varepsilon_\infty}{\omega^2-\omega_0^2}d\omega\,. \qquad \textbf{Eq. 2- 20}$$

The real and the imaginary part of the complex dielectric function are plotted in the Fig. 2- 8.

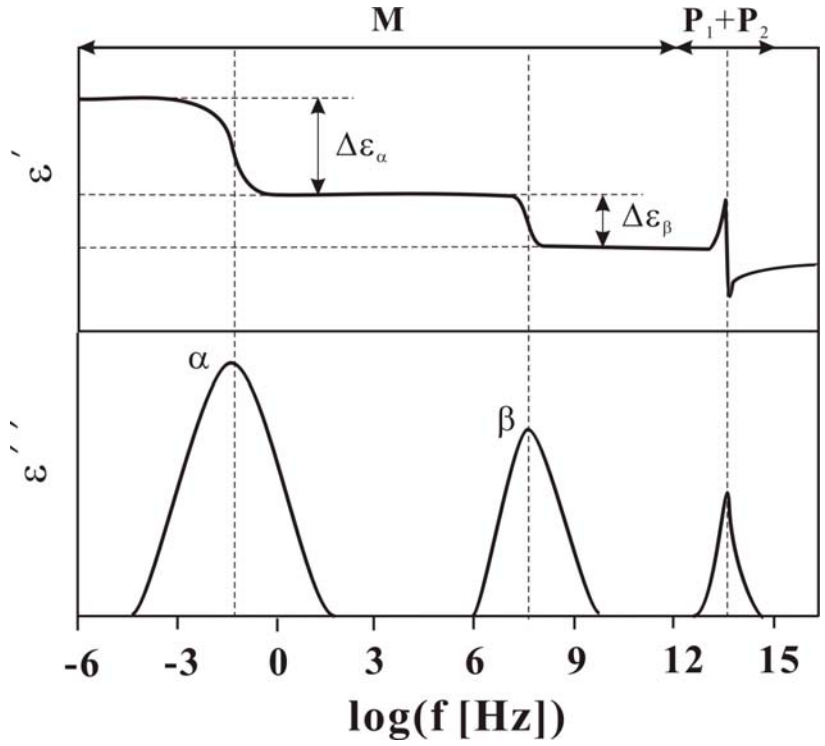

Fig. 2- 8 A schematic plot of the real and imaginary part of the complex dielectric function ε*(ω) versus frequency. M, P_1 and P_2 stand for the orientational polarization, the electronic polarization and the ionic polarization, respectively. The dynamic relaxation process and the secondary relaxation process are presented as α- and β-peak in the plot. The relaxation intensity of these processes are $\Delta\varepsilon_\alpha$ and $\Delta\varepsilon_\beta$.

Generally speaking, $\varepsilon'(\omega)$ shows a stepwise decrease with frequency and is related to the energy stored reversibly during the relaxation. The imaginary part,

ε´´(ω) has a peak-like structure in the frequency domain and is proportional to the energy dissipated in each period due to the relaxation. For these reasons, the real and imaginary parts are called the dielectric storage and dielectric loss in the literatures as well.

The KK relation indicates that both the real and the imaginary part of the complex dielectric function contain equivalent information on the relaxation process. The dielectric relaxation strength Δε is estimated as:

$$\Delta\varepsilon = \frac{2}{\pi}\int_0^\infty \varepsilon''(\omega)\mathrm{d}(\ln\omega). \qquad \textbf{Eq. 2- 21}$$

In the frame of statistical thermodynamics, one can use an auto correlation function to characterize the polarization of a material. Callen and Welton[81] gave the correlation function of the polarization fluctuations $\Delta\mathbf{P}(t) = \mathbf{P}(t) - \langle\mathbf{P}\rangle$ following the Fluctuation Dissipation Theorem (FDT):

$$\Phi(t) = \frac{\langle\Delta P(t)\Delta P(0)\rangle}{\langle\Delta P^2(0)\rangle}. \qquad \textbf{Eq. 2- 22}$$

Here t is the time variable. The limits of the Φ(t) as:

$$\lim_{t\to 0}\Phi(t) = 1 \quad \text{and} \quad \lim_{t\to\infty}\Phi(t) = 0. \qquad \textbf{Eq. 2- 23}$$

Insertion of Eq. 2- 13 into the correlation function Eq. 2- 22 yields:

$$\Phi(t) = \frac{\sum_i \langle\boldsymbol{\mu}_i(0)\boldsymbol{\mu}_i(t)\rangle}{\left\langle\left(\sum_i \boldsymbol{\mu}_i\right)\right\rangle} + \frac{2\sum_i\sum_{i<j}\langle\boldsymbol{\mu}_i(0)\boldsymbol{\mu}_j(t)\rangle}{\left\langle\left(\sum_i \boldsymbol{\mu}_i\right)\right\rangle}. \qquad \textbf{Eq. 2- 24}$$

Here, the first term on the right hand side of the equation is the auto correlation function of the dipole-dipole fluctuation. The second term on the right hand side describes the cross-correlation.

2.3.3 Analyzing Dielectric Relaxation Spectra

2.3.3.1 Debye Relaxation Process

The dielectric relaxation processes are analyzed by model functions. The simplest dynamic function for dielectric relaxation was developed by Debye[78]

and other authors[82,83]. Debye assumed that the change of polarization P is related to its actual value:

$$\frac{d\mathbf{P}(t)}{dt} = -\frac{1}{\tau_D}\mathbf{P}(t)\,. \qquad \textbf{Eq. 2- 25}$$

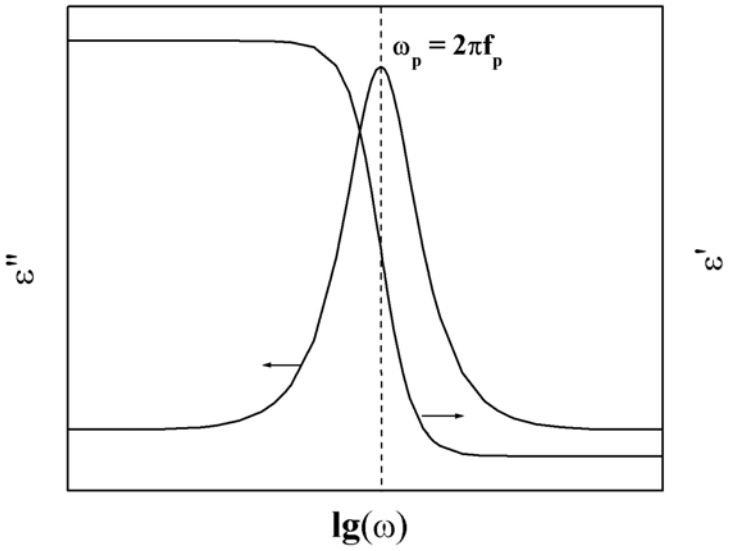

Fig. 2- 9 A schematic plot of the real and the imaginary part of the Debye function. The maximum frequency of dielectric loss is shown as ω_p in the plot.

Here, τ_D stands for the characteristic time of Debye relaxation. Solving Eq. 2- 25 gives:

$$\mathbf{P}(t) = \mathbf{P}(0)\cdot\exp\left(-\frac{t}{\tau_D}\right). \qquad \textbf{Eq. 2- 26}$$

Hence, the correlation function $\Phi(t)$ of Debye relaxation is an exponential decay.

$$\Phi(t) = \exp\left(-\frac{t}{\tau_D}\right). \qquad \textbf{Eq. 2- 27}$$

Insert Eq. 2- 27 into Eq. 2- 25, Debye relaxation function in the frequency domain is:

$$\varepsilon^*(\omega) = \varepsilon'(\omega) - i\varepsilon''(\omega) = \varepsilon_\infty + \frac{\Delta\varepsilon}{1+i\omega\tau_D}\,. \qquad \textbf{Eq. 2- 28}$$

where the real and the imaginary parts are given by Eq. 2- 29 and Eq. 2- 30.

$$\varepsilon'(\omega) = \varepsilon_\infty + \frac{\Delta\varepsilon}{1+\omega^2\tau_D{}^2} \qquad \textbf{Eq. 2- 29}$$

$$\varepsilon''(\omega) = \frac{\omega\tau_D\Delta\varepsilon}{1+\omega^2\tau_D{}^2} \qquad \textbf{Eq. 2- 30}$$

The frequency dependence of the real and the imaginary part is shown in Fig. 2- 9. In general, the dielectric storage shows a stepwise decrease with frequency, while the dielectric loss shows a peak-like structure in the frequency domain. From the maximum position of the dielectric loss, the mean relaxation rate f_p can be determined.

2.3.3.2 Non-Debye Relaxation Processes

Eq. 2- 28 gives the expression of a Debye relaxation process, which is valid for the orientation of a small rigid dilute dipole system and cannot be applied to amorphous polymeric systems. This is due to the fact that polymer materials are quite complex systems. For an isolated polymer molecule, a large number of atoms are covalently bonded together. Therefore, the dynamic relaxation of the polymer occurs on a broad time and temperature scales. Experimentally, the dielectric spectra of polymer materials are always asymmetric and broader than the prediction given by Eq. 2- 28.

The broadening of the time distribution of the relaxation peaks is described by the Cole-Cole function (CC, Eq. 2- 31)[82], where the β value characterizes the symmetric broadening of the relaxation peaks ($0<\beta\leq1$) and τ_{CC} is the characteristic time of the relaxation process:

$$\varepsilon^*_{CC}(\omega) = \varepsilon_\infty + \frac{\Delta\varepsilon}{1+(i\omega\tau_{CC})^\beta}. \qquad \textbf{Eq. 2- 31}$$

In some cases, the relaxation spectra become asymmetric and can be described by the Cole-Davidson function (CD, Eq. 2- 32): [83]

$$\varepsilon^*_{CD}(\omega) = \varepsilon_\infty + \frac{\Delta\varepsilon}{[1+i\omega\tau_{CD}]^\gamma}. \qquad \textbf{Eq. 2- 32}$$

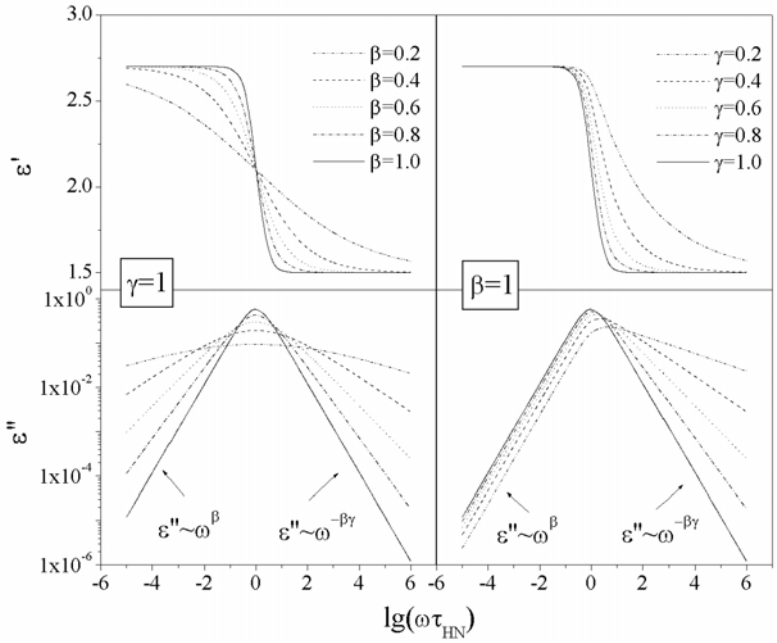

Fig. 2- 10 The complex dielectric permittivity for the Havriliak-Negami function with fixed shape parameter. In this plot, the initial value of ε_∞ and $\Delta\varepsilon$ are given as 1.5 and 1.2, respectively. The slop of ε´´ at infinite higher and lower frequency is calculated following the notation introduced by Jonscher[84] (Eq. 2- 38 and Eq. 2- 39).

In Eq. 2- 32, the parameter γ ($0<\gamma\leq1$) is introduced to describe the asymmetric broadening of a relaxation peak. Similarly, τ_{CD} is the characteristic time. A more general function, which is actually the combination of the CC and CD, is introduced by Havriliak and Negami (HN, Eq. 2- 33):[85-87]

$$\varepsilon^*_{HN}(\omega)=\varepsilon_\infty+\frac{\Delta\varepsilon}{\left[1+(i\omega\tau_{HN})^{\beta}\right]^{\gamma}}. \qquad \textbf{Eq. 2- 33}$$

The real and the imaginary part of the HN complex function have the following forms shown as Eq. 2- 34 and Eq. 2- 35, respectively.

$$\varepsilon'=\varepsilon_\infty+\frac{\Delta\varepsilon\cdot\cos(\gamma\varphi)}{\left(1+(\omega\tau_{HN})^{2\beta}+2(\omega\tau_{HN})^{\beta}\cos\left(\frac{\pi\beta}{2}\right)\right)^{\frac{\gamma}{2}}} \qquad \textbf{Eq. 2- 34}$$

$$\varepsilon''=\frac{\Delta\varepsilon\cdot\sin(\gamma\varphi)}{\left(1+(\omega\tau_{HN})^{2\beta}+2(\omega\tau_{HN})^{\beta}\cos\left(\frac{\pi\beta}{2}\right)\right)^{\frac{\gamma}{2}}} \qquad \textbf{Eq. 2- 35}$$

In Eq. 2- 34 and Eq. 2- 35, the parameter φ and the maximum frequency of the dielectric loss ω_P are:

$$\varphi = \mathrm{arctg}\left(\frac{\sin\left(\frac{\pi\beta}{2}\right)}{\left(\omega\tau_{HN}\right)^{-\beta} + \cos\left(\frac{\pi\beta}{2}\right)} \right), \qquad \textbf{Eq. 2- 36}$$

and

$$\omega_p = \frac{1}{\tau_{HN}} \left[\sin\frac{\beta\pi}{2+2\gamma} \right]^{1/\beta} \left[\sin\frac{\beta\gamma\pi}{2+2\gamma} \right]^{-1/\beta}. \qquad \textbf{Eq. 2- 37}$$

The HN function has four parameters. $\Delta\varepsilon$ and τ_{HN} are the relaxation intensity and the characteristic relaxation time. β and γ ($0<\beta,\beta\gamma\leq 1$) are parameters determining the shape of the relaxation spectra. The impacts of changing β and γ on the shape of ε′ and ε′′ plotted in Fig. 2- 10.

A more detailed investigation of the HN function was presented by Jonscher,[84] who introduced shape parameters m and n relating to β and γ.

$$\varepsilon_S - \varepsilon'(\omega) \sim \omega^m;\ \varepsilon''(\omega) \sim \omega^m \quad \text{for } \omega << 1/\tau_{HN} \text{ with } m=\beta \qquad \textbf{Eq. 2- 38}$$

$$\varepsilon'(\omega) - \varepsilon_\infty \sim \omega^{-n};\ \varepsilon''(\omega) \sim \omega^{-n} \quad \text{for } \omega >> 1/\tau_{HN} \text{ with } n=\beta\gamma \qquad \textbf{Eq. 2- 39}$$

Jonscher' s notation of the HN function indicates the slopes of the dielectric loss curve at the low and the high frequency part of the plot (shown in Fig. 2-5). The dielectric loss peak becomes broader as the β value decreases, while a low γ value corresponds to the asymmetry of the relaxation function. It also needs to be mentioned that the Debye relaxation function (β=γ=1), Cole-Cole relation function ($0<\beta<1$, γ=1) and Cole-Davidson relation function (β=1, $0<\gamma<1$) can be recovered when the shape parameters of the HN function adjusted accordingly. From this point of view, β and γ are named the symmetric and asymmetric broadenings of the relaxation process in the literature.

2.3.4 Maxwell-Wagner-Sillars Polarization

As stated in section 2.3.1, at internal phase boundaries, charge carriers can be blocked and give rise to MWS-polarization (Fig. 2- 11) or electrode polarization. In both cases, such an effect leads to separation of the charges and results in an additional contribution to the polarization.

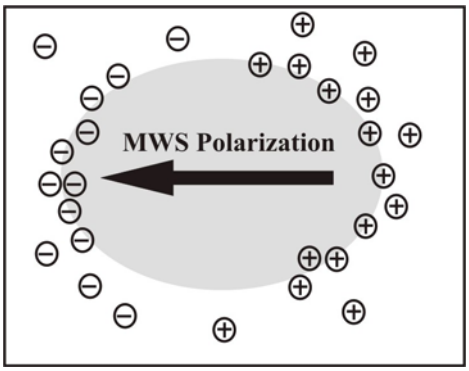

Fig. 2- 11 A schematic illustration on the separation of the moving charge carriers at the boundary of the phases (shown as the white and the grey areas).

The Maxwell-Wagner-Sillars polarization is widely observed in heterogeneous systems such as colloids, phase separated materials, biological materials with bond water and blends of crystalline and liquid crystalline materials. As the moving charge carriers are separated over a considerable distance, its contribution to the dielectric storage can be, by orders of magnitude, larger than that of the orientational polarization. This effect is generally accepted as a characteristic identifying of MWS-polarization.[88-91]

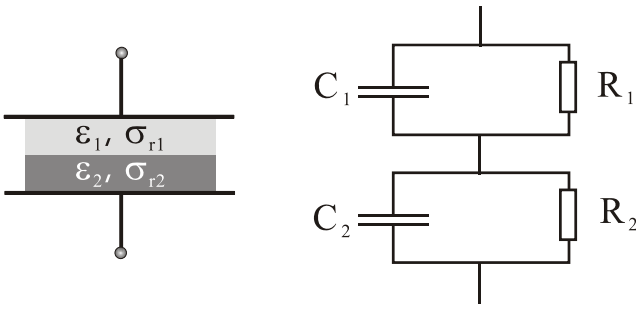

Fig. 2- 12 Schematic illustration of the two-layer capacitor model (left) and its equivalent circuit (right). Here, ε_i and σ_i are the permittivity and conductivity of the sample layers. C_i and R_i are the equivalent capacitance and resistance.

The MWS-polarization was investigated by many authors.[88-90] Theoretical assumptions were made regarding the structure, the shape and the orientation of embedded particles to give supplementary information on the dielectric properties of heterogeneous materials. The simplest model to describe a

heterogeneous material is the two-layer capacitor, which is shown in Fig. 2- 12. The two-layer capacitor model as well as the multi-layer lamella model often gives a good representation of compressed or sintered polycrystalline samples. In these cases, a boundary layer exists between adjacent particles or surface layers with different dielectric properties. The relaxation intensity $\Delta\varepsilon_{MWS}$ and relaxation time τ_{MWS} can be solved from its equivalent circuit (shown in Eq. 2- 40 and Eq. 2- 41).

$$\Delta\varepsilon_{MWS} = \frac{\sigma_{r1}\varepsilon_2 + \sigma_{r2}\varepsilon_1}{(\sigma_{r1} + \sigma_{r2})^2(\varepsilon_1 + \varepsilon_2)} \qquad \textbf{Eq. 2- 40}$$

$$\tau_{MWS} = \frac{\varepsilon_0(\varepsilon_1 + \varepsilon_2)}{\sigma_{r1} + \sigma_{r2}} \qquad \textbf{Eq. 2- 41}$$

For heterogeneous materials with complicate morphology, a series of new models were established to describe the distinct MWS-polarization process of the composites. Wagner[91] developed a function to describe a system, in which a spherical particle is suspended in an infinite dielectric medium. The specific admittance of the system was represented as the contribution of the admittance of each phase in relate to its volume fraction. Further calculations of τ_{MWS}, ε_s and ε_∞ were presented by Kharadly and Jackson[92] and by Dryden and Meakins[93] based on the Debye relaxation. A more general picture was sketched by Fricke in 1954,[94] which extended the shape of suspended particles from spherical to randomly orient ellipsoids by introducing a depolarization factor A ($0 \leq A \leq 1$) of the ellipsoid filler particles. The theoretical calculation of high particle concentration systems were given by Bruggeman[95], Hanai[96], Boned and Peyrelasse[97]. Steeman and Maurer[88-90] proposed a model for the complex dielectric function of the ellipsoidal shaped particles surrounded by an interlayer and dispersed into the matrix. The interlayer model is suitable to describe the dielectric properties of polymers filled by rigid particles since the use of filler particles often introduces a conductive layer of water at the interface. When the nonconductive fillers are covered by a conductive layer in an insulating matrix, the Steeman-Maurer function collapses to the Debye form function.

2.4 Gas Transport through Polymer Membranes

Polymer membranes can be applied as a perm-selective layer in gas separation processes.[6,27,28] Gas transport through membranes takes places when a driving force is applied to the feed components. Neglecting the impact from the external field, the chemical potential gradient, caused by the concentration gradient and the pressure gradient, can be regarded as the driving force of the gas transport process.[98] In gas transport measurements, the sample membranes can be generally sorted into two groups according to the pore size and pore size distribution. They are named as porous and nonporous membranes, respectively. The gas transport mechanism of the former is dominated by the Knudsen's flow or viscous flow, while the gas transport through the latter follows the so-called solution-diffusion mechanism. In practice, polymer and polymer-based nanocomposite membranes are categorized as nonporous membranes.

2.4.1 Solution-Diffusion Mechanism

Based on the pioneer work presented by Graham[99], Barrer[100,101] suggested a three-step solution-diffusion mechanism to describe the gas transport process in nonporous homogenous dense polymer films (Fig. 2- 13).

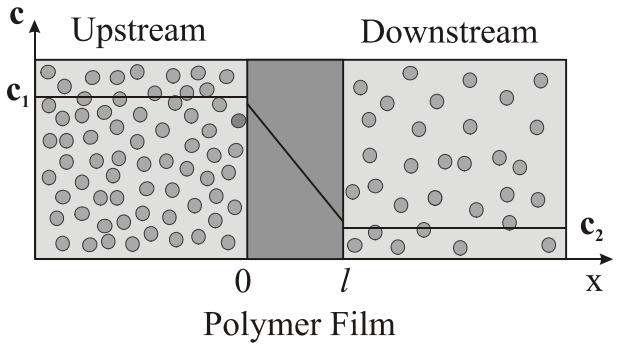

Fig. 2- 13 A schematic illustration of the solution-diffusion mechanism

The solution diffusion theory states:

1. Dissolution (sorption) of the gas molecules at the side of higher chemical potential (upstream phase);
2. Diffusion of the gas molecules across the polymer along the chemical potential gradient;

3. Desorption of the gas molecules at the lower chemical potential side; the gas molecules then enter the downstream phase.

As shown in Eq. 2- 42, the permeability (P) can be described as the product of solubility (S) and diffusion coefficient (D). The former is a measure of the amount of gas in the material, while the latter is a mobility related term, which describes the rate of penetrants moving in the polymer.

$$P = D \cdot S \qquad \textbf{Eq. 2- 42}$$

It needs to be mentioned that not all usual units of gas transport parameters are SI units. In this thesis, gas transport parameters are defined under standard temperature and pressure condition (STP: T = 273.15 K, P=101,325 Pa). The units of permeability, diffusion coefficient and solubility are as following.

$$[P] = 1\ \text{Barrer} = 10^{-10}\ \frac{\text{cm}^3(\text{STP}) \cdot \text{cm}}{\text{cm}^2 \cdot \text{s} \cdot \text{cmHg}}$$

$$[D] = 1\ \text{cm}^2/\text{s}$$

$$[S] = 1\ \frac{\text{cm}^3(\text{STP})}{\text{cm}^3(\text{polym.}) \cdot \text{cmHg}}$$

The diffusion of the penetrant in a nonporous polymer film can be described based on Fick's first law.[102,103] The Fick's first law establishes a relationship between the flux of a substance diffusing through the film (J) and the concentration gradient in three-dimensional scale. In order to solve the Fick's law, different boundary conditions have to be considered. In gas transport experiments, the sample membranes are so thin that only a negligible amount of gas molecules escape from the edges of the membrane. This is the so-called the "plane sheet boundary condition". Applying this unique boundary condition, the Fick's law can be simplified to the one-dimensional case as the following function Eq. 2- 43 shows. Here, ($\partial c/\partial x$) is the one-dimensional concentration gradient at each point of the film. c denotes the concentration of the gas:

$$J = -D \cdot \left(\frac{\partial c}{\partial x} \right) \qquad \textbf{Eq. 2- 43}$$

Fick's first law is valid in the steady state when the profile of the gas concentration is independent of time. The Fick's second law of diffusion

extends Eq. 2- 43 to the non-steady (transient) state by giving the local penetrant concentration c as a function of position x and time t.

$$\frac{\partial c}{\partial t} = -D \cdot \frac{\partial^2 c}{\partial x^2} \qquad \textbf{Eq. 2- 44}$$

The permeability coefficient of the gas molecules can be measured by the "time-lag" experiment under the following boundary conditions.

$$\begin{array}{lll} t < 0 & 0 \le x \le l & c = 0 \\ t = 0 & x = 0 & c = S \cdot p_1 \\ t = 0 & x = l & c = 0 \\ t > 0 & 0 \le x \le l & c = f(x,t) \end{array}$$

During the gas permeation measurements, a plane sheet membrane of thickness *l* and effective area A is placed between the partial pressures p_1 and p_2 at the two sides ($p_1 > p_2$, $p_2 \approx 0$ bar). Before the measurement starts, penetrant molecules have to be removed completely from both sides of the sample membrane. This procedure is called "degassing".

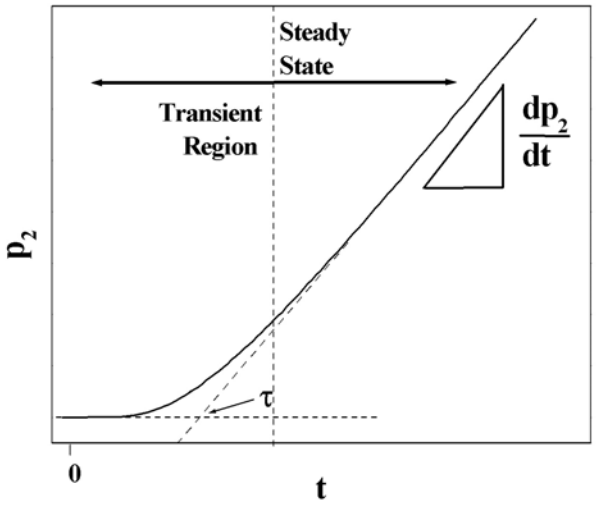

Fig. 2- 14 A typical result of the time-lag experiment (solid line). In the plot, the downstream pressure (p_2) is plotted versus the time (t). The straight dashed line denotes the extrapolation of the steady state part of the curve. The parameter τ is the time-lag of the experiment.

A typical result of gas permeation measurement is sketched in Fig. 2- 14. After applying the pressure p_1 at t=0, a transient region can be observed before the steady state is established. The term "time-lag" (τ) is introduced to describe

the time interval to establish the steady state concentration across the sample. When Henry´s law (Eq. 2- 45) is satisfied, in the steady state, the diffusive flux J being given by Eq. 2- 46 can be further simplified to Eq. 2- 47, which gives the steady state flux J_s.

$$c = p \cdot S \qquad \textbf{Eq. 2- 45}$$

$$J = -P \cdot \left(\frac{\partial p}{\partial x} \right) \qquad \textbf{Eq. 2- 46}$$

$$J_s = D \cdot S \cdot \left(\frac{p_1 - p_2}{l} \right) \approx D \cdot S \cdot \left(\frac{p_1}{l} \right) \qquad \textbf{Eq. 2- 47}$$

$$J_s = \frac{1}{A} \cdot \left(\frac{dn}{dt} \right) = \frac{1}{A} \cdot \frac{d(p_2 V_2 / RT)}{dt} = \frac{V_2}{A \cdot R \cdot T} \cdot \left(\frac{dp_2}{dt} \right) \qquad \textbf{Eq. 2- 48}$$

In Eq. 2- 48, R is the ideal gas constant (R=8.314 $Jmol^{-1}K^{-1}$) and V_2 is the downstream volume. Eq. 2- 49 can be used to determine the permeability from the experiment result.

$$P = \left(\frac{l}{p_1} \right) \cdot \frac{V_2}{A \cdot R \cdot T} \cdot \left(\frac{dp_2}{dt} \right) \qquad \textbf{Eq. 2- 49}$$

The diffusion coefficient can be obtained as the solution of Fick's second law under same boundary condition (Eq. 2- 50). Here, Q_t is the amount of the penetrant molecules passing through the membrane.[103]

$$\frac{Q_t}{l \cdot c_1} = \frac{D \cdot t}{l^2} - \frac{1}{6} - \frac{2}{\pi} \cdot \sum_{n=1}^{\infty} \left(\frac{(-1)^n}{n^2} \cdot \exp\left(\frac{-D \cdot n^2 \cdot \pi^2 \cdot t}{l^2} \right) \right) \qquad \textbf{Eq. 2- 50}$$

The steady state is established at infinite time ($t \rightarrow \infty$), the function above can be simplified to the form:

$$\frac{Q_t}{l \cdot c_1} = \frac{D \cdot t}{l^2} - \frac{1}{6}. \qquad \textbf{Eq. 2- 51}$$

Physically, the time-lag describes the time period until a constant concentration gradient is established across the membrane cross section ($0 \le x \le l$, see Fig. 2- 13). According to Fig. 2- 14, the diffusion coefficient of the penetrant can be estimate from the steady state extrapolation to the time axis (τ):

$$D = \frac{l^2}{6\tau}. \qquad \textbf{Eq. 2- 52}$$

It needs to be mentioned that the diffusion coefficient evaluated from time-lag experiment depends strongly on the concentration of the gas molecules and is described as the "effective diffusion coefficient (D_{eff})" in the literature.[104,105] During the course of this research, this D_{eff} is used as the mean value of the diffusion coefficient.

2.4.2 Diffusion of Gas Molecules in Polymers

In the previous section, the diffusion coefficient of gases is deduced from the solution of the Fick's second law. To describe the diffusion of small molecules in a polymer matrix, several models have been proposed. Fujita[106] and many other contributors [107,108] improved the free volume approach (FV, section 2.2.2.1) by analyzing the relative mobility of the diffusing molecules. The activated zone theory was further developed by Barrer based on the energy assumption.[109] Different from the free volume model, the actived zone theory was able to predict the activation energy of diffusion since Barrer attributed the diffusion of gas molecules to a thermally activated process. The molecular model of Kumins & Kwei[110] assumed that the diffusing molecule moves from the position to another if its energy of the molecule is high enough. In other words, the energy fluctuation allows the penetrant to make a 'jump'.

Involving the cooperative approach (section 2.2.2.2) in the diffusion process, Brandt & Anysas studied the diffusion of several gases (CO_2, CH_3Cl, CHF_3 and SF_6) in Polytetrafluoroethylene (PTFE)[111] and extended the activated zone theory through the discussion of a specific activation energy for a single molecular diffusion step. This approach is partly valid for the gas diffusion of polyethylene. Further developments were presented by DiBenedetto and Paul,[112] Pace and Datyner[113-116]. Theses authors argued that the 'jump' between the free volume cavities requires more activation energy than transport parallel to the orientation of the polymer chain.

Though these molecular models were initially developed for gas transport in rubbery polymers (gas transport above T_g), they can also be used to describe glassy polymers.[117] The diffusion properties of gas molecules in glassy

polymer can also be studied by simulation methods such as Monte-Carlo simulation techniques and molecular dynamics[118]. Several examples, such as dynamic simulations on the CH_4 in polyethylene,[119,120] He and CH_4 in poly(dimethylsiloxane)[121] and CO_2 in polysulfone[122] gave close values to the experimental transport parameters.

2.4.3 Sorption of Gas Molecules in Polymers

The term 'sorption' describes the dissolution of a penetrant into the matrix polymer.[98] It is characterized by the thermodynamic quantity solubility (S) describing the amount of gas molecules sorbed in the sample after the state of equilibrium is established. It should be noted that the sorption of the gas molecules in the pure polymer phases are dominated by different mechanisms. Several empirical models have been developed to describe the sorption behavior of the gas molecules.

2.4.3.1 Henry Model

A simple model, the Henry model, has emerged for sorption and permeation process of gases in polymers above their glass transition temperature.[98,100] In this case, the concentration of the gas is assumed to have a linear dependence on pressure.

$$c_D = k_d \cdot p \qquad \textbf{Eq. 2- 53}$$

Here, the Hery's parameter k_d is identical to the solubility S. k_d is independent of the gas concentration.

2.4.3.2 Dual Mode Sorption Model (DMSM):

For glassy polymers below T_g, the sorption isotherms of the sample at specific temperature is sketched in Fig. 2- 15. It has been observed extensively that equilibrium sorption of some gases does not follow Henry model, but rather a nonlinear isotherm exists.[123] To describe this particular sorption behavior, a dual mode sorption model (DMSM) was initially proposed by Barrer .[124,125] and extended by Vieth[126] and Paul [127].

$$c = c_D + c_H = k_d \cdot p + \frac{(c_H' \cdot b \cdot p)}{1 + b \cdot p} \qquad \textbf{Eq. 2- 54}$$

The DMSM assumes that the total concentration c of the sorbed gas molecules in a polymer comprises a component c_D for the dissolved species in the highly fluctuating free volume of the polymer matrix and c_H for molecules traped in the "frozen-in" free volumes. It is assumed that the former part obeys the Henry Model while the latter part follows the Langmuir equation for adsorption on a fixed number of equivalent sites with not more than one molecule per site.[123]

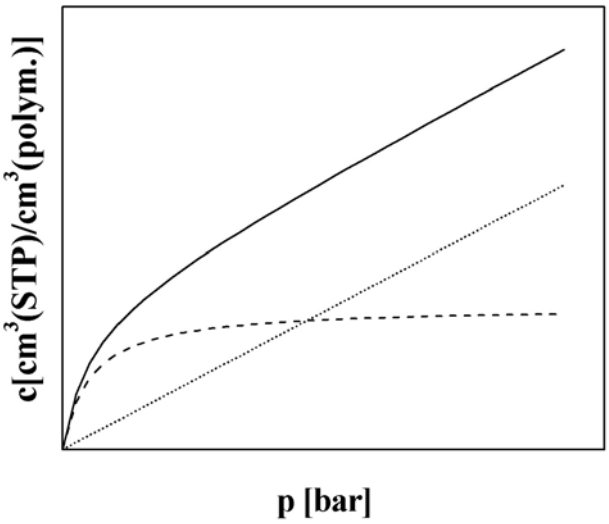

Fig. 2- 15 A schematic comparison of the Henry model (dotted line), Langmuir model (dashed line) and DMSM (solid line).

In Eq. 2- 54, c_H' is called the hole saturation constant (Langmuir capacity) and b is called the hole affinity constant. Following the statements given above, the parameters of DMSM: k_d and c_H' describe the fraction of highly fluctuating free volume and the fraction of frozen-in free volume, respectively. The DMSM establishes a correlation between the solubility of gas molecules and the diffusion coefficient. Fitting the DMSM to the sorption isotherm of gases, the fitting results are in agreement with the experiment results.[123,128,129]

Based on the experimental results of the ^{13}C-NMR spectra, some research groups stated that it is possible to identify the difference between the two populations of CO_2 molecules sorbed in polycarbonate[130] or polystyrene[131]. However, more others questioned the existence of two populations in the sorption process. Sefcik et al. developed the gas-polymer matrix model (GPMM) for the concentration dependence of the solubility in glassy

polymers.[132,133] They proposed that only one population of the penetrant exists during the gas transport. Since GPMM is in better agreement with the experimental result of the plasticization phenomena, the authors stated that the DMSM describes the sorption data rather well but ambiguous in the physical definition of the parameters. Similar results were presented by Brolly et al., who determined the effective coefficients of solubility and diffusion of CO_2 in polyethylene terephthalate (PET) and in polyethylene naphthalate (PEN).[134,135] Following their conclusion, the DMSM description seems to be closer to the results though only a single population of CO_2 molecules could be detected by infrared spectroscopy.

On the other hand, extensions of the DMSM were also developed to describe the sorption process of the gas molecules in glassy polymers. Among these, the partial immobilization assumption is frequently discussed. First introduced by Petropoulos.[136,137] Based on a concentration gradient to calculate permeability, diffusion coefficient and time-lag, Paul & Koros improved the model by assuming the diffusion coefficients of each gas population are different.[104] When the strong interaction between penetrant and polymer matrix is considered, the model of Paul & Koros can be modified by involving the contribution of the coupling between the diffusing species.[129,138,139]

2.4.3.3 Kinetics of Gas Sorption

During the gas sorption measurement, both sides of the sample film are in contact with the gases. Therefore, the concentration of the gas molecules in the polymer sample films can be estimated by the gas sorption measurement under the following boundary condition.

$$
\begin{array}{lll}
t < 0 & 0 \le x \le l & c = c_0 \\
t = 0 & x = 0 & c = c_1 \\
t = 0 & x = l & c = c_1 \\
t > 0 & 0 \le x \le l & c = f(x,t)
\end{array}
$$

Here, c_0 and c_1 are the gas concentration. Assuming the diffusion coefficient is constant and the membrane does not swell, the solution of Fick's second law (Eq. 2- 44) is given by Crank:[108]

$$\left(\frac{m_t}{m_\infty}\right)_F = 1 - \frac{8}{\pi^2}\sum_{n=0}^{\infty}\frac{1}{(2n+1)^2}\exp\left\{-\frac{D\cdot(2n+1)^2\cdot\pi^2\cdot t}{l^2}\right\}. \qquad \textbf{Eq. 2- 55}$$

Eq. 2- 55 can be simplified to Eq. 2- 56 for sufficiently short times:

$$\left(\frac{m_t}{m_\infty}\right)_F = \frac{4}{\pi^{1/2}}\left(\frac{D\cdot t}{l^2}\right)^{1/2}. \qquad \textbf{Eq. 2- 56}$$

In Eq. 2- 55 and Eq. 2- 56, the term $(m_t/m_\infty)_F$ denotes the mass uptake of the sample film in the Fickian diffusion process, in which m_t and m_∞ represents the sample mass at time t and infinit. These functions are applied for the estimation of diffusion coefficients of the sample (detail shown in section 3.2.2).

2.4.4 Temperature Dependence of the Gas Transport Parameters

Barrer showed that the diffusion of the gas penetrants through a rubbery material is an activated process. Excluding the impact of thermal transitions of the polymer, the permeability, the diffusion coefficient and the solubility are temperature-dependent:[140]

$$P = P_0\cdot\exp\left(\frac{-E_P}{R\cdot T}\right), \qquad \textbf{Eq. 2- 57}$$

$$D = D_0\cdot\exp\left(\frac{-E_D}{R\cdot T}\right), \qquad \textbf{Eq. 2- 58}$$

$$S = S_0\cdot\exp\left(\frac{-\Delta H_S}{R\cdot T}\right). \qquad \textbf{Eq. 2- 59}$$

In Eq. 2- 57, Eq. 2- 58 and Eq. 2- 59, the E_P, E_D and ΔH_S are the activation energy of permeation, the activation energy of diffusion and the enthalpy of sorption. Considering the solution-diffusion mechanism, Eq. 2- 60 holds:

$$E_P = E_D + \Delta H_S. \qquad \textbf{Eq. 2- 60}$$

E_D is correlated with physical properties of the penetrant such as the size and shape of the gas molecules. ΔH_S can be characterized by the critical temperature (T_C) of the gas molecules.[141,142] For more condensable gases (e.g. CO_2, CH_4 and NH_3), ΔH_S is negative.

3 Experimental

In this chapter, the basic concepts of the experimental techniques are briefly discussed. The morphology and molecular mobility of nanocomposites were investigated by the dielectric spectroscopy. The relaxation spectra were analyzed by fitting the Havriliak-Negami function to the data (section 3.1). The gas transport properties of nanocomposites are determined by gas permeation and gas sorption measurements in custom-made apparatuses (section 3.2.1 and section 3.2.2). Other characterization methods were applied to investigate the properties of the nanocomposite films. The density of the films was measured by Density Gradient Column (DGC, section 3.3.1), while the infrared spectroscopy was applied to estimate the content of POSS molecules in the nanocomposites (FTIR, section 3.3.2). The glass transition temperature of the sample is measured by the Differential Scanning Calorimetry (DSC, section 3).

3.1 Broadband Dielectric Relaxation Spectroscopy (BDRS)

3.1.1 Dielectric Measurement Techniques

The dielectric relaxation spectroscopy is suitable to determine the complex dielectric function $\varepsilon^*(\omega)$ of the sample in the very broad frequency range from μHz to THz.[23,24] For a capacitor C* filled with a material under study, the complex dielectric function is given by:

$$\varepsilon^*(\omega) = \frac{C^*(\omega)}{C_0}. \qquad \textbf{Eq. 3- 1}$$

Here, C_0 is the vacuum capacitance of the capacitor. Applying a sinusoidal electric field $\mathbf{E}^*=\mathbf{E_0}\exp(i\omega t)$, the complex dielectric function can be deduced by measuring the complex dielectric impedance $Z^*(\omega)$.

$$\varepsilon^*(\omega) = \frac{1}{i\omega Z^*(\omega) C_0} \qquad \textbf{Eq. 3- 2}$$

In order to determine the complex impedance of the sample, several methods such as Fourier correlation analysis (10^{-6}~10^7 Hz)[143], impedance analysis (10^1~10^7 Hz)[144], coaxial line reflectometry (10^6~10^9 Hz)[59] and network analysis (10^7~10^{11} Hz)[145] have been utilized.

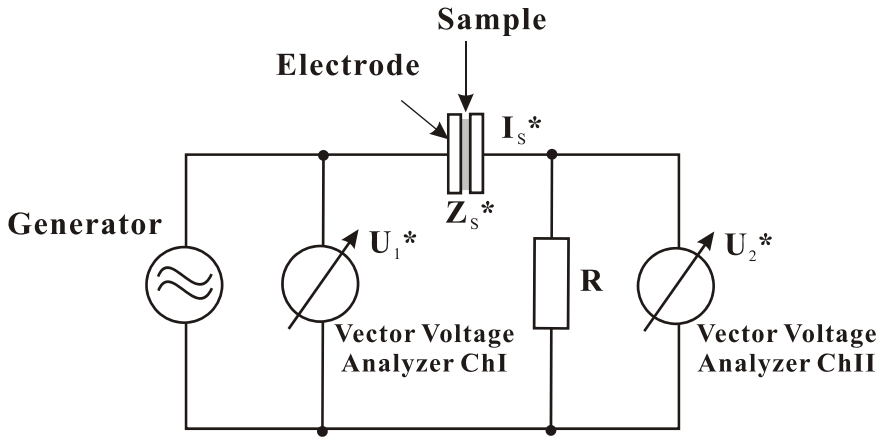

Fig. 3- 1 Scheme of the basic operation principle of a Fourier correlation analyzer.

The basic operation principle of a Fourier correlation analyzer is shown in Fig. 3- 1. It covers a frequency range from 10^{-3} to 10^7 Hz. The generator applies a sinusoidal voltage $U_1^*(\omega)$ to the sample. The resistor R converts the sample current $I_S^*(\omega)$ into a voltage $U_2^*(\omega)$. As a result, the complex impedance of the sample $Z_S^*(\omega)$ can be estimated.

$$Z_S^*(\omega) = \frac{U_S^*(\omega)}{I_S^*(\omega)} = R\left(\frac{U_1^*(\omega)}{U_2^*(\omega)} - 1\right) \qquad \textbf{Eq. 3- 3}$$

For dielectric measurements, the Fourier correlation analyzer introduced in Fig. 3- 1 with the resistor R has to be adapted due to its limitations.[143,144] For this reason, a dielectric converter is usually used for conversion of the sample current. The dielectric converter uses a broadband electrometer amplifier with variable gain (shown in Fig. 3- 2). It provides a broad frequency range (1 mHz to 10 MHz) for the dielectric measurements.

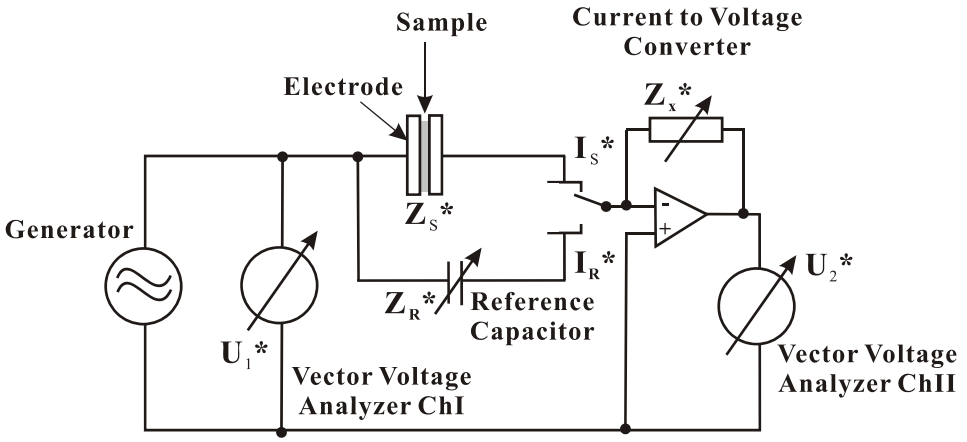

Fig. 3- 2 Scheme of a dielectric converter in the low-frequency range with electrometer amplifier and variable reference capacitor

If $Z_X^*(\omega)$ is a variable impedance, the sample impedance $Z_S^*(\omega)$ of a direct measurement is given by:

$$Z_S^*(\omega) = \frac{U_{1S}^*(\omega)}{I_S^*(\omega)} = -\frac{U_{1S}^*(\omega)}{U_{2S}^*(\omega)} \cdot Z_X^*(\omega). \qquad \textbf{Eq. 3- 4}$$

The accuracy of the function above is limited due to amplitude and phase errors in the current to voltage converter and the correlations. For this reason, further comparison of sample capacitor with a variable converter internal reference capacitor ($Z_R^*(\omega)$) is carried out under the same condition:

$$Z_R^*(\omega) = \frac{U_{1R}^*(\omega)}{I_R^*(\omega)} = -\frac{U_{1R}^*(\omega)}{U_{2R}^*(\omega)} \cdot Z_X^*(\omega). \qquad \textbf{Eq. 3- 5}$$

Comparing Eq. 3- 4 and Eq. 3- 5, the sample impedance $Z_S^*(\omega)$ can be estimated as:

$$Z_S^*(\omega) = \frac{U_{1S}^*(\omega)}{U_{2S}^*(\omega)} \cdot \frac{U_{2R}^*(\omega)}{U_{1R}^*(\omega)} \cdot Z_R^*(\omega). \qquad \textbf{Eq. 3- 6}$$

During the course of this research, the dielectric measurements were carried out by an Alpha-impedance analyzer (Novocontrol®) combining a high precision broadband dielectric material characterization system. The measured magnitude of the impedance covers a wide range from 10^{-3} to 10^{15} Ω in a broad frequency domain (3 μHz to 1 MHz)[144]. The sample film was mounted between two parallel round gold-covered electrodes (diameter of the upper electrode is 20 mm) of a capacitor, which is suitable in the cryostat. The capacitance of the sample was estimated from the effective dimension of the

film. The temperature of the sample was controlled by heating up nitrogen gas in the sample cell from 173 K to 473 K. The temperature of the sample cell is measured by a Pt100 temperature sensor and adjusted by a Quatro Cryosystem (Novocontrol®). The experimental stability of the system is 0.1 K. The experimental data were collected and monitored online by the program WINDETA®.

3.1.2 Fitting HN Function to the Experimental Results

Usually, the analysis of dielectric results is accomplished by fitting model functions to the experimental data in the isothermal scale (section 2.3.3). Despite the conductive contribution, the Havriliak-Negami (HN, Eq. 2- 33) function describes best the dielectric data in the frequency domain. Each parameter of the HN function can be estimated by:

$$\sum_i w_i \left[\varepsilon^*_i - \varepsilon^*_{HN}(\omega_i)\right]^2 \rightarrow \min. \qquad \textbf{Eq. 3- 7}$$

where i counts the number of experimental points. The parameter w_i is a weighting factor, which characterizes the accuracy of data measured by different equipments. The fitting procedures can be carried out by using either dielectric storage or dielectric loss since both the real (ε´) and imaginary part (ε´´) of the complex dielectric function ε*(ω) contain equivalent information on the relaxation processes (for details see section 2.3.3 and relates[79,80]). The discussions presented in this work focus on the analysis of the dielectric loss part of the complex function.

In practice, the observed spectra do not contain isolated peaks. Instead, different relaxation processes, such as the conductive contribution or MWS-polarization, can be observed as superposition of several relaxation processes. In case of pure electronic conductivity ($\sigma'(\omega)=\sigma_{DC}$), no contribution arises to ε´. Therefore, the contribution of conductivity in the dielectric loss is:

$$\varepsilon''(\omega) = \frac{\sigma_{DC}}{\varepsilon_0 \omega}. \qquad \textbf{Eq. 3- 8}$$

Eq. 3- 8 indicates that for pure electronic conductivity, the dielectric loss increases linearly with decreasing frequency (Fig. 3- 3). The function above describes the dielectric spectrum of an ideal conductive material.

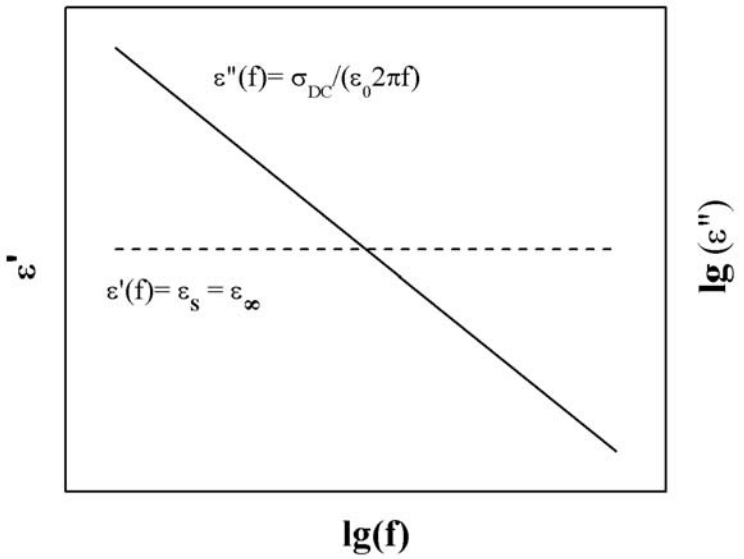

Fig. 3- 3 A schematic illustration on the frequency dependence of complex dielectric function with a pure ohmic conductivity. The dielectric storage and dielectric loss are shown as the dashed line and solid line respectively.

The mechanism of the transport of charge carriers in real dielectric materials is more complicated. In practice, $\varepsilon'' \sim a/\omega^s$ with $s<1$ is introduced to reduce the contribution of MWS or electrode polarization (a is the normalization factor with [a] = 1/s).[25]

$$\varepsilon^*(\omega) = i\frac{a\sigma_{DC}}{\varepsilon_0 \omega^S} + \varepsilon^*_{HN}(\omega) \qquad \textbf{Eq. 3- 9}$$

The dielectric spectrum presents a superposition of several relaxation processes due to fluctuations of different dipolar groups or polarization of moving charge carriers. Assuming the actual relaxation spectrum is a combination of k different processes and the whole spectrum consists of i different measurement points, the complex dielectric function can be separated by the HN function:

$$\sum_i w_i \left[\varepsilon^*_i - \sum_k \varepsilon^*_{HN,k}(\omega_i) \right]^2 \rightarrow \min. \qquad \textbf{Eq. 3- 10}$$

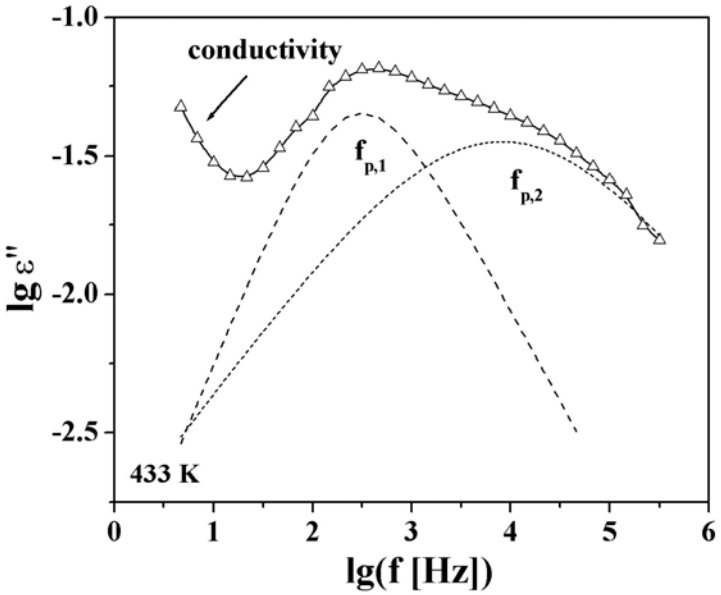

Fig. 3- 4 An example of fitting HN function to the dielectric spectrum. The dielectric spectrum (the open triangles) is fitted as superposition of two different relaxations (shown as the dashed lines) with a conductivity contribution.

Usually, the measured dielectric loss is extracted for the dielectric analysis. Fig. 3- 4 shows a typical isothermal dielectric spectrum (open triangles). As the superposition of the three processes, the fitting result (solid line) shows a very good description of the dielectric spectra.

3.2 Gas Transport Properties

3.2.1 Gas Permeation Measurement

3.2.1.1 Construction Scheme of the Gas Permeation Module

The schematic drawing of the gas permeation module is shown in the Fig. 3- 5. The vacuum of the system is supplied by a turbomolecular pump system (Leybold® Vacuum GmbH), which consists of a turbomolecular pump and an oil-sealed rotary vane vacuum pump. Such a system provides reliable vacuum down to 10^{-3} mbar, which is suitable for the measurements.*

* The gas permeaiton setup is designed and constructed by Dr. M. Böhning in BAM.

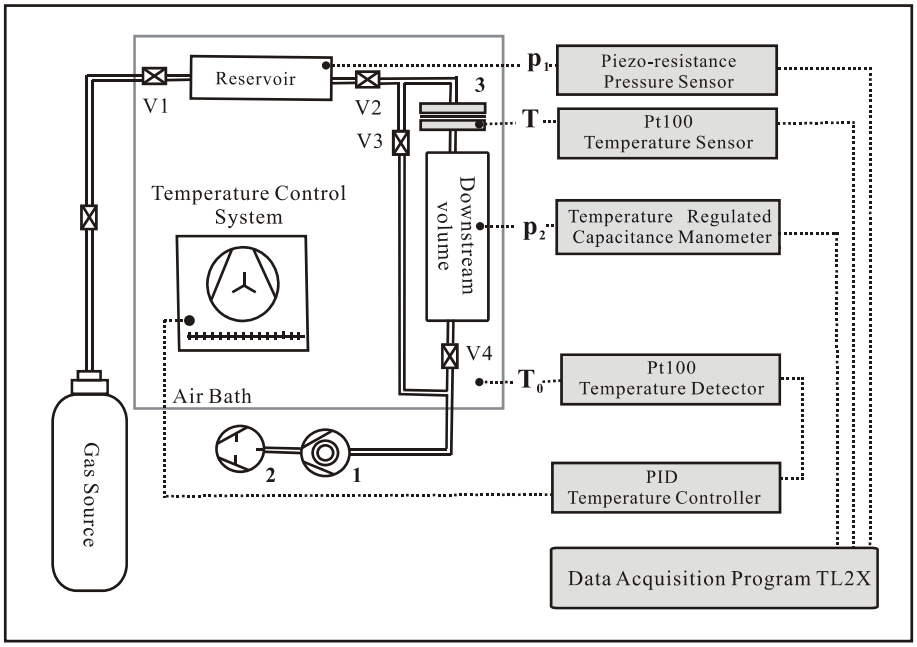

Fig. 3- 5 The construction scheme of gas permeation module. 1: The turbomolecular pump; 2: The oil-sealed rotary vane vacuum pump; 3: The permeation cell.

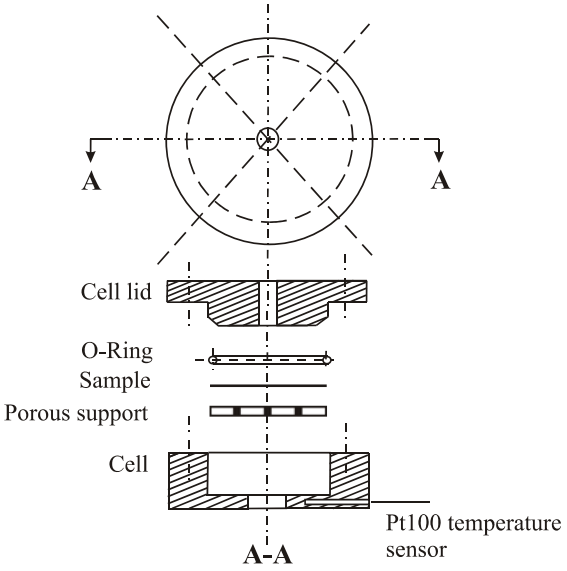

Fig. 3- 6 The construction scheme of permeation cell.

The reservoir in the upstream side of the permeation cell is designed to produce instantaneous pressure increase at the beginning of the experiment. The upstream pressure p_1 is detected by a piezo-resistance pressure sensor. The downstream volume is designed to maintain a low pressure in the downstream side. The downstream pressure p_2 is detected by Baratron® temperature regulated capacitance manometer 128 A. It provides a resolution of 0.01 mbar in the temperature region below 373 K. The temperature of the air bath is

controlled by an electronic PID temperature controller equipped with Pt-100 temperature sensor.

As shown in the inset of Fig. 3- 5, a custom-made permeation cell is mounted inside the setup. The highest pressure that can be applied to the cell is 30 bar. The sample film is mounted on the top of a porous synthetic metal support and sealed inside the permeation cell by a rubber O-ring. The outer diameter and the thickness of the O-ring are 40 mm and 5 mm. The temperature (T) of the sample is measured by a Pt100 sensor installed in the block of the permeation cell.

The experimental results were monitored by the program TL2X, which starts automatically when the pre-adjusted upstream pressure in the reservoir was changed. During the measurements, the downstream pressure p_2, upstream pressure p_1 and T were recorded as function of time.

3.2.1.2 Samples Preparation of Gas Permeation Measurements

The sample of the gas permeation measurement was cut from the film prepared by film-casting by using a die-cutting tool with a defined diameter of 38.5 mm. The thickness of the sample was determined by an electronic thickness gauge (Mitutoyo®).

3.2.1.3 Gas Permeation Measurement Technique

As discussed in section 2.4.1, the steady state gas flux and the time-lag value can be evaluated when the film is initially free of the penetrant molecules. Therefore, a degassing step is always required, i.e. vacuum was applied to both sides of the film before the measurement for at least 2 days. During the experiments, the empirical degassing time was applied around 10 times of the time-lag value of the previous permeation experiment.

For the gas permeation measurements, single measurement was always performed at constant temperature and upstream pressure. In the temperature domain, the measurements were performed with fixed upstream pressure of p_1=10 bar and with variable temperatures (T=308 K, 318 K, 328 K, 338 K). The latter measures different upstream pressure from 1 bar to 20 bar when T was kept constant (T=308 K).

The output downstream pressure was plotted as a function of time Fig. 2- 14. The slope (dp_2/dt) and x-axis interception were determined by fitting the data in the steady state by a linear regression function. As the effective area for permeation (A=707 mm^2), the downstream volume V_2 (V_2=43.8 cm^3), the thickness of the membrane (l) and upstream pressure (p_1) were known, the permeability coefficient (P) and diffusion coefficient (D) were calculated by introducing the obtained values to Eq. 2- 49 and Eq. 2- 52 respectively. The solubility coefficient (S) was determined according to Eq. 2- 42.

3.2.2 Gas Sorption Measurement

3.2.2.1 Construction Scheme of Gas Sorption Module

The scheme of the gas sorption module is shown in Fig. 3- 7. It consists of an electronic microbalance (Sartorius® GmbH, Germany), a pressure adjusting system and a temperature control system.

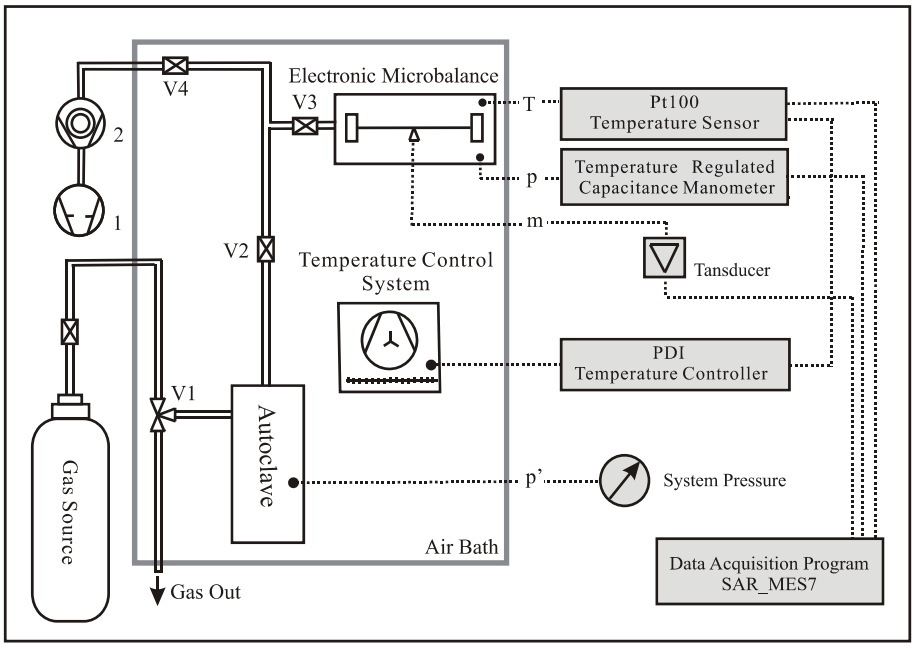

Fig. 3- 7 The construction scheme of the gas sorption module.

Similar to the gas permeation module, the whole system is covered in a air bath to control the temperature. The vacuum is provided by a turbomolecular pump system. A reservoir is installed in the system to provide a sufficiently large volume for minimizing the pressure changes in the test cell due to gas

sorption of the sample. The microbalance detects the weight of the sample with a resolution of 0.001 mg.[†]

3.2.2.2 Samples Preparation of Gas Sorption Measurements

Film-like samples are suitable for the gas sorption measurements. The flat films are cut into small pieces and weighted by the electronic balance (Sartorius® 1207 MPI) before the experiment.

3.2.2.3 Gas Sorption Measurement Techniques

During the gas sorption measurements, the gas pressure of the system was increased step by step. The degassing was required before each series of measurements in order to obtain the initial boundary condition for the measurements (see section 2.4.3.3). The minimum time of degassing is 48 h.

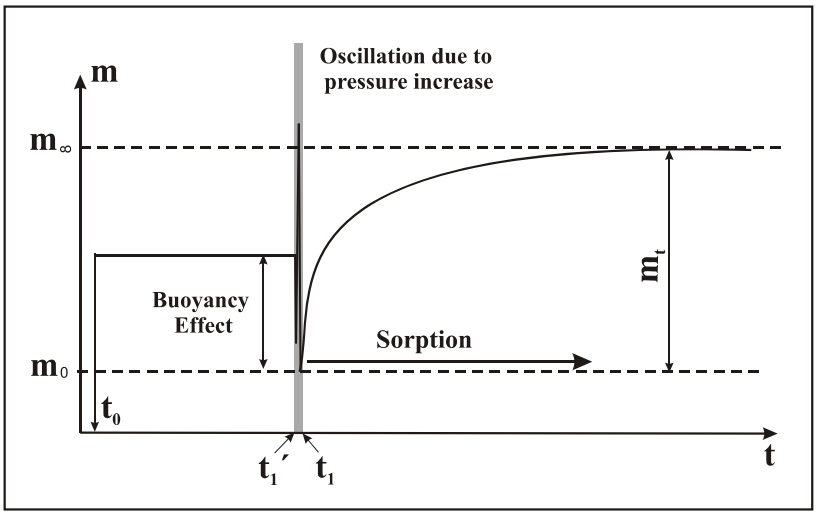

Fig. 3- 8 A schematic illustration of the buoyancy effect for the gas sorption experiments. The parameters t_0, t_1 and t_1' represent the time of measurement starts, the time of instantaneous pressure increase is applied and the time of sorption process starts. The parameter m_0, m_t and m_∞ denote the mass of the sample at time t_1, during the measurement and at the end of the measurement.

During the measurement, the sample mass m_t was recorded as a function of time by the program SAR_MES7. Fig. 3- 8 shows a typical result for the gas sorption measurement (solid curve), where t_0 denotes the beginning time of the data acquisition. A one-step instantaneous pressure increase was applied at

[†] The gas sorption setup is designed and constructed by Dr. M. Böhning in BAM.

time t_1' and causes an oscillation of the balance. The oscillation at the beginning of the measurement is due to the buoyancy effect and gas flow in the system. It can be separated from the actual sorption process at time t_1.[146] Theoretically, the sorption process terminated at infinite long time when a constant sample mass is reached.

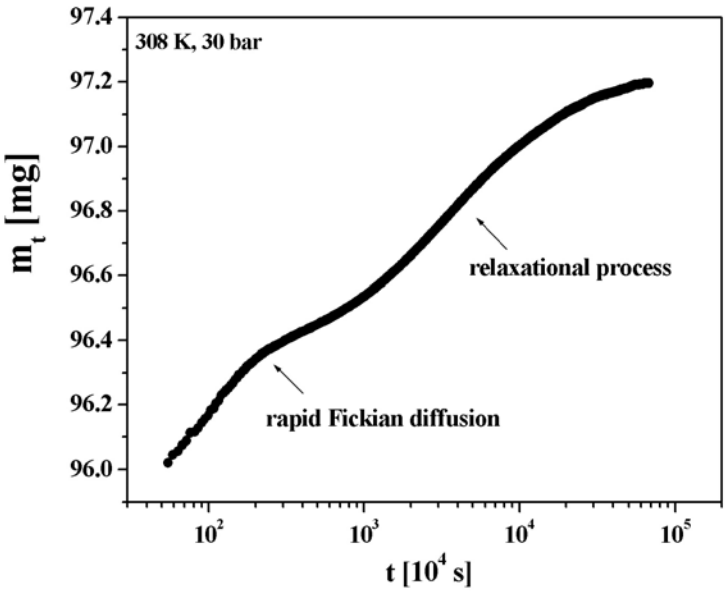

Fig. 3- 9 A typical result of the gas sorption measurement. The data are taken from the CO_2 sorption measurement of PS-based PhenethylPOSS nanocomposite (22 wt%). The sample mass mt is plotted versus time in logarithmic scale.

Experimentally, the equilibrium states of N_2 and O_2, can be reached within several minutes. In this case, the data acquisition was terminated manually within 1 hour. The diffusion coefficient of the sample (D) can be determined by fitting Eq. 2- 55 to the sorption curve after time t_1. Sufficient accuracy was achieved using the first two terms in the summation ($i \le 2$) of Eq. 2- 55.

$$c_i = \frac{\sum_{i=q}^{n} V_i(\text{gas})}{V(\text{polymer})} = \frac{R \cdot T_0}{p_0} \cdot \frac{\rho(\text{polymer})}{m(\text{polymer}) \cdot M(\text{gas})} \sum_{i=1}^{n} \Delta m_i \qquad \textbf{Eq. 3- 11}$$

The mass uptake ($\Delta m_i = m_\infty - m_0$) at each pressure step was determined according to the limits of the fitting regions. The volume gas concentration in the sample c_i [cm^3(STP)/cm^3(polymer)] was calculated based on Eq. 3- 11. In this function, T_0=273.15 K and p_0=1.013 bar. m(polymer), ρ(polymer) and M(gas) denote the sample mass, the density and molar mass of the penetrant.

The sorption isotherm can be obtained by plotting c_i versus pressure of the experiment p_i.

In the sorption measurements of highly sorbing gases, such as CO_2 and CH_4, m_t increases continuously. For the obtained data of CO_2 diffusion into polymer-based nanocomposite at 308 K, the shape of the sample mass curve (m_t) implies anomalous diffusion with a two-stage sorption process. Similar effect can be observed from CO_2 sorption measurements in Polysulfone.[147]

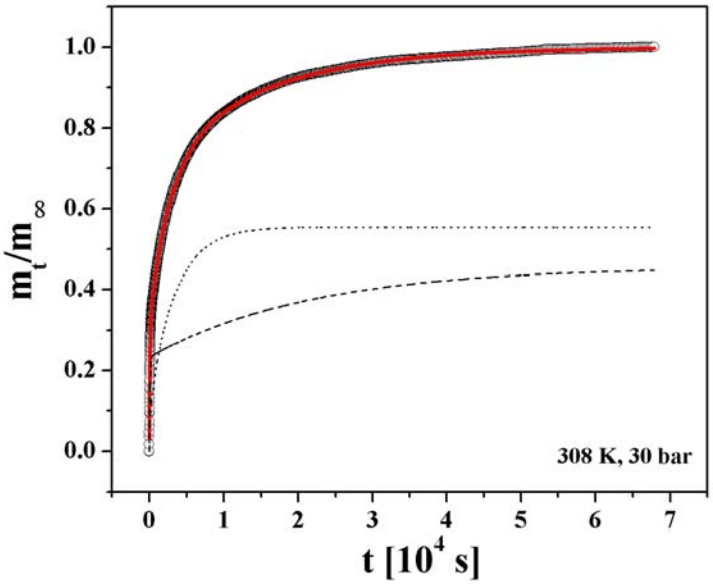

Fig. 3- 10 The kinetic sorption result of CO_2 in polystyrene-based PhenethylPOSS nanocomposite (22 wt%, empty cycles). The fitting results of the function Eq. 3- 12 is shown as the red curve. Its contribution of Fickian diffusion and the relaxation process are presented as the dotted line and the dashed line, respectively.

Based on the published result of Berens and Hopfenberg[148] and Hölck et al.,[149] the sorption process is explained as superposition of a rapid Fickian diffusion in the first stage (the first term in the right side of Eq. 3- 12) and a relaxational processes of the polymer matrix as the second stage (the second term in the right side of Eq. 3- 12). Thus, for a detailed analysis of the kinetics of sorption, the following model function has been fitted to the sorption and dilation data, respectively.

$$\frac{m_t}{m_\infty} = \left(\frac{m_t}{m_\infty}\right)_F + \sum_i \left(\frac{m_{t,r}}{m_\infty}\right)_i \left[1 - \exp\left(-\frac{t}{\tau_{r,i}}\right)\right] \qquad \textbf{Eq. 3- 12}$$

It needs to be mentioned that the Fickian diffusion term $(m_t/m_\infty)_F$ is discussed in the previous section (Eq. 2- 55) as the solution of the second Fick´s law.[103] In addition, the term $(m_{t,r}/m_\infty)$ and $\tau_{r,i}$ in the relaxational contribution are fitting parameters of the function. Sufficient accuracy was achieved using the first two terms in the summation ($i \leq 2$) of Eq. 3- 12. As shown in Fig. 3- 10, the fitting result of the superposition function (read line) is much closer to the experimental data.

3.3 Basic Sample Properties

3.3.1 Density

The density of polymers, which is connected to the diffusion coefficient and permeability of the sample, is an important parameter. It was determined by the Density Gradient Column (DGC) during the course of this research. The DGC was prepared at 296.15 K according to the standard DIN 53/479. By mixing solutions with different density (shown in Fig. 3- 11), a linear density gradient of the reference solution was obtained in the column.

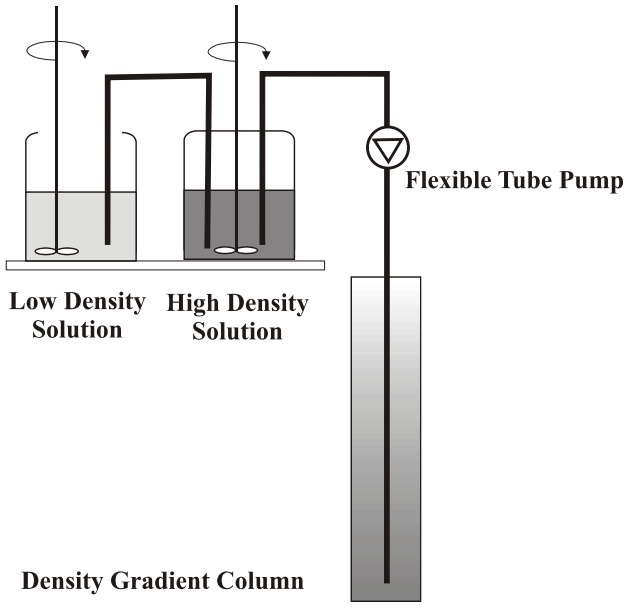

Fig. 3- 11 A schematic drawing on the preparation of density gradient column

Two columns with different density range were prepared. $Ca(NO_3)_2/H_2O$ solution (ρ=1.175~1.220 g/cm^3) is used in the measurements of the PBAC-based nanocomposites, while the isopropanol/H_2O solution is used in the

measurements of PS-based nanocomposites (ρ=1.040~1.114 g/cm^3). The density gradient of the solution was calibrated by floating glass beads with known density. The absolute error of the calibration of the glass floats was below 2 %.

The nanocomposite films were cut into small pieces before the measurement starts. The samples were cleaned in an ultrasonic ethanol bath for 15 min. For the measurements, the samples were immersed into the gradient column. After 4~6 hours, the density of the sample was determined by their position in the DGC relative to the standard glass beads. The density of the sample was taken as the average of the measurement results during one week after the calibration, with an accuracy below 1 %.

3.3.2 Infrared Spectroscopy

The infrared spectra of the samples film were measured by a Thermo-Nicolet (Nexus® 670) Fourier Transform Infrared Spectrometer (FTIR) at room temperature. The sample films were examined in the wave number range between 400 and 4000 cm^{-1}. For all of the samples, 64 scans with a resolution of 2 cm^{-1} were performed to record the spectra.

The IR spectrum of the pure PhenethylPOSS sample was measured by Attenuated Total Reflection Infrared Spectroscopy (ATR-IR). Before the measurements, the viscous PhenethylPOSS was cast onto the surface of an internal reflection element, which is made of Germanium. The IR radiation from the spectrometer enters and totally reflects through the Germanium crystal (shown in Fig. 3- 12). The sample interacts with the evanescent wave resulting in the adsorption of radiation by the sample at each point of reflection.

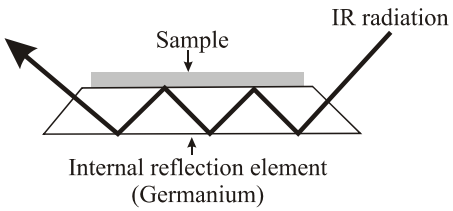

Fig. 3- 12 A schematic drawing of the total reflection with internal reflection element.

It needs to be noted that although ATR-IR and transmission spectra closely resemble each other, differences can always be observed because of the

dependence of the penetration depth on wavelength. It is known that longer wavelengths penetrate further into the sample. Therefore, the adsorption bands of ATR-IR spectrum at longer wavelength are more intense than those at shorter wavelengths.

3.3.3 Thermal Analysis

The thermal analysis of the nanocomposites was carried out by the Differential Scanning Calorimetry (DSC). The DSC measurements were performed using a SEIKO® DSC 220C instrument equipped with a liquid nitrogen cooling accessory. The nanocomposite samples were heated and cooled with a rate of 10 K/min. The experimental results were taken from the second rump of the measurement. The glass transition temperature of the sample was determined as the temperature at the inflection point of the C_p changes in the DSC thermogram.

4 Materials

In the present work, the samples for the measurements were prepared by blending different POSS molecules into different matrix polymers. Phenethyl-POSS and ChloropropylPOSS were used as nanofillers in the investigations. Poly(bisphenol A carbonate) and polystyrene, were used as matrix polymers to prepare nanocomposites. Their basic properties are discussed in section 4.1 and 4.2, respectively. The nanocomposites were preparation via solution casting under optimized conditions (section 4.3). As a result, four different nano-composites were obtained. Their physical properties were characterized by the experimental methods discussed in section 3.

4.1 Molecular Silica POSS

4.1.1 PhenethylPOSS

PhenethylPOSS (octa-phenethylPOSS, MS0870) is purchased from Hybrid-Plastics Inc (Hattiesburg, MS, US). It is a viscous liquid and soluble in organic solvents at ambient conditions. The density of PhenethylPOSS was measured as 1.21 g/cm^3.

The chemical structure of an octa-PhenethylPOSS molecule (T8) is sketched in Fig. 4- 1. The molecular simulation of the POSS showed that the phenethyl sidegroups form a bulky surface outside of the silica core structure. The MALDI-TOF mass spectrum (Bruker Reflex 3 spectrometer) of Phenethyl-POSS is shown in Fig. 4- 2. The result reveals that the PhenethylPOSS is a mixture of T8, T10 and T12 POSS molecules. Its weight averaged molar mass is determined as 1258 g/mol by Gel Permeation Chromatography (GPC).

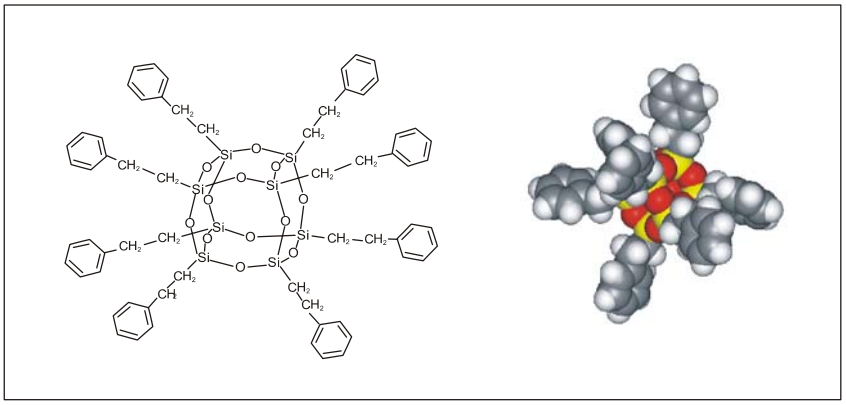

Fig. 4- 1 Left: Chemical structure (shown in the left side) of a T8 PhenethylPOSS molecule. Right: The figure shows an octa-PhenethylPOSS molecule in a representation of van deWaals-sphere [hydrogen (H): white; carbon (C): grey; oxygen (O): red; silicon (Si): yellow]. The structure was minimized in vacuum with Insight II using the compass force field. The simulation was carried out at 308 K for 10 ps using the same force field.

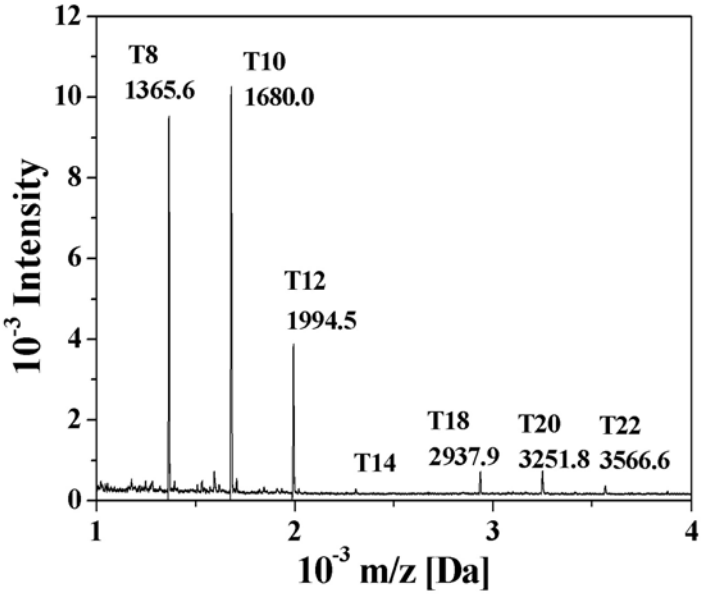

Fig. 4- 2 The MALDI-TOF mass spectrum of pure PhenethylPOSS. As matrix nitro-phenyl octyl ether with silver trifluoroacetate as salt is used. The mass difference of the peaks is about 314 Da, which is equal to the molar mass of a $(SiO_{1.5})_2R_2$ unit where R is the phenethyl group.

Fig. 4- 3 shows the dielectric loss of the pure PhenethylPOSS versus temperature and frequency in a 3-dimensional representation. The observed dielectrically active relaxation process at around 260 K is assigned to co-operative motions of PhenethylPOSS molecules in the bulk, which are related to the dynamic glass transition. This result is comparable to the measured glass transition temperature of pure PhenethylPOSS obtained by DSC (shown as the

inset of Fig. 4- 3), in which a step-like change in the thermogram about 250 K can be found.

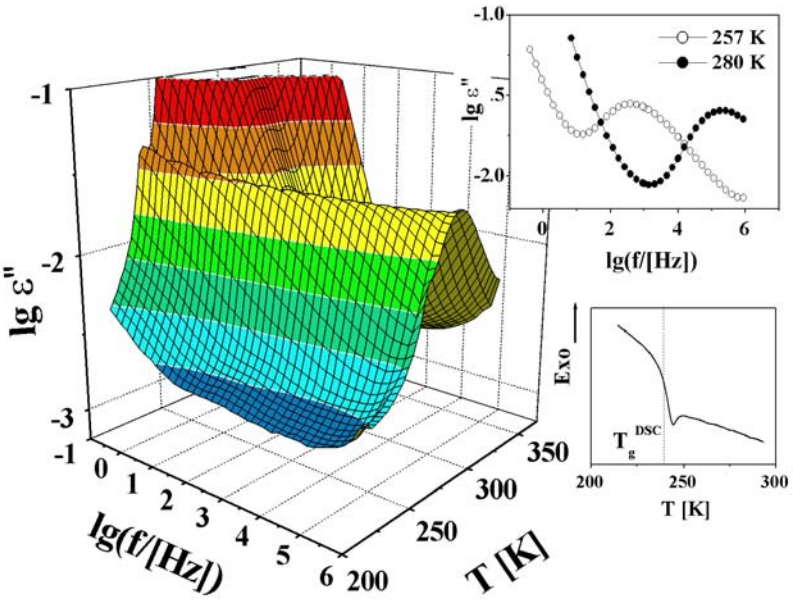

Fig. 4- 3 Dielectric loss of pure PhenethylPOSS versus temperature and frequency in a 3-dimensional representation. The inset in the upper-right part shows the frequency dependence of dielectric loss for pure PhenethylPOSS versus frequency. The inset in the lower-right part shows the DSC thermogram of the pure PhenethylPOSS.

4.1.2 ChloropropylPOSS

ChloropropylPOSS is synthesized by the partial rearrangement reaction by Dr. Rikowski in BAM.[150] The MALDI-TOF spectrum of ChloropropylPOSS reveals that the major component of the product is T8-ChloropropylPOSS (Fig. 4- 5). Its chemical structure is shown in Fig. 4- 4 .

The ChloropropylPOSS is a white powder at ambient condition. Since the powder is soluble in the $Ca(NO_3)_2$ solution, it is impossible to measure the density of ChloropropylPOSS by DGC.

The dielectric properties of the ChloropropylPOSS are investigated by BDRS. As shown in Fig. 4- 6, no dielectric active process can be observed during the experiment. Instead, above 300 K the dielectric loss of the sample shows a linear decrease with frequency, which can be related to the conductivity of the sample (section 3.1.2).

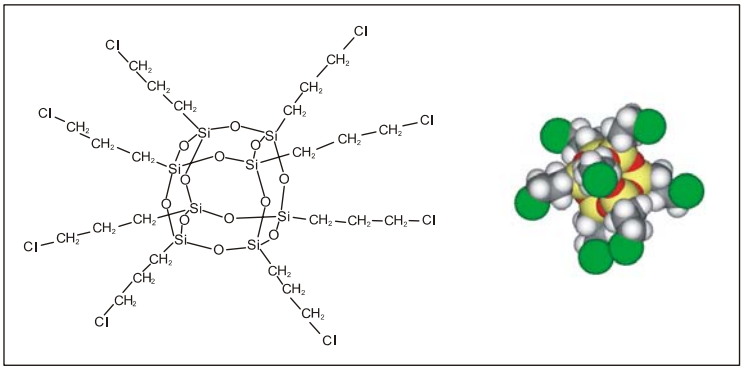

Fig. 4- 4 Left: Chemical structure (shown in the left side) of an octa-ChloropropylPOSS molecule. Right: The figure shows octa-ChloropropylPOSS as obtained by atomistic molecular modelling (hydrogen (H): white; carbon (C): grey; oxygen (O): red; silicon (Si): yellow; Chlorine (Cl): Green).

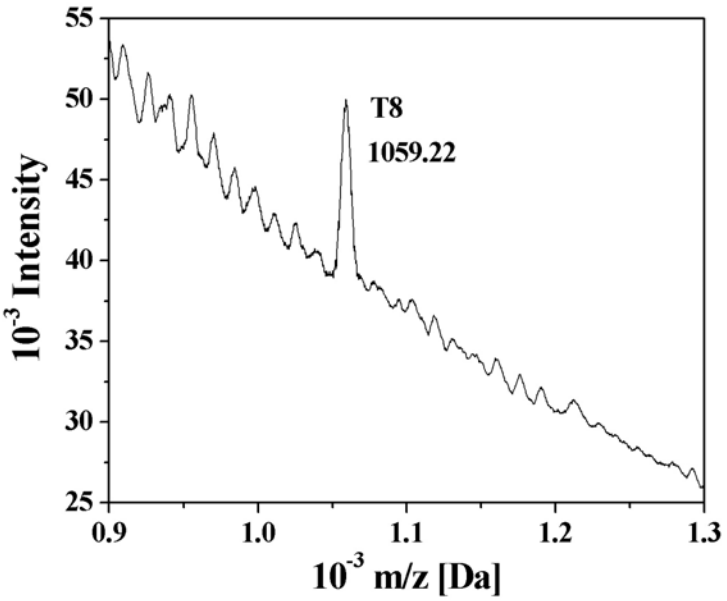

Fig. 4- 5 The MALDI-TOF mass spectra of pure ChloropropylPOSS. As matrix nitrophenyl octyl ether with silver trifluoroacetate as salt is used.

The inset of Fig. 4- 6 shows the DSC thermogram of bulk Chloropropyl-POSS. The observation of three endothermic peaks at 250 K, 400 K and 480 K indicates a complex melting behavior of the crystalline ChloropropylPOSS. Furthermore, it can be assumed that ChloropropylPOSS is partlialy melted above 250 K. As a result, the movement of charge carriers is enhanced and the conductivity of the sample is increased.

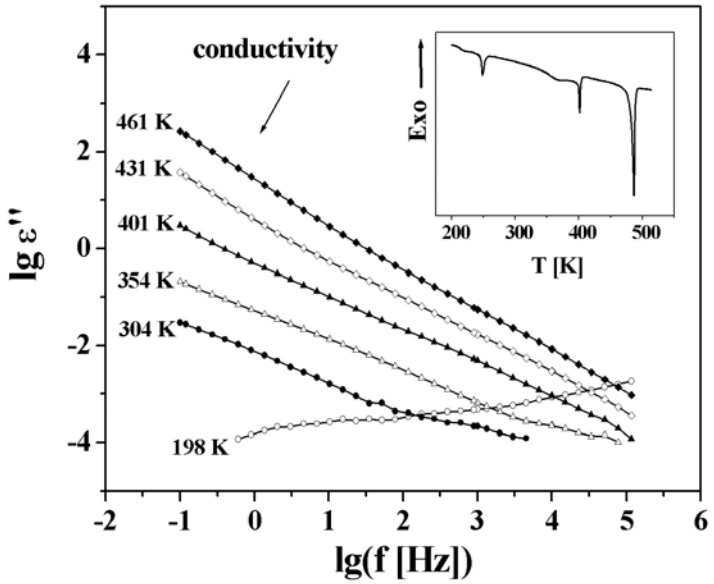

Fig. 4- 6 Dielectric loss of pure ChloropropylPOSS versus frequency at different temperatures. The inset of the plot shows the DSC thermogram of the Chloropropyl-POSS.

4.2 Matrix Polymers

4.2.1 Poly(bisphenol A carbonate)

The poly(bisphenol A carbonate) (PBAC) is one of the most important members of the polycarbonate family. It is a thermal stable material with self-distinguished property. The chemical structure of PBAC is given in Fig. 4- 7:

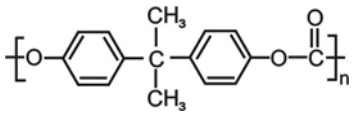

Fig. 4- 7 Chemical structure of poly(bisphenol A carbonate) PBAC

The transparent pellets of PBAC were purchased from Aldrich® and used as received. The molecular weight and molecular weight distribution was measured by GPC. The number average molar mass of the material is about 22,000 g/mol and the polydispersity (PDI) is 1.22. The density of PBAC was measured as 1.196 g/mol.

The first investigations on the relaxation properties of PBAC were accomplished by Mikhailkov and Eidelnant[151] as well as Illers and Breuer[152]

via mechanical spectroscopy. Later, Krum and Müller[153] applied dielectric spectroscopy to the study of the α-relaxation of PBAC. The glass transition temperature was reported by Schnell as 422 K.[154] Pratt and Smith constructed a three-dimensional plot of dielectric loss for PBAC (Lexane® 141) and categorized the relaxation behavior of PBAC into 8 different types.[155] Among them, the α-, β- and intermediate relaxation processes are often discussed in the literature. Tab. 4- 1 gives a brief summary of the characteristic temperature and the activation energy of these relaxations. It needs to be noted that such quantities, especially the activation energies of the relaxation, differ from each other due to the thermal histroy and preparation conditions of the sample.[156]

Tab. 4- 1 Summary of the literature data

Preparation	Testing Method	Relaxation Temperature [K]			E_a [kJ/mol]		Ref.
		α	i.m.	β	α	β	
Lexan 101, IM	D, 10 Hz	423		173	800	10~45	157
Lexan 141, TP	D				490	40, 30	158
Lexan 141, TP	D, 1k Hz	449		205	510	47	159
Lexan 143, TP	D				610	42±2	158
Lexan 145, TP	D, 1k Hz	449		205	390	49	159
Lexan 145, FC	D, 120 Hz	420		220	830	74	160,161
Lexan, FC	D			195		51, 27	162,163
Lexan, TP	M, 1.2 Hz	423		165		44	164
Lexan, TP	M, 70 Hz	423	373~393	173		43.26	165
Teijin, FC	D, 100 Hz	418		153	630	29	156
Teijin, AD	D, 3 Hz	443	393, 338	183	<462	15~18	164
Makrolon 2800, IM	D+M, 1k Hz	443	328	223		32	166
Makrolon 3000, TP	D, 1 Hz	423	343	163			167
Makrolon Mv=26000, EX	M, 1 Hz	423	333~373	193			168
Makrolon Mn=34900	M, 1k Hz	418		203			169
Mn=36000	D, 0.01 Hz	429		211		48	170
Makrolon Grade S, EX	M	433	353	163			171
Polyscience , FC	D, 10k Hz	433		213			31

Abbreviation keys: FC: film-casting; TP: thermal pressing; IM: injection molding; EX: extrusion; D: dielectric relaxation spectroscopy; M: mechanical relaxation spectroscopy; i.m.: intermediate relaxation.

The relaxation properties of the PBAC used in this experiment were investigated by dielectric relaxation spectroscopy. Fig. 4- 8 shows the temperature dependence of dielectric loss of the pure PBAC. Two relaxation

processes may be identified from the plot. The α-relaxation (the dynamic glass transition) locates in the higher temperatures and lower frequencies. It is assigned to cooperative segmental fluctuations of PBAC.

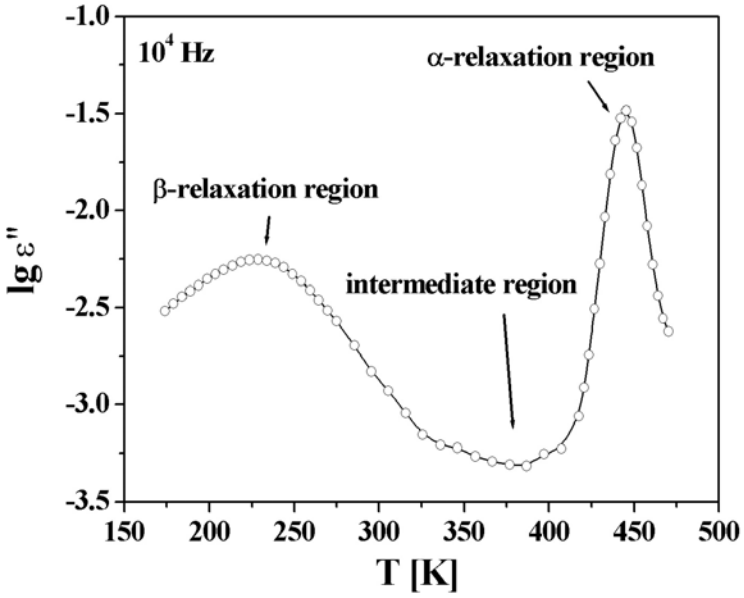

Fig. 4- 8 The temperature dependence of dielectric loss for pure PBAC at 10^4 Hz

As discussed in section 2.2.2, the β-relaxation is assigned to localized fluctuations of the polymer matrix. Early experiments reported a single, broad and symmetric β-relaxation peak, which was assigned to the superposition of two[160-163,172,173], three[174,175] or even four relaxation processes[176]. Illers and Breuer[152], Nielsen[177] as well as Watts and Perry[157] have observed symmetric β-relaxation processes in contrast to the asymmetric one (ones). The broadband nature of β-relaxation arises from a relatively strong interaction of the driven carbonyl dipole with the surrounding matrix, especially the phenyl groups. Krum and Müller[153] investigated the role of carbonyl/carbonate group in the β-relaxation region. Some subsequent experiments were carried out to give a theoretical interpretation of the localized molecular mobilities. The hindrance of carbonyl group by the restriction of the phenyl groups[164,170,178-180] and the restricted motion of the carbonate and phenyl groups were often discussed[181-185]. In addition, as the only polar group in PBAC, the fluctuation of the carbonyl groups can also be the reason of the β-relaxation.

Besides the α- and β-relaxation processes, many research groups have observed the intermediate relaxation process, which locates between the α- and the β-relaxation processes.[157,164,178-183,186,187] Most of them assigned the intermediate relaxation process to localized motions of PBAC matrix, which relate to the β-relaxation process or the cooperative motion of a specific sub-unit of polycarbonate chain.[159] Sacher attributed a wagging fluctuation of carbonate, methyl and phenyl groups to be the molecular origin for the intermediate relaxation.[182,183] It needs to be mentioned that the molecular origin of the intermediate relaxation can be attributed to many reasons and depends also strongly on the thermal history and the preparation technique of the material.[152,169] In this work, the observed intensity of the intermediate relaxation is quite small, because the PBAC samples were annealed below its T_g during the sample preparation (section 4.3). Similar results were also presented in the literature.[157,164,174,178-183,187]

4.2.2 Polystyrene

Polystyrene (PS) with various configurations can be synthesised under different conditions.[188,189] Among them, the dielectric and mechanical properties of atactic-PS were intensively investigated because of its high commercial importance.[190] In this work, the atactic-PS was purchased from Polysciences Inc as pellets. Pure polystyrene is a brittle and transparent material. Its chemical structure is shown in Fig. 4- 9.

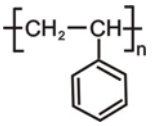

Fig. 4- 9 Chemical structure of polystyrene (PS)

The number average molar mass of the PS used in this work is about 985,000 g/mol and the polydispersity (PDI) is 2.02. The density of PS was determined by DGC as 1.045 g/mol. Its glass transition temperature was measured of 373.1 K by DSC.

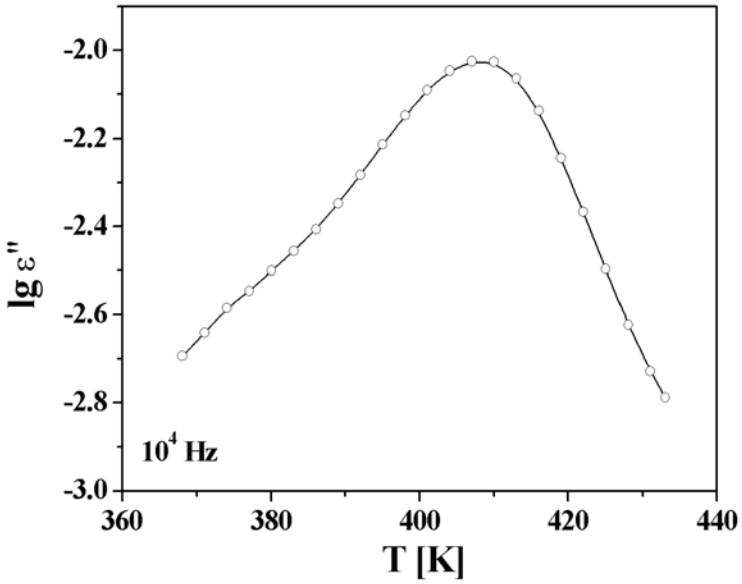

Fig. 4- 10 Dielectric loss of the pure PS versus temperature at 10^4 Hz.

The dielectric loss of bulk atactic-PS at 10^4 Hzis plotted versus temperature in Fig. 4- 10. Atactic PS is a weak polar material.[190] For pure PS, only one dielectrically active process (the α-relaxation process) can be observed at about 410 K. The α- process of PS is located in the temperature range from 393 K to 418 K, which is in agreement with literature values.[191-194]

The glass transition process of PS attracts a lot of attention due to the huge demand of flexible material for industrial applications. Blending small molecular plasticizers or nanoparticles into the PS matrix dramatically changes the physical properties of PS. In the literature, low molecular weight molecules containing phenyl-rings were used as plasticizers.[194] An example was given by Illers and Jenckel, who stated that blending phthalates into the PS matrix shifted the α-relaxation process of PS to a lower temperature region.[195] Recently, nanoscaled fillers, such as clays,[196] nanowhiskers,[197] nanoscaled $CaCO_3$,[198-200], SiO_2, layered graphite, carbon nanotubes[34] and POSS[36,37,201] were used to prepare nanocomposites. These nanocomposites show distinct modified behaviors. [202,203]

4.3 Sample Preparation

The objective of sample preparation is to form nanocomposite samples with a homogenous distribution of the nanoparticles, while the thickness of the film should be between 50 and 100 μm. This can be achieved by casting polymer solution under optimized conditions.[204,205]

The film-casting is an essential and important step since many physical properties of the film depend on the evaporation behavior of the solvent. For the PBAC-based nanocomposites, empirically, a faster evaporation causes mechanical defects or introduces crystallinity in the films, while longer evaporation times are always accompanied by sedimentation and aggregation of the nanofillers.

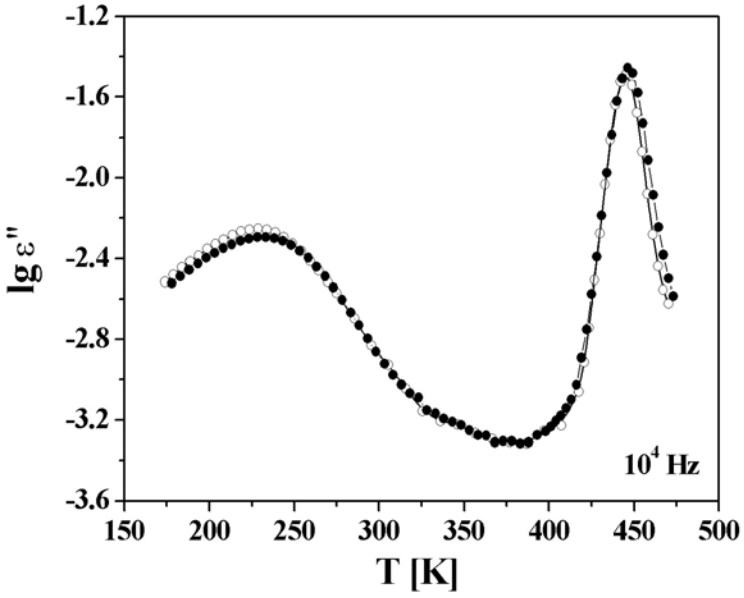

Fig. 4- 11 Dielectric loss of pure PBAC at 10^4 Hz versus temperature. Open circles and solid circles represent the spectrum of the samples with and without ultrasonic treatment.

Dichloromethane (DCM) and Chloroform (purchased from Carl Roth® GmbH, reagent grade, used as received) were used as solvent of PBAC and PS respectively. The matrix polymers were dissolved in the solvents to prepare a 15 wt% polymer solution. A selected amount of POSS was dispersed into the polymer solution. The dispersity of POSS was improved by an ultrasonification treatment (HD200/UW200 Bandelin® Sonopuls homogenizer equipped with

KE76 titanium tapered tip). The dielectric measurement showed no influence of the ultrasonification treatment on the glass transition of the polymer (shown in Fig. 4- 11).

The polymer solution was cast onto a polished glass substrate by a custom-made casting knife with a defined thickness of 500 μm. The casting procedures were carried out in a closed chamber with a solvent-rich atmosphere to control the initial evaporation rate of the solvent. After the evaporation of the organic solvent, the film was removed from the substrate by immersing film and glass support in water. The composite films were then heated up in vacuum for 24 hours to eliminate solvent residues. The heating temperature was carefully set below glass transition temperature (363 K for PBAC and 343 K for PS) in order to sustain the planarity and uniform thickness of the polymer films. The complete removal of the solvent was verified by thermogravimetric analysis. After film-casting, the sample films were cut into different shapes for the investigations. The thickness of the films was determined by an electronic thickness gauge (Mitutoyo® Corporation).

It needs to be noted that the quality of the samples should be carefully controlled after film-casting. Samples with visible defects such as mechanical bending, bubbles, aggregates or opacity, were discasded.

4.4 Sample Descriptions

PBAC and PS were used as matrix polymers. Molecular Silica POSS with high polarity (ChloropropylPOSS) and low polarity (PhenethylPOSS) substituents were used as filler materials (section 4.1). Blending ChloropropylPOSS into PS dramatically enhances the brittleness of the sample. This may be due to the aggregation of POSS crystallites during the evaporation of the solvents. For this reason, the PS-based ChloropropylPOSS nanocomposites were excluded from the sample preparation.

Tab. 4- 2 compares the brittleness and transparency of these nanocomposite films under same conditions. As presented by Wu and Wicks,[45] adding POSS molecules into matrix polymers reduces the optical transparency of the sample.

In addition, the flexibility of the PBAC/PhenethylPOSS is enhanced as the concentration of the POSS increases.

Tab. 4- 2 The physical properties of the sample films

	PhenethylPOSS	**ChloropropylPOSS**
PBAC	enhanced flexibility slightly reduced transparency	reduced flexibility reduced transparency
PS	reduced flexibility slightly reduced transparency	very brittle visible aggregation of ClPOSS

The details of the samples are listed in the Tab. 4-3. The sample code consists of 5 or 6 letters. The pure PBAC and PS are named as PC000 and PS000 respectively. For the nanocomposites, the first three letters stand for the content of the sample. Here, PCP, PCC and PSP are the PBAC/PhenethylPOSS, PBAC/ChloropropylPOSS and PS/PhenethylPOSS nanocomposites. The digits indicate the weight fraction of the POSS molecules in the nanocomposite.

Infrared spectroscopy was applied to determine the POSS content in the nanocomposites. The IR spectra of the matrix polymer, the Molecular Silica and the nanocomposites are presented in Fig. 4- 13 to Fig. 4- 15. In these plots a series of characteristic adsorption peaks can be identified.[52,206,207] The details are listed in Tab. 4- 3.

Tab. 4- 3 The characteristic bands of the IR spectra

wave number [cm^{-1}]	Description	Samples
1103	symmetrical vibration of the -C-O-C-	PBAC
1078	-Si-O-Si-	POSS
1159 to 1216	asymmetrical vibration of the -C-O-C-	PBAC
1452 and 1496	$-CH_2-$	PS, PhenethylPOSS
1502	-OC-O-CO-	PBAC
1764	C=O	PBAC
around 3000	C-H bonds of the phenyl rings	PS, PhenethylPOSS

It needs to be mentioned that the intensity of the IR spectra of the pure PhenethylPOSS is higher than that of the polymer films. That is because the pure PhenethylPOSS was investigated by ATR techniques (section 3.3.2), where a different degree of contact between sample and ‘substrate’ leads to observed difference in the infrared intensity.

Tab. 4- 4 List of the samples used in the measurements

Code	Concentration			DGC	DSC	FTIR	BDRS	GP	GS
	wt%	mol%	vol%	ρ [g/cm^3]	T_g [K]				
PC000	0	0	0	1.196	422.0	x	x	x	x
PS000	0	0	0	1.045	373.1	x	x	--	x
PCP001	1.0	0.1	1.0	1.194	416.2				
PCP002	2.4	0.2	2.3	1.178	412.3		x		
PCP005	4.8	0.4	4.7	1.180	411.0		x	x	
PCP010	9.1	0.8	8.9	1.180	406.5	x	x	x	x
PCP013	13.0	1.1	12.7	1.182	406.2		x	x	
PCP014	14.0	1.2	13.9	1.195	405.8				
PCP015	15.3	1.3	15.2	1.199	405.2				
PCP017	16.7	1.4	16.7	1.206	403.0	x	x	x	x
PCP023	23.1	2.0	23.1	1.209	402.4	x	x	x	x
PCP029	28.6	2.5	28.6	1.211	402.4	x	x	x	x
PCP033	33.3	3.0	33.3	1.212	397.7	x	x	x	x
PCP041	41.2	3.8	41.2	1.209	399.4	x	x	x	x
PCC002	2.4	0.2	--	1.196	416.2	x			
PCC005	4.8	0.5	--	1.200	416.7	x	x		
PCC010	9.1	0.9	--	1.215	415.3	x		x	x
PCC013	13.0	1.3	--	1.218	413.5	x	x		
PCC017	16.7	1.7	--	1.231	412.7	x	x	x	x
PCC023	23.1	2.4	--	1.246	403.1	x	x	x	x
PCC029	28.6	3.0	--	1.251	414.1	x	x		
PCC033	33.3	3.6	--	1.262	415.6	x	x		
PSP005	4.7	0.5	4.1	1.062	362.3	x	x	--	
PSP010	9.1	1.0	8.1	1.072	358.0	x		--	x
PSP013	13.1	1.4	11.8	1.077	355.9	x	x	--	x
PSP022	22.1	2.6	20.2	1.082	351.7	x	x	--	x
PSP032	31.9	4.3	29.8	1.101	343.0	x	x	--	--
PSP038	38.3	5.5	36.5	1.126	325.8		x	--	--

Abbreviations: DGC: Density Gradient Column, DSC: Differential Scanning Calorimetry, FTIR: Fourier Transform Infrared Spectroscopy, BDRS: Broadband Dielectric Relaxation Spectroscopy, GP: Gas Permeation Measurements, GS: Gas Sorption Measurements. --: not possible to measure

In the IR spectra of pure PBAC and PBAC-based nanocomposites, a strong adsorption band at 1764 cm^{-1} is assigned to the C=O groups of the PBAC backbone. The peak at 1103 cm^{-1} is due to symmetric vibration of the –C-O-C- group, while the double peak structure at 1159 and 1216 cm^{-1} is assigned to the asymmetric vibration of the –C-O-C- group.

According to the literatures,[52,206,207] the absorption peak of the -Si-O-Si- group is located at around 1100 cm^{-1}. In the IR spectra of the bulk Molecular Silica samples, it corresponds to the adsorption peak at 1078 cm^{-1} (Fig. 4- 13 and Fig. 4- 15). In the polymer-based nanocomposites, it is observed that the intensity of the peak at 1099 cm^{-1} is increasing with increasing POSS content. Therefore this band is used to characterize the content of POSS in the nanocomposites. Since this band overlaps with adsorption bands of pure PBAC in the same wave number range, in practice, the intensity of this peak was estimated as the difference between the peak area at 1099 cm^{-1} of the nanocomposites and the pure PBAC (shown as A_2-A_1 in Fig. 4- 12).

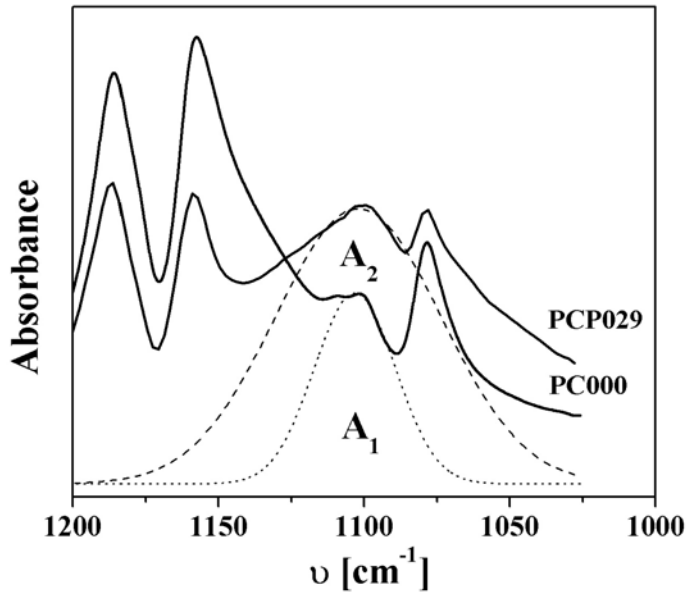

Fig. 4- 12 An example of determining the intensity of -Si-O-Si- peak from the IR spectra. For pure PBAC (PC000) and PBAC-based PhenethylPOSS nanocomposite (PC029), their spectra at 1099 cm^{-1} are fitted by a Gaussian function. A_1 and A_2 are the area of the peaks. The intensty of -Si-O-Si- peak in PCP029 is calculated from the difference of the peak areas (A_2-A_1).

For PBAC-based nanocomposites, the ratio of the absorbance A_{1099}/A_{1764} is plotted over the molar ratio of the Molecular Silica and the matrix polymer (shown in Fig. 4- 16A and Fig. 4- 16B). The characteristic band ratios have linear relations to the molar ratio of POSS to PBAC as Eq. 4-1 and Eq. 4- 2 described.

In the IR spectra of PS-based PhenethylPOSS nanocomposite, the band at 1099 cm^{-1} is used as the characteristic band for the content of POSS. However,

the analysis of PS-based PhenethylPOSS nanocomposite is more complicated because the characteristic bands of PS all overlap with that of bulk Phenethyl-POSS. Here one needs to make a simple assumption that the molar fraction of PhenethylPOSS molecules is small and therefore can be neglected (see Tab. 4-3). In this case, the characteristic bands at 3000 cm^{-1} are used as characteristic bands for polystyrene. The intensity ratio of these characteristic bands A_{1099}/A_{3000} is then plotted versus their molar ratio in Figure Fig. 4- 16c. The data points of the plot can be fitted as a linear function given by:

$$\frac{\text{mol\%}\,(\text{PhenethylPOSS})}{\text{mol\%}\,(\text{PBAC})} = 0.125 + 1.850\left(\frac{A_{1099}}{A_{1764}}\right), \qquad \textbf{Eq. 4- 1}$$

$$\frac{\text{mol\%}(\text{ChloropropylPOSS})}{\text{mol\%}(\text{PBAC})} = -0.084 + 4.642\left(\frac{A_{1099}}{A_{1764}}\right). \qquad \textbf{Eq. 4- 2}$$

$$\frac{\text{mol\%}(\text{PhenethylPOSS})}{\text{mol\%}(\text{PS})} = -0.178 + 0.619\left(\frac{A_{1099}}{A_{3000}}\right). \qquad \textbf{Eq. 4- 3}$$

Eq. 4-1 to Eq. 4-3 confirm that the molar concentration of the POSS inside the nanocomposites is equal to that of the formulation. Moreover, these equations present a simple method to estimate the molar concentration of the POSS molecules in the nanocomposites based on the infrared spectra.

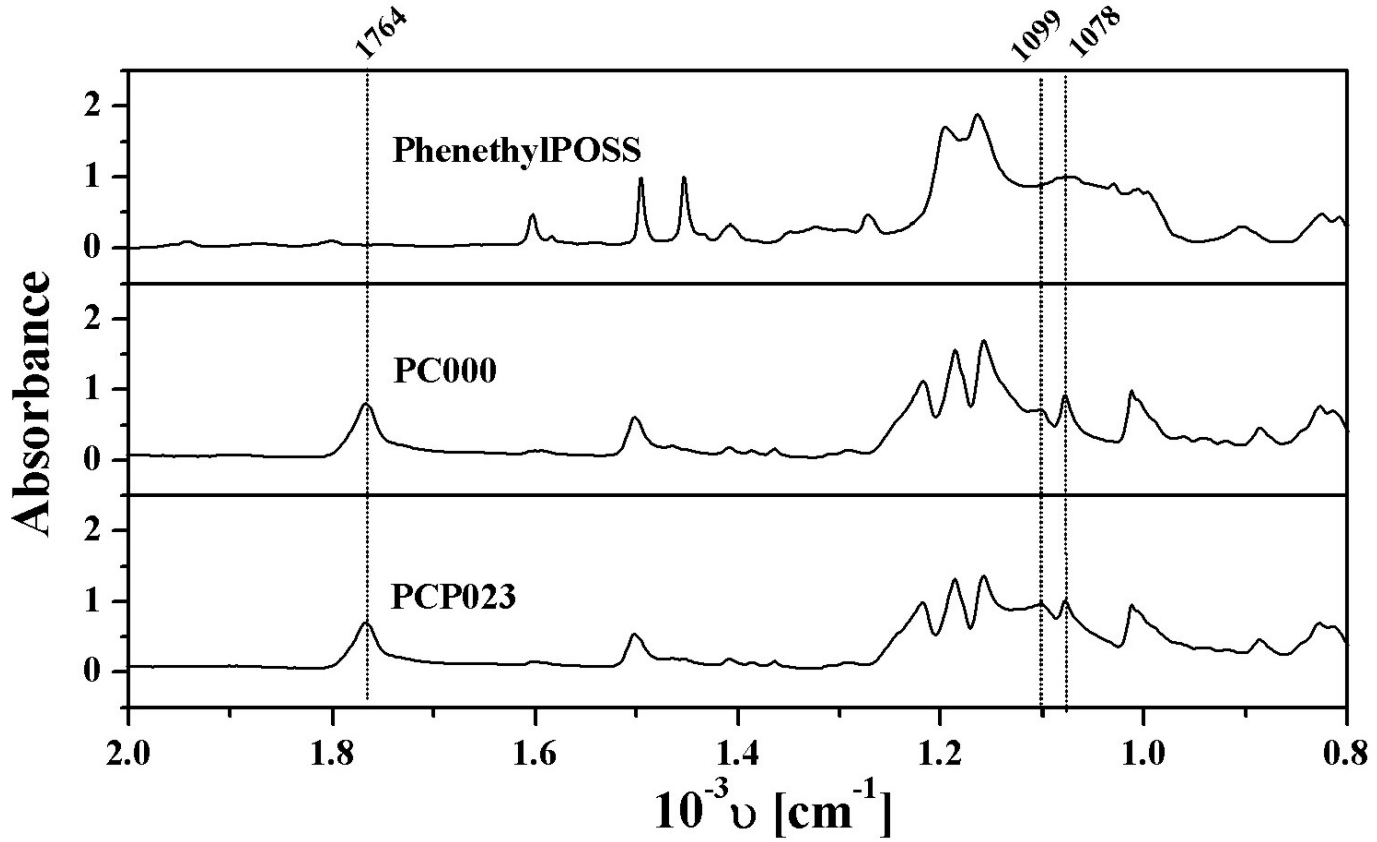

Fig. 4- 13 IR spectra of PhenethylPOSS, pure PBAC (PC000) and PBAC-based PhenethylPOSS nanocomposite (PCP023)

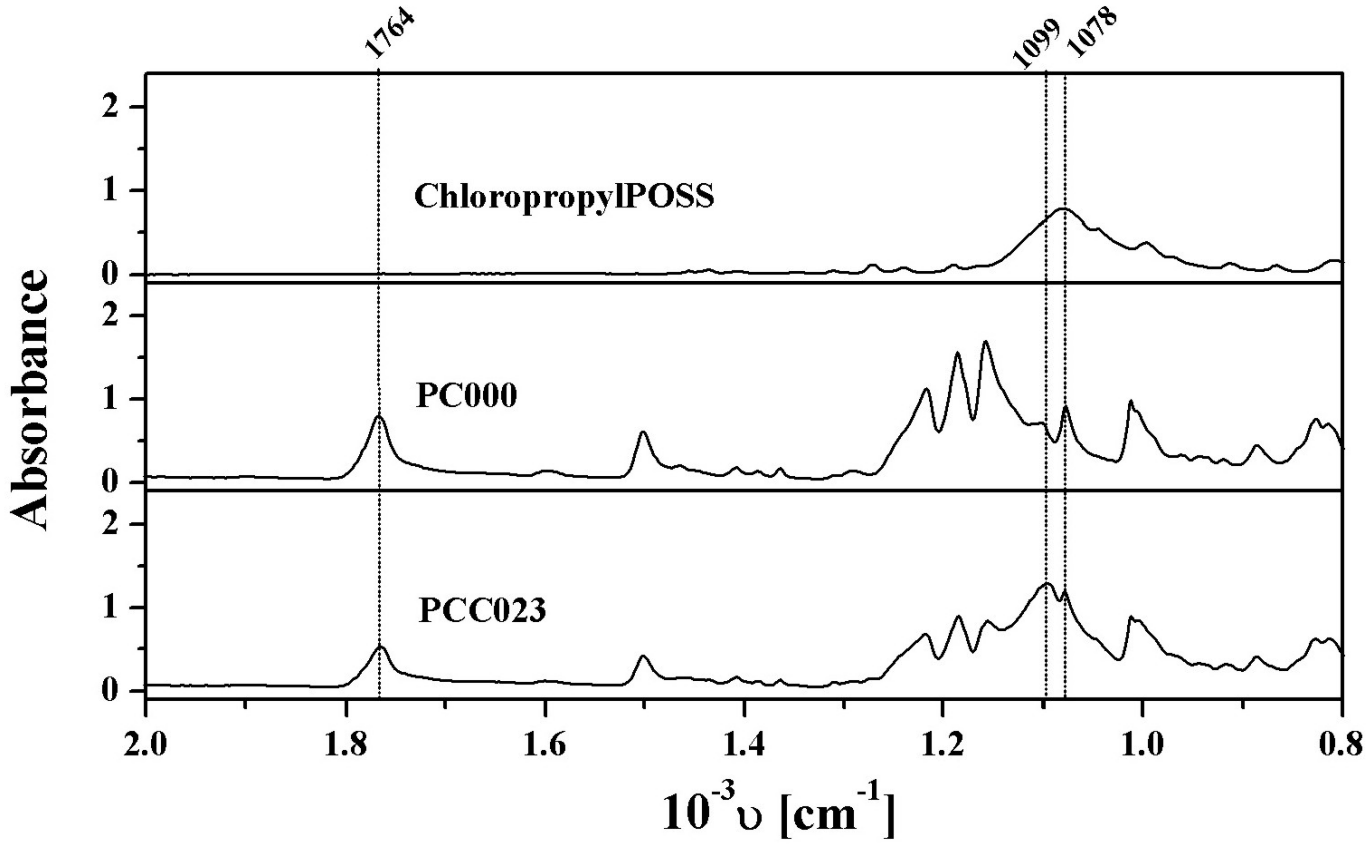

Fig. 4- 14 IR spectra of ChloropropylPOSS, pure PBAC and PBAC-based ChloropropylPOSS nanocomposite (PCC023)

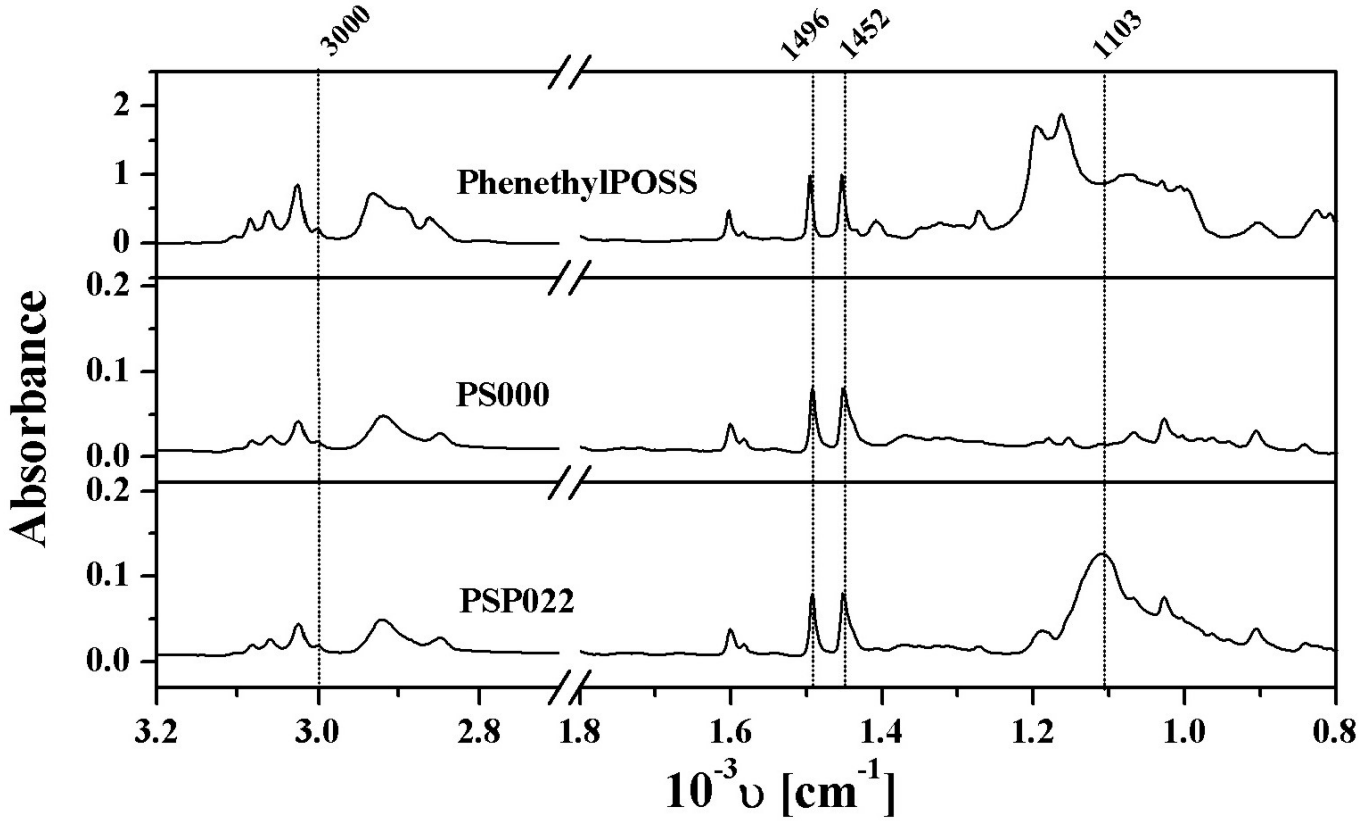

Fig. 4- 15 IR spectra of PhenethylPOSS, pure PS (PS00) and PS-based PhenethylPOSS nanocomposite (PSP022)

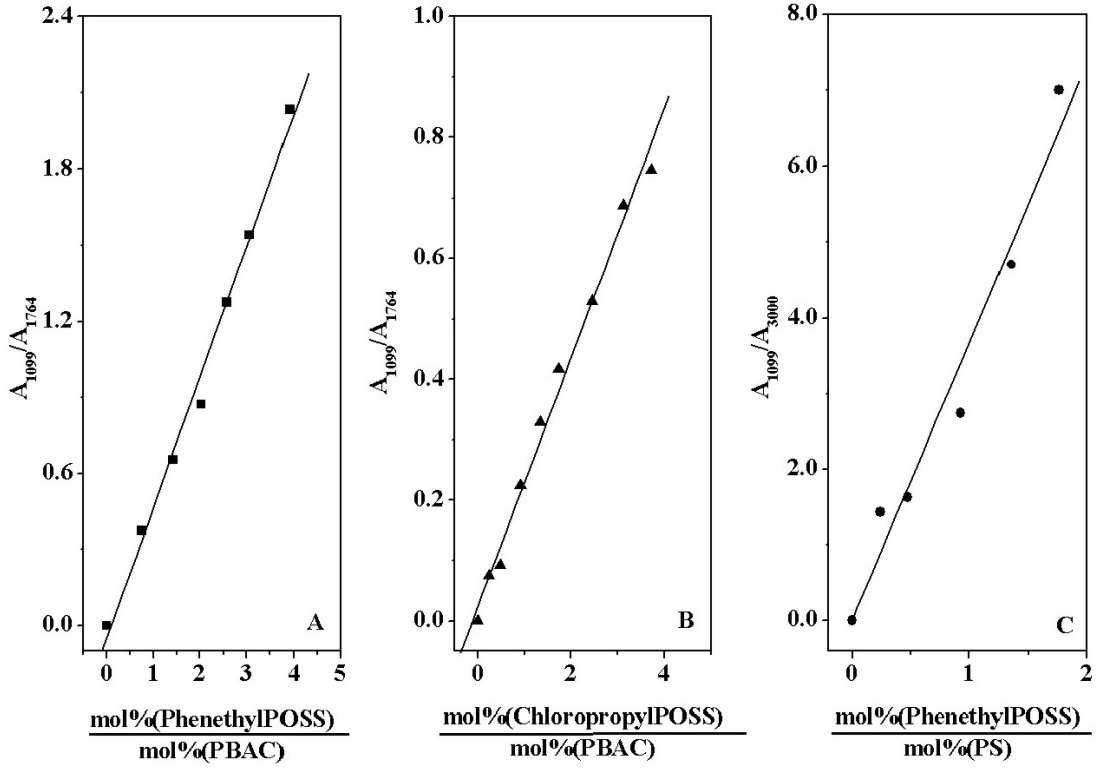

Fig. 4- 16 Intensity ratio of the characteristic adsorption peaks versus the molar ratio of the components of the nanocomposites. A: PBAC-based PhenethylPOSS nanocomposites; B: PBAC-based ChloropropylPOSS nanocomposites; C: PS-based PhenethylPOSS nanocomposites The data were fitted by a linear function.

5 Results and Discussions

5.1 Dielectric Investigation of Nanocomposites

As discussed in section 4.4, the structure-property relationships of the three different polymer-based nanocomposites (Tab. 4- 2 and Tab. 4- 4) were investigated by dielectric measurements. The change of the complex dielectric function ε* was recorded as a function of frequency and temperature. The relaxation properties of each process were discussed in the frequency domain by fitting model functions to the spectrum. The changes of the molecular mobility were analyzed in terms of compatibility and the packing structure of the POSS molecules as well. Furthermore, they were discussed further in the framework of morphological changes of the nanocomposites in the following sections.

5.1.1 Nanocomposites based on PhenethylPOSS

5.1.1.1 PBAC-based PhenethylPOSS Nanocomposites

Fig. 5- 1 shows the dielectric spectra of the pure PBAC sample (PC000) and the PBAC-based PhenethylPOSS nanocomposite (PCP005) in its temperature and frequency dependence. In contrast to the pure PBAC (shown also in Fig. 4- 8), both the α- and β-relaxation processes of PCP005 are shifted to lower temperatures. Fig. 5- 1b compares the frequency-dependent dielectric spectra of PC000 and PCP005 at 433 K. For both samples, only one single relaxation process can be observed at this temperature. This indicates that the PhenethylPOSS molecules are miscible within PBAC matrix on a molecular level up to the considered concentration of 4.8 wt%.

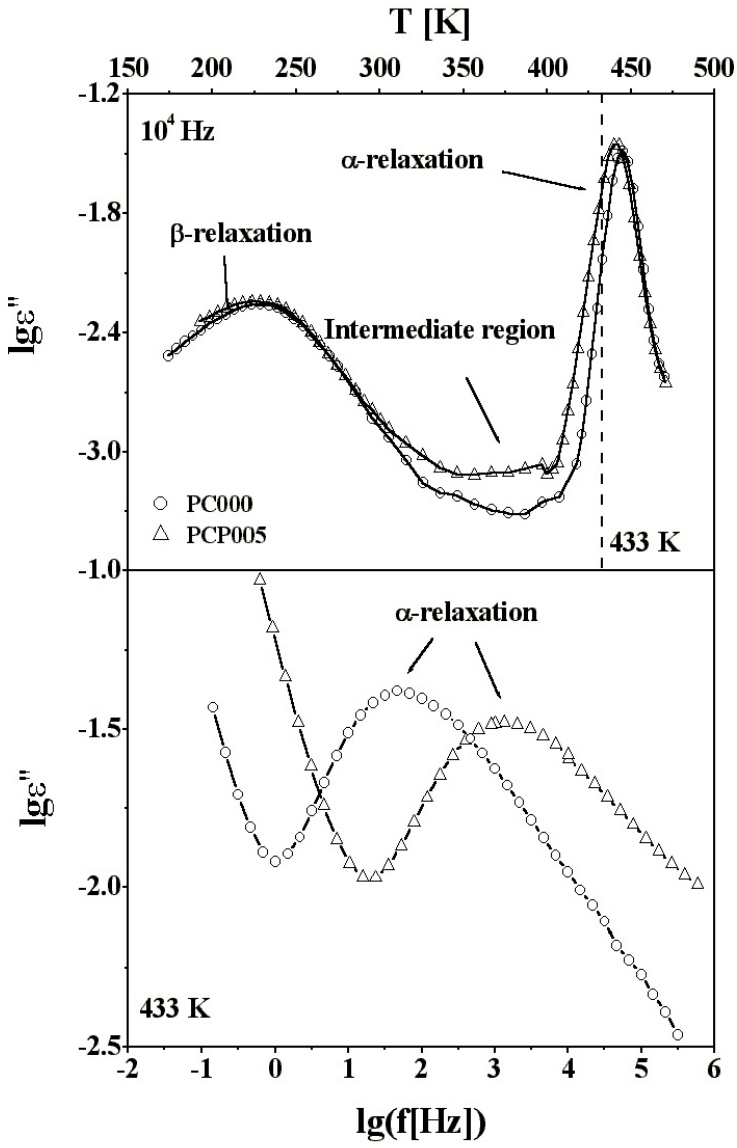

Fig. 5- 1a: Dielectric loss of the pure PBAC (open cycles) and the PBAC-based Phenethyl-POSS nanocomposite (5 wt%, empty triangles) versus temperature at 10^4 Hz. b: Dielectric loss of same samples versus frequency at 433 K.

As the concentration of PhenethylPOSS is increasing, the characteristic temperature of the α-peak shifts to lower temperatures (Fig. 5- 1a). This is in agreement with the change of glass transition temperature measured by DSC in the same concentration region (shown in Tab. 4- 4). This effect is called plasticization. A similar behavior was reported for the nanocomposite systems prepared by PMMA and POSS with acrylic, cyclohexyl or isobutyl substituents.[11-13,20]

It should be mentioned that the mechanism of the plasticization of the matrix polymer PBAC by PhenethylPOSS is quite different from that caused

by low molecular weight molecules. As discussed in section 4.1, the Phenethyl-POSS molecule is quite bulky (Fig. 4- 1). The equilibrated molecular model of PhenethylPOSS reveals that the orientation of phenyl rings is perpendicular to the silica core. The rearrangements of the rings are hindered by the short -CH_2-CH_2- groups. Therefore, such mobility changes give dense packing structure to the POSS molecules. For this reason, at low concentrations, the packing density of the surrounding matrix is decreased with the POSS concentration, which corresponds to an increase of local free volume. This line of argument is supported by the density measurements (Fig. 5- 2). At low concentrations of PhenethylPOSS, the density of the nanocomposite is strongly reduced compared to pure PBAC, which corresponds to an increase of free volume.

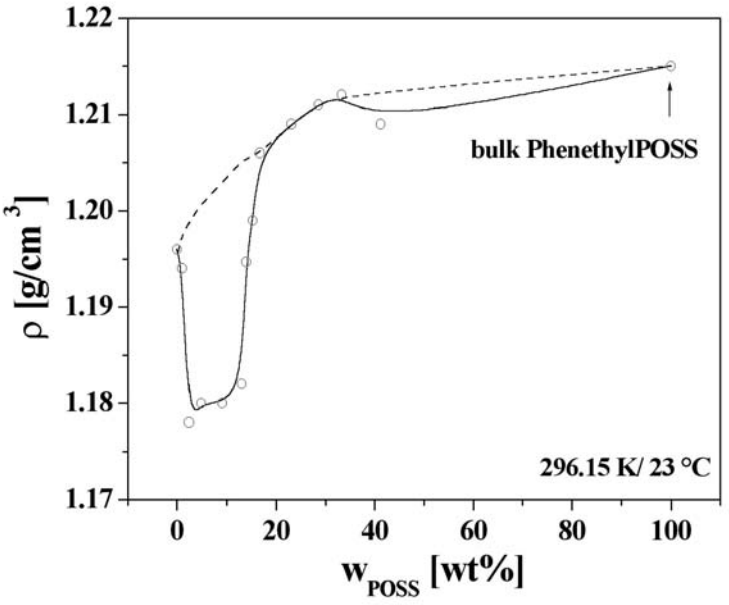

Fig. 5- 2 The density of PBAC-based PhenethylPOSS nanocomposites versus the concentration of PhenethylPOSS. The dashed line may characterize the change of density of an additive system.

Fig. 5- 3 shows the dependence of the relaxation rate f_p versus reciprocal temperature for lower POSS concentrations (up to 17 wt%). As shown in the plot, the curves shift to lower temperatures with increasing content of PhenethylPOSS. The data were fitted by the VFTH function (Fig. 5- 3) and the fitting parameters were summarized in Tab. 5- 1. As shown in Fig. 5- 3, the dynamic glass transition temperature T_g^{Diel} can be calculated as the temperature at 1 Hz.

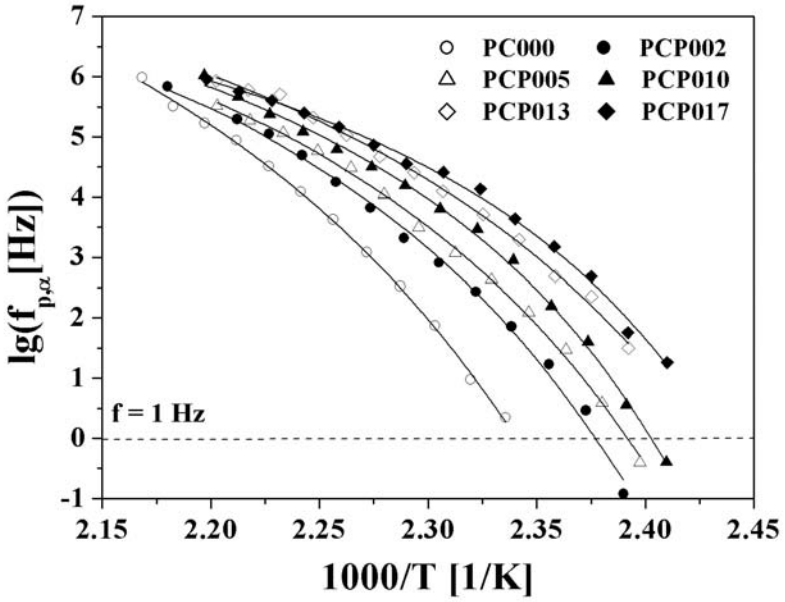

Fig. 5- 3 Relaxation rate $f_{p,\alpha}$ versus reciprocal temperature. The data were fitted by the VFTH function and the fitting parameters are listed in the shaded part of Tab. 5- 1. The dynamic glass transition temperature T_g^{Diel} was estimated at 1 Hz.

Tab. 5- 1 FVTH fitting parameters of the pure PhenethylPOSS, the pure PBAC (PC000) and PBAC-based nanocomposites

Sample Code	α-relaxation		
	$lg(f_\infty$ [Hz])	A [K]	T_0^{id} [K]
PhenethylPOSS	11.4	334.0	218.2
PC000	13.7	611.3	382.6
PCP002	11.6	437.7	382.8
PCP005	11.0	386.7	383.0
PCP010	10.4	311.8	386.1
PCP013	11.3	422.8	374.6
PCP017	9.3	236.4	386.0
PCP023	10.7	245.9	399.9
PCP029	10.8	246.1	398.6
PCP033	9.4	182.6	398.6
PCP041	10.6	311.1	384.8

In Fig. 5- 4, the dielectric loss of samples with higher PhenethylPOSS concentration (PCP010, PCP033) is compared with that of the pure PBAC in dependence of temperature and frequency, respectively. In the temperature dependent domain, blending POSS molecules does not shift the α-relaxation process of the nanocomposite to lower temperatures. In addition, a double peak structure can be identified around the glass transition region. The one at lower

temperatures forms a shoulder-like structure (called α´-relaxation in Fig. 5- 4). Such a double-peak structure exists also in the frequency domain (Fig. 5- 4b) and can be interpreted in terms of a phase separation. Due to the strong overlap of the peaks, only the α-relaxation is suitable to be analyzed in the full temperature range. Similar to the samples with lower concentration of PhenethylPOSS, the α-relaxation is assigned to PBAC-rich domains with dissolved Phenethyl-POSS molecules.

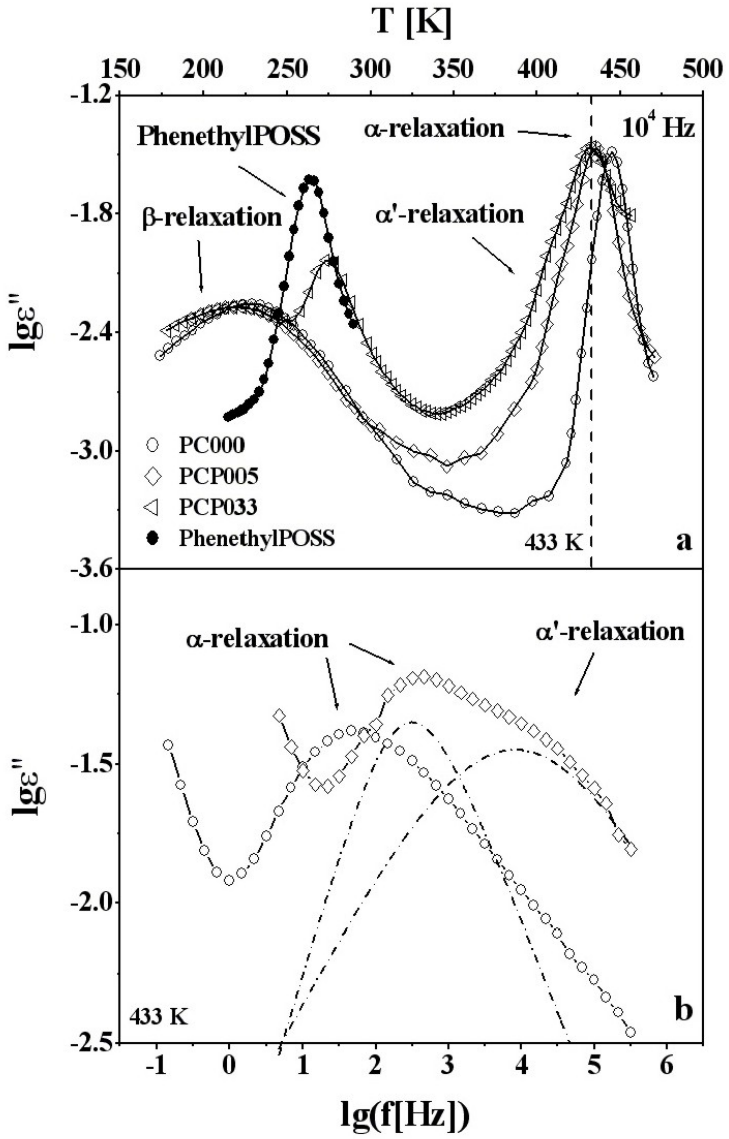

Fig. 5- 4 a: Dielectric loss of the pure PBAC (PC000), PBAC-based nanocomposites (PCP010 and PCP033) and the pure PhenethylPOSS versus temperature at 10^4 Hz. b: Dielectric loss of pure PBAC (PC000) and PBAC-based PhenethylPOSS nanocomposite (PCP010) versus frequency at 433 K. The spectrum of PCP010 is fitted as a superposition of two HN functions (shown as the dash-dotted lines).

The analysis of the α-relaxation processes is carried out by fitting the HN function (Eq. 2- 33) to the experimental results. For the calculations, the parameter γ value is held constant to reduce the number of fitting parameters.

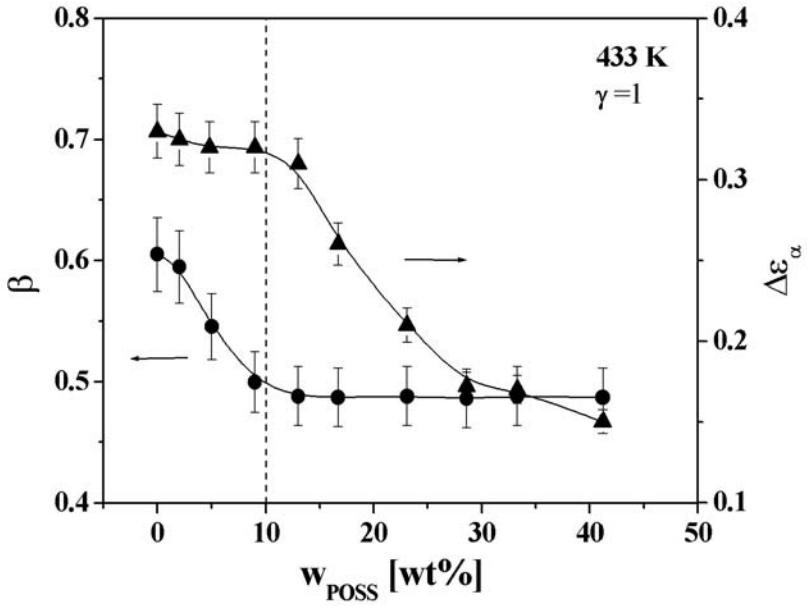

Fig. 5- 5 Fitting parameters β (full circles) and $\Delta\varepsilon_\alpha$ (full triangles) of α-relaxation process versus the concentration of PhenethylPOSS at 433 K. Lines are drawn to guide the eyes.

The symmetric broadening parameter β and the relaxation intensity $\Delta\varepsilon_\alpha$ are plotted in Fig. 5- 5 versus PhenethylPOSS concentration. The decrease of $\Delta\varepsilon_\alpha$ observed at a concentration of 10 wt% may be ascribed to changes of the effective dipole moment because the low polarity PhenethylPOSS molecules are incorporated into the PBAC matrix. On the other hand, the symmetric broadening parameter β of the α-relaxation process decreases with the POSS concentration up to 10 wt%. This means the α-peak becomes broader in this concentration region (Fig. 5- 1a). For higher concentrations (w_{POSS} > 10 wt%), the β value reaches its minimum of about 0.5. This implies that at higher concentrations, the width of the dynamic relaxation peak does not depend on POSS concentration. This conclusion agrees with the observation in Fig. 5- 4a, where the broadening of the α-relaxation process at higher temperature is attributed to the superposition of the α´-peak.

In Fig. 5- 4a, a new peak is observed in the lower temperatures. The characteristic temperature of the peak is located at around 260 K, which is

close to the glass transition temperature of pure PhenethylPOSS. In addition, as the concentration of POSS increases, the relaxation intensity of this peak increases. For these reasons, this process is assigned to cooperative motions of PhenethylPOSS molecules in POSS-rich domains.

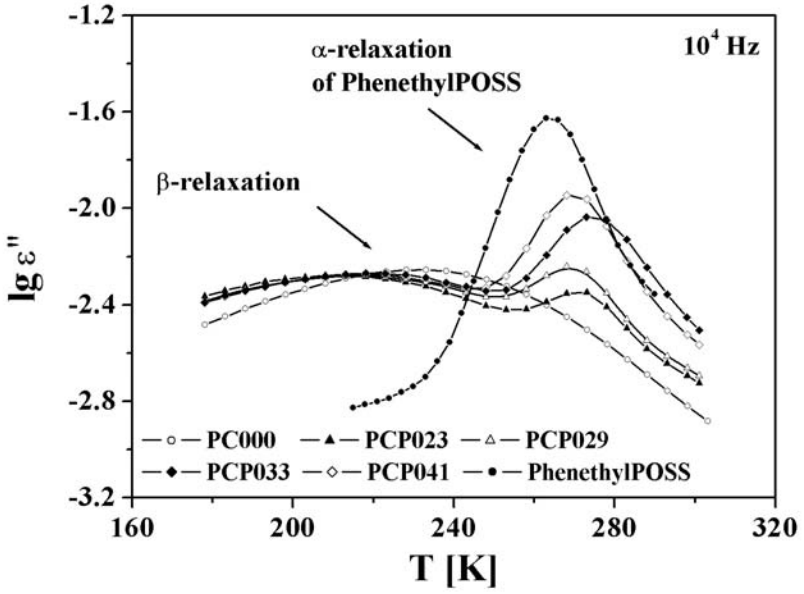

Fig. 5- 6 Dielectric loss of the pure PBAC (PC000), PBAC-based nanocomposites (PCP023 to PCP041) and the pure PhenethylPOSS versus temperature at 10^4 Hz in lower temperatures.

The α′-process is located at slightly lower temperatures than the α-relaxation. It is therefore concluded that this process is related to cooperative motions of PBAC segments but with more PhenethylPOSS molecules involved in the relaxation processes. According to the Gibbs phase rule, the number of possible phases at constant temperature and pressure is two. Therefore, this relaxation process can be assigned to an interfacial layer between POSS-rich domains and PBAC-rich domains. To have a signature in the dielectric spectra the interfacial layer should have a certain extent. To be visible in the dielectric spectrum, the characteristic size of this interfacial layer is assumed to be in the range between 1 and 3 nm.[70]

It can be further concluded from the relaxation experiments that for higher concentrations of PhenethylPOSS, the nanocomposite exhibits a two-phase structure consisting of a PBAC-rich phase and a POSS-rich phase. Both phases are separated by an interfacial layer as stated above (shown in Fig. 5- 7).

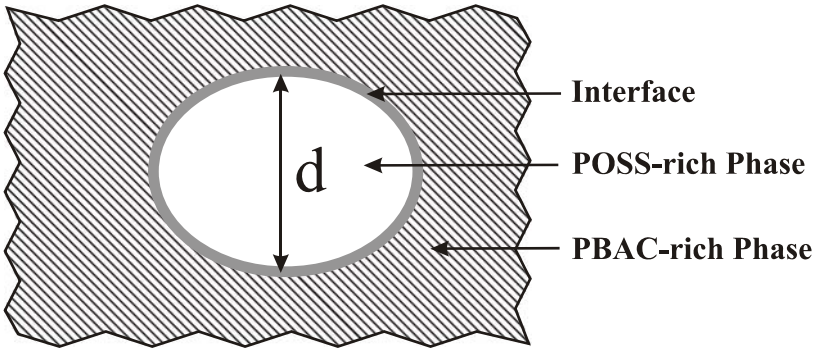

Fig. 5- 7 A schematic illustration of the phase separation at higher concentrations. The parameter d is used to characterize the size of the PhenethylPOSS-rich domain.

The discussed phase morphology is also supported by the change of density of the sample with POSS concentration. For low concentrations of Phenethyl-POSS, the density of the nanocomposites is decreasing with the concentration of PhenethylPOSS (Fig. 5- 2). This is because of the increase of free volume due to the blending of PhenethylPOSS molecules.

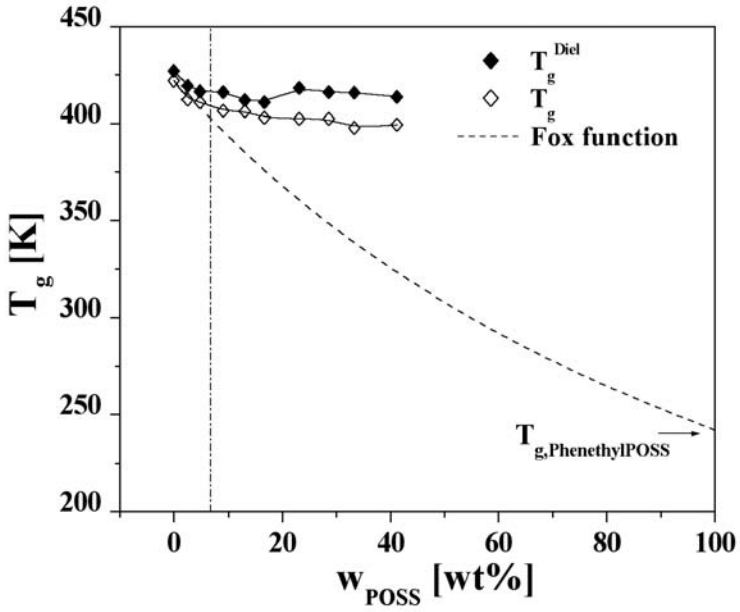

Fig. 5- 8 T_g and T_g^{Diel} of PBAC-based PhenethylPOSS nanocomposites versus Phenethyl-POSS concentration w_{POSS}. Solid lines are drawn to guide the eyes. The dashed line shows the prediction given by the Fox function (Eq. 5- 1).

For higher concentrations (w_{POSS}>10 wt%), this increase of free volume is compensated by the formation of a POSS-rich phase having approximately the same density as Phenethyl-POSS. As a result, the density of the sample is strongly increased and approaches a line, which may be predicted for a simple two-phase system.

$$\frac{1}{T_g} = \frac{w_{PBAC}}{T_{g,PBAC}} + \frac{w_{POSS}}{T_{g,POSS}}, \quad w_{PBAC} + w_{POSS} = 1 \qquad \textbf{Eq. 5- 1}$$

Plotting the glass transition temperature T_g (data are taken from Tab. 4- 4) and the dynamic glass transition temperature T_g^{Diel} versus the POSS concentration, the micromorphology of the nanocomposites can be summarized in the phase diagram shown in Fig. 5- 8. The Fox function (Eq. 5- 1) is given in the same figure. The Fox function describes the glass transition temperature of the composites, whose components are miscible on the molecular level.

The measured T_g^{Diel} values are about 20 to 30 K higher than T_g but share a similar trend of decreasing with concentration since both describe the same process but in different frequency scales. Below 7 wt%, the measured T_g values coincide with the Fox-expectation indicating the PhenethylPOSS molecules are dissolved on a molecular level. For the samples with higher POSS concentrations, the decreased T_g value reaches its minimum value and becomes constant. It can be concluded that the PhenethylPOSS molecules can be dissolved into PBAC on a molecular level up to a concentration of about 7 wt%. Above 20 wt%, a slight increase of T_g^{Diel} value indicates the existence of interfacial layers.

β-relaxation Processes

For PBAC-based PhenethylPOSS nanocomposites, as the concentration of PhenethylPOSS increases, the β-process shifts to lower temperatures (Fig. 5- 1 and Fig. 5- 4). This is in contrast to conventional polymer-based low molecular weight filler composites, where the opposite effect, a shift of the β-relaxation to higher temperatures can be observed.[208] This result supports the conclusion that the plasticization of the PBAC matrix by PhenethylPOSS is different from that of a low molecular weight plasticizer.

The temperature dependence of the relaxation rate of the β-relaxation $f_{p,\beta}$ obeys the Arrhenius equation. Thus the activation energy $E_{A,\beta}$ can be estimated by fitting Eq. 2- 2 to the data (inset of Fig. 5- 9). In Fig. 5- 9, the value of $E_{A,\beta}$ is plotted versus the weight fraction of PhenethylPOSS.

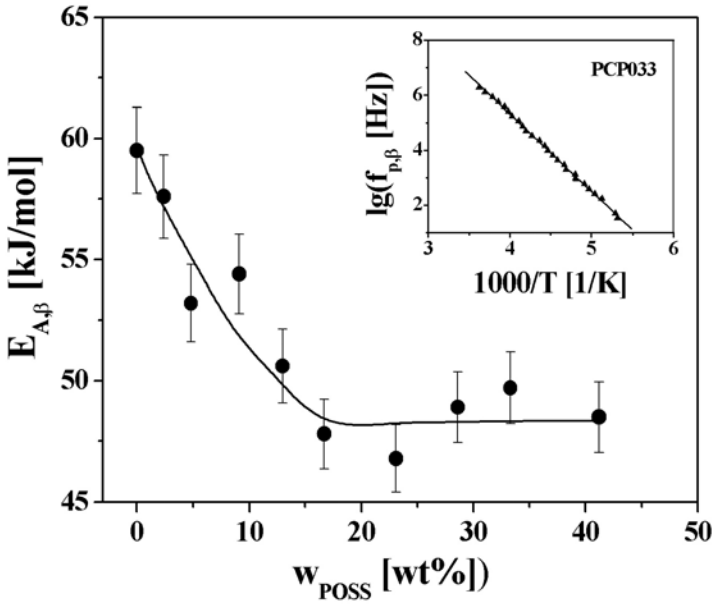

Fig. 5- 9 Activation energy $E_{A,\beta}$ versus concentration of PhenethylPOSS. Lines are drawn to guide the eyes. The $E_{A,\beta}$ is calculated by fitting the Arrhenius function to the relaxation rates (An example is shown in the inset).

Up to 10 wt%, the activation energy decreases with increasing concentration of PhenethylPOSS. This can be attributed to the increase of the localized free volume due to the reduced packing density. Above 10 wt%, the $E_{A,\beta}$ value remains constant. Such a result is in agreement with the conclusion of the phase diagram given in Fig. 5- 8, which assumes the solubility of Phenethyl-POSS reaching its saturation level in PBAC at 7 wt%.

The Maxwell-Wagner-Sillars Polarization Process

For the nanocomposites with higher POSS concentration, a pronounced peak is observed as superposition of the α-relaxation peak in the lower frequencies. Compared with the α-relaxation, this peak is characterized by a relatively narrow distribution of relaxation times and a high intensity (Fig. 5-10). Moreover, in the same frequency range, the real part of the dielectric function (ε´) of the samples shows a dramatic increase in lower frequencies. Therefore, this relaxation process is interpreted as the Maxwell-Wagner-Sillars polarization (section 2.3.4).

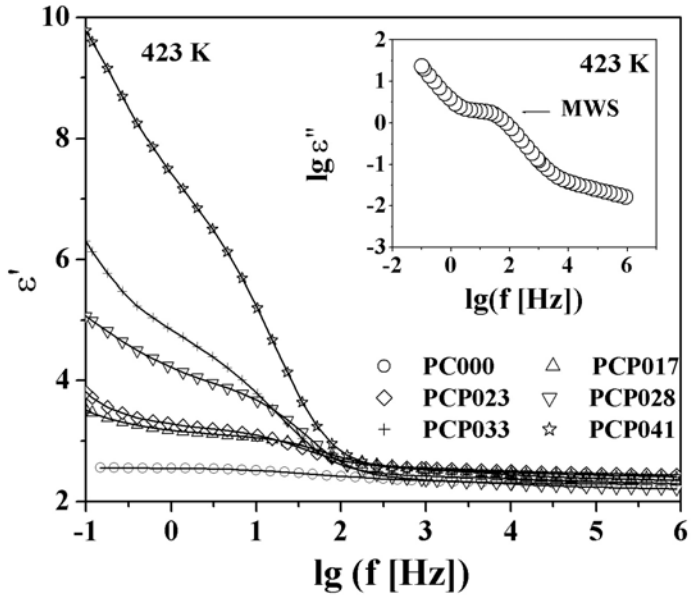

Fig. 5- 10 Dielectric storage ε´ of the pure PBAC sample (PC000) and PBAC-based PhenethylPOSS nanocomposites (PCP017 to PCP041) versus frequency at 423K. The lines are drawn to guide the eyes. The inset of the figure shows the frequency dependence of dielectric loss ε´´ of the sample PCP041 at the same temperature.

It needs to be noted that the MWS polarization is observed below the glass transition temperature of the PBAC-rich matrix. As discussed in section 2.3.4, the blocking of charge carriers at interfaces between two phases with different permittivity or conductivity induces MWS polarization. From this point of view, the characteristic temperature of the MWS polarization should be higher than the glass transition temperature of the composite.[88-90] However, it is not in contrast to the classic theories. The glass transition temperature of the PhenethylPOSS-rich domains ($T_{g,POSS\text{-}rich}$) is assumed to be lower than that of the PBAC-rich phase. In such a particular morphology, the charge carriers have a high mobility inside the POSS-rich domains even when the PBAC-rich domains are still in glassy state. As a result of this structure, the movement of charge carriers is blocked at the interface between POSS-rich phase and PBAC-rich phase.

Although the MWS polarization is not a relaxation process, it can be analyzed by fitting the HN-function to the data (Fig. 5- 10). In Fig. 5- 11 the relaxation rates of the MWS process ($f_{p,MWS}$) are plotted versus the reciprocal temperature. At a fixed temperature the $f_{p,MWS}$ decreases with the concentration of POSS. This result reflects the growing of the POSS-rich domains. Therefore,

the charge carriers need longer time to drift through the POSS-rich phases. An oversimplified model is developed to characterize such a polarization behavior.

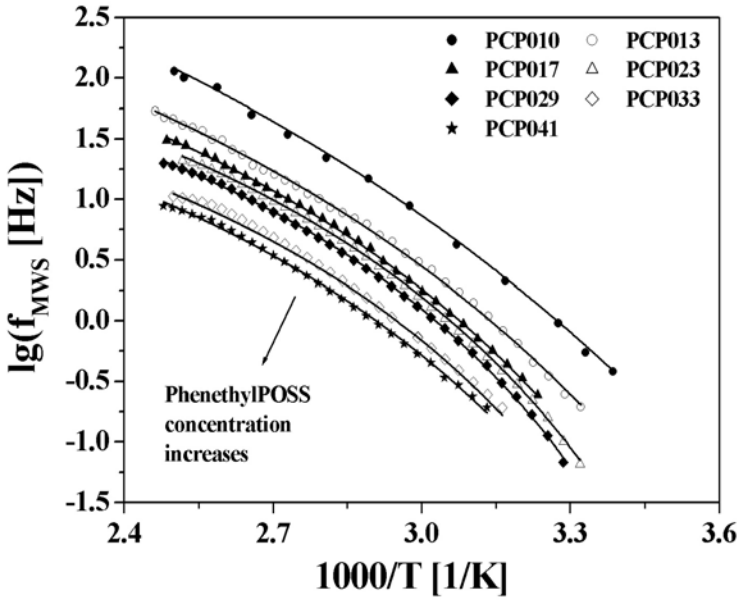

Fig. 5- 11 Relaxation rate of Maxwell-Wagner-Sillars polarization f_{MWS} versus the reciprocal temperature. Lines are drawn to guide the eyes.

According to this assumption, the POSS-rich domain is described by a mobile layer of the thickness *d* between interfaces of the separated phases (shown in Fig. 5- 7). From this point of view, *d* can be used to characterize the size of the spherical POSS-rich domains. The blocking of the charge carriers at the interfaces of the separated domains is described by an electrical double layer with an effective spacing characterized by its Debye length L_D. This double layer represents an additional capacitance in the system. Therefore the time dependence of the polarization is due to the charging/discharging of that electrical double layer. Assuming $d >> L_D$ the characteristic time τ_{MWS} can be estimated by the following function.[24,25,88]

$$\tau_{MWS} = \frac{\varepsilon_0 \varepsilon_S}{\sigma_0} \frac{d}{2L_D} \qquad \textbf{Eq. 5- 2}$$

Assuming ε_S, σ_0 and L_D are independent on the overall POSS concentration, the expansion of the mean size of the POSS-rich domains [*d/d(PCP010)*] can be estimated by Eq. 5- 3 from the data provided in Fig. 5- 11.

$$\frac{\tau_{MWS}}{\tau_{MWS,PCP010}} = \frac{f_{MWS,PCP010}}{f_{MWS}} \approx \frac{d}{d_{PCP010}} \qquad \text{Eq. 5- 3}$$

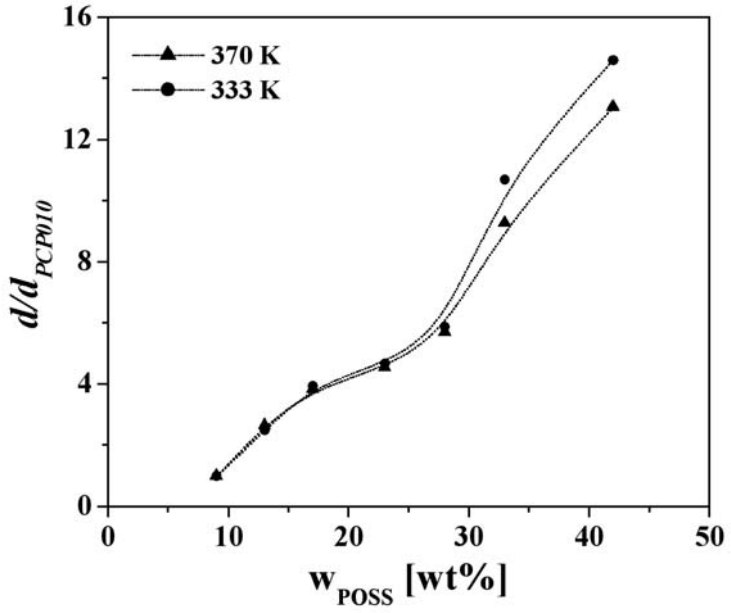

Fig. 5- 12 Change of the size of PhenethylPOSS-rich domain versus POSS concentration. Lines are drawn to guide the eyes.

In Fig. 5- 12 the relative change of the mean size of the POSS-rich domain d/d_{PCP010} is plotted versus the concentration of PhenethylPOSS for two different temperatures (333 K and 373 K). Eq. 5- 3 describes the growing of POSS-rich domains with w_{POSS}. As discussed in the above-mentioned model, there is no temperature dependence since the PBAC-rich phase is still in the glassy state and the phase behavior does not change with the temperature.

For medium concentrations (15 wt%~25 wt%), this change is quite moderate (Fig. 5- 12). This can also be discussed in the following picture. For low and medium concentration samples (w_{POSS} < 25 wt%), as the content of PhenethylPOSS rises, the number of POSS-rich domains increases faster compared to the growing of the domain size. This corresponds to the plateau-like changes in the concentration range between 15 wt% and 25 wt% in Fig. 5- 12. Above this concentration, the average size of the domains increases strongly. For the sample with highest concentration (41.2 wt%), the average domain size is about 13 times larger than that of PCP010.

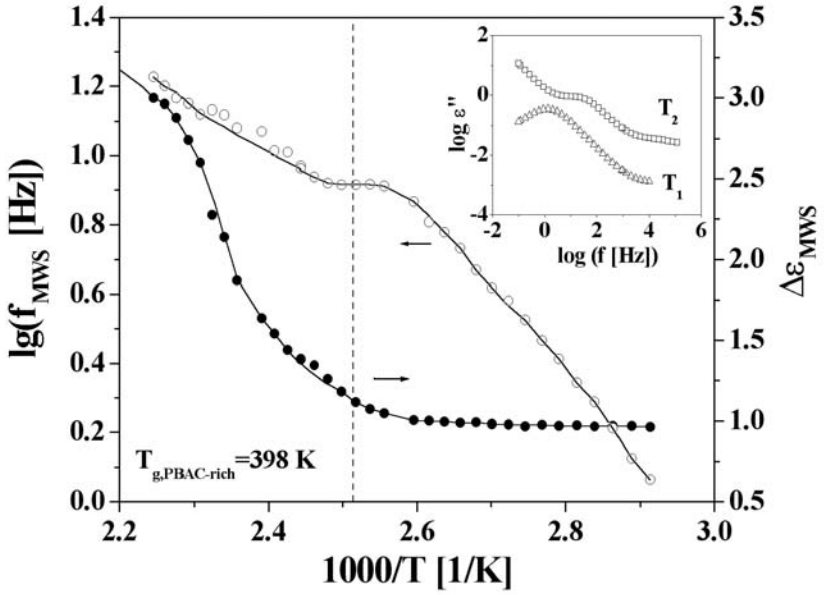

Fig. 5- 13 Relaxation rate f_{MWS} and relaxation strength $\Delta\varepsilon_{MWS}$ of the MWS process versus reciprocal temperature (PCP033). Lines are drawn to guide the eyes. The inset of the picture shows the dielectric loss of the same sample versus frequency at a temperature below and above the glass transition temperature of the PBAC-rich phase (T_1=343 K and T_2=433 K).

The simple discussed above assumes that the PBAC-rich phase is in the glassy state. Above the glass transition temperature of the PBAC-rich phase ($T_{g,PBAC\text{-}rich}$), the enhanced mobility of PBAC chains induces much stronger mobility. The inset of Fig. 5- 13 compares the significant differences on the MWS spectra of the sample PCP033 for temperatures below (T_1=343 K) and above (T_2=433 K) $T_{g,PBAC\text{-}rich}$. Fig. 5- 13 shows the relaxation rate (f_{MWS}) and the dielectric strength ($\Delta\varepsilon_{MWS}$) of the MWS polarization for the sample. Both quantities undergo drastic changes in the presented temperature region.

5.1.1.2 PS-based PhenethylPOSS Nanocomposites

Fig. 5- 14 shows the dependence of the dielectric loss of PS-based PhenethylPOSS on temperature and frequency. In the observed temperature and frequency range, only a single broad α-relaxation process with relatively low relaxation intensity can be identified. This process is assigned to the cooperative segmental motion of the polystyrene matrix (section 4.2.2).

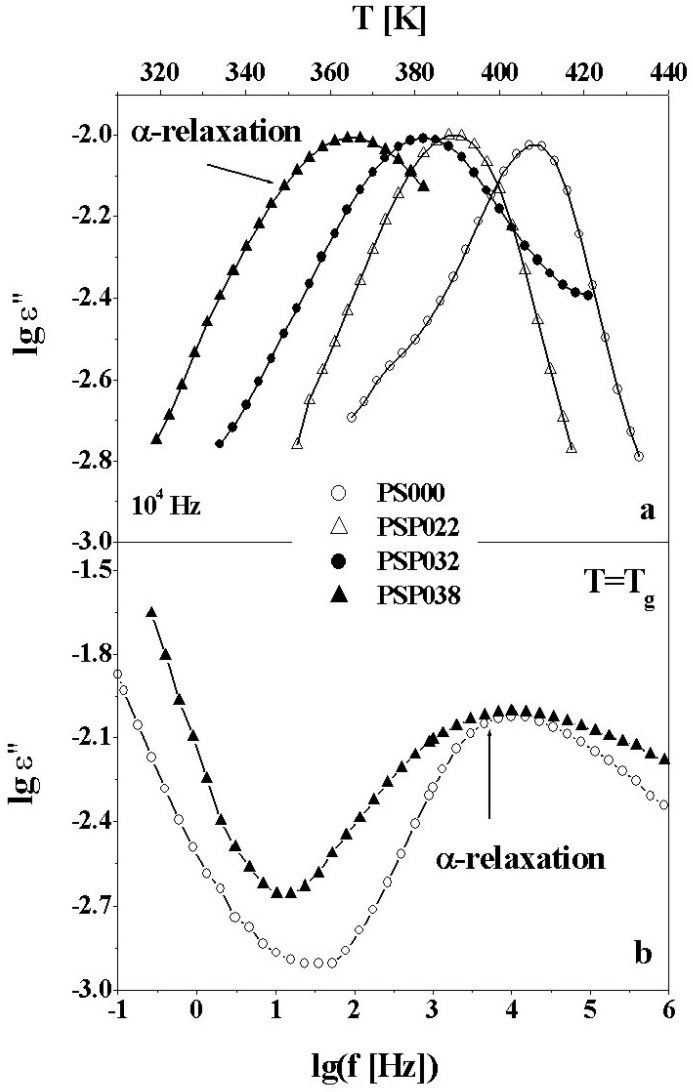

Fig. 5- 14 a: Dielectric loss of the pure PS (PS000) and PS-based PhenethylPOSS nanocomposites (PSP022 to PSP038) versus temperature. b: Dielectric loss of the pure PS (PS000) and the PS-based nanocomposite (PSP038) versus frequency at T_g.

In contrast to the PBAC-based nanocomposites discussed in the previous section, adding PhenethylPOSS molecules into PS matrix does not introduce new relaxation processes, but shifts the dynamic glass transition temperature of the nanocomposites to lower temperatures. As shown in Fig. 5- 14a, the

dynamic glass transition temperature of the PS-based nanocomposite PSP038 is about 60 K lower than that of pure PS (PS000). This effect can be attributed to the plasticization of the PhenethylPOSS molecules in pure PS phase.

Fig. 5- 14b shows the dielectric loss versus frequency for pure PS (PS000) and the PS-based PhenethylPOSS nanocomposites (PSP038) at the dynamic glass transition temperatures. The most significant change on the frequency-dependent domain is the broadening of the α-peak with the content of POSS.

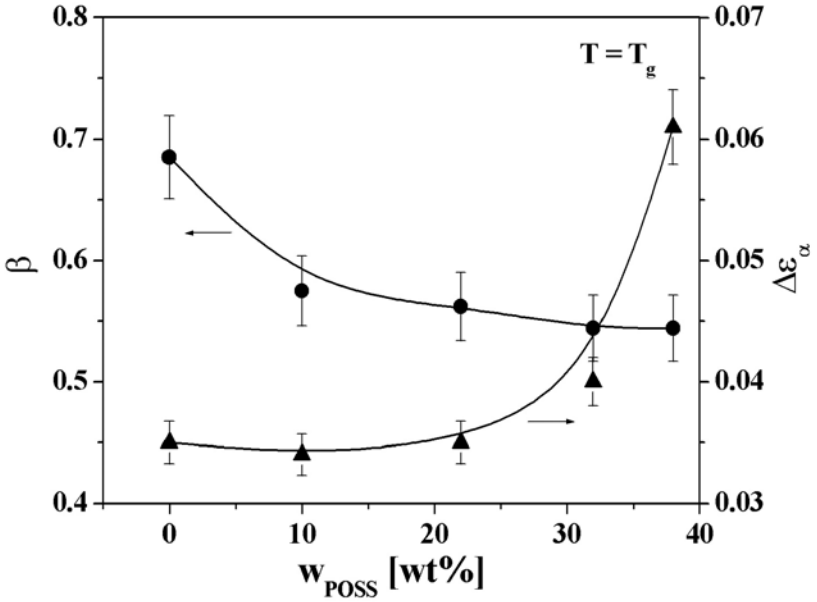

Fig. 5- 15 β (solid circles) and $\Delta\varepsilon_\alpha$ (solid triangles) versus PhenethylPOSS concentration. The relaxation parameters of the samples are taken at the temperature T = T_g. Lines are drawn to guide the eyes.

In the frequency domain, the dielectric loss curve is analyzed by fitting the HN function (Eq. 2- 33) to the data. The γ value is fixed as 1 since the peak of the α-relaxation process is assumed to be symmetric. The evaluated α-relaxation intensity $\Delta\varepsilon_\alpha$ and the symmetric broadening parameter β are plotted versus concentration in Fig. 5- 15. Due to the strong dependence of the glass transition temperature with POSS concentration, the relaxation parameters presented in Fig. 5- 15 are taken at the glass transition temperature $T=T_g$.

The calculated $\Delta\varepsilon_\alpha$ values increase with the POSS content. According to the Kirkwood-Fröhlich correlation (Eq. 2- 14), this is because the dipole moment of PhenethylPOSS is greater than that of the polystyrene. Thus blending POSS

into polystyrene will increase the effective dipole moment of the system. Therefore, the relaxation intensity $\Delta\varepsilon$ increases with the concentration of POSS. The symmetric broadening parameter β decreases with the POSS concentration. It implies the broadening of the α-relaxation peak with POSS concentration. This line of argument corresponds to the observation from Fig. 5- 14a and b. The broadening of the relaxation spectra indicates an enhanced heterogeneity of the molecular motions.

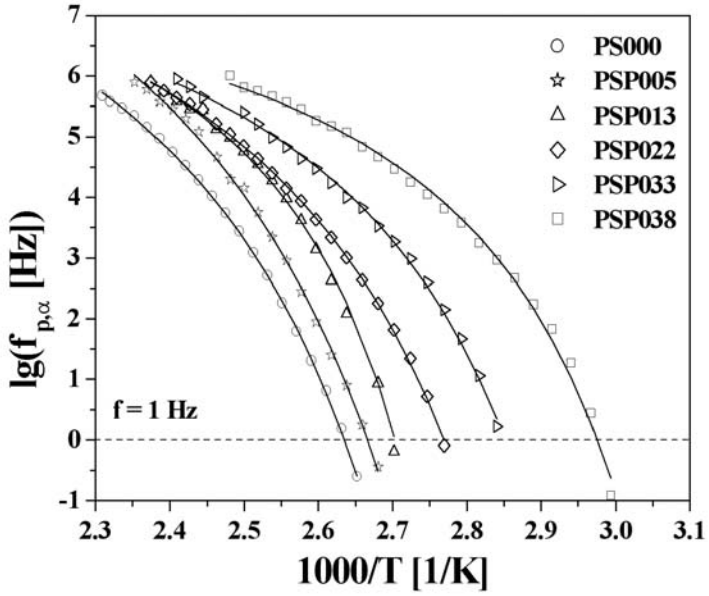

Fig. 5- 16 Relaxation rate versus reciprocal temperature of the pure PS (PS000) and PS-based PhenethylPOSS nanocomposites (PSP005 to PSP038). The data are fitted by the VFTH function and the respective parameters are listed in Tab. 5- 2.

Tab. 5- 2 The VFTH fitting parameters of Fig. 5- 16

Sample Code	α-relaxation		
	$\log(f_\infty$ [Hz])	A [K]	T_0^{id} [K]
PhenethylPOSS	11.4	334	218.2
PS000	10.6	475.3	334.4
PSP005	11.8	565.3	327.1
PSP013	9.0	242.3	323.7
PSP022	10.0	412.7	319.7
PSP033	11.3	506.1	309.5
PSP038	8.4	238.7	307.5

The relaxation rates $f_{p,\alpha}$ of the nanocomposites were calculated by fitting the HN function to the data and plotted in Fig. 5- 16 versus the reciprocal

temperature. The data are then fitted with the VFTH function. The fitting results are listed in Tab. 5- 2. Comparing to Fig. 5- 3 and Fig. 5- 16, the VFTH fitting curve in Fig. 5- 16 shows a considerable shift with PhenethylPOSS concentration. Following the method suggested in Fig. 2- 5, the dynamic glass transition temperatures of the samples (T_g^{Diel}) can be estimated from the VFTH fitting curves at a relaxation rate of 1 Hz.

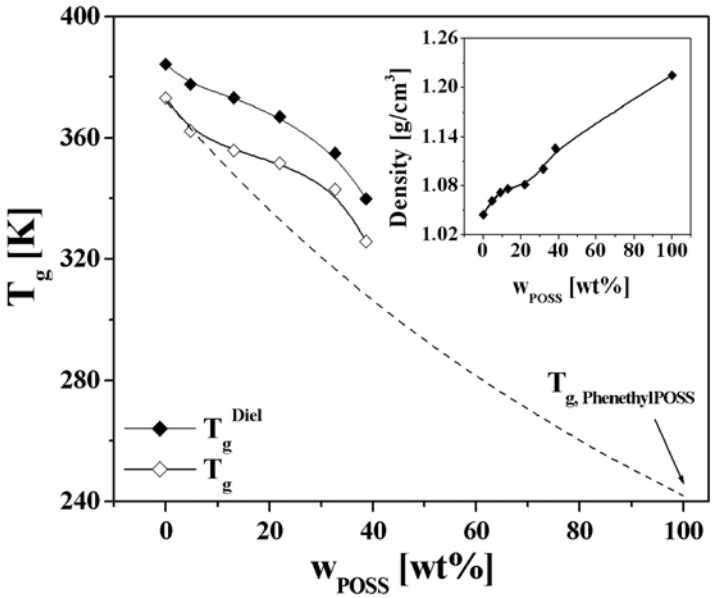

Fig. 5- 17 Glass transition temperature (T_g) and dynamic glass transition temperature (T_g^{Diel}) of PS-based nanocomposites versus PhenethylPOSS concentration w_{POSS}. The dashed line shows the prediction given by the Fox function. The inset of the figure shows the change of density of the sample versus PhenethylPOSS concentration.

The dynamic glass transition temperature (T_g^{Diel}) of the PS-based PhenethylPOSS nanocomposites is plotted over the weight fraction of POSS in Fig. 5- 17. In addition, the Fox expectation (Eq. 5- 1) is given in the same plot. Similar to Fig. 5- 8, the value of T_g^{Diel} is about 20 K higher than that of T_g measured in DSC experiments. This is because the characteristic frequency of DSC measurements is lower than that of the dielectric measurements.

Both the T_g and T_g^{Diel} of PSP nanocomposites decrease strongly with POSS concentration. In contrast to Fig. 5- 8, the T_g of PSP nanocomposites decrease continuously with the POSS concentration. The experimental values do not deviate as much from the prediction given by the Fox function than do those of the of the PBAC-based nanocomposites.

Such a behavior implies an improved solution compatibility of the POSS molecules in PS compared to PBAC due to the interaction between the phenyl rings of PS and the phenethyl side groups of POSS. Taking into consideration that in PS the phenyl ring forms a side group of the polymer backbone, while for PBAC, phenyl rings part of the backbone chain. PS-based nanocomposites are more likely to form dense packing structures around POSS molecules than PBAC-based nanocomposites, which is in agreement with the density measurements. As shown in the inset of the Fig. 5- 17, the density of the samples increases continuously with the content of POSS. This implies that the local fraction of the free volume does not change due to packing incapability of PBAC. Thus the PhenethylPOSS molecules have higher solution compatibility in the PS matrix than in the PBAC matrix.

5.1.2 Nanocomposites based on ChloropropylPOSS

Fig. 5- 18 presents the temperature and frequency-dependent relaxation process of the pure PBAC and a PBAC-based nanocomposite (PCC033). Similar to the relaxation spectrum of pure PBAC, the α- and β-processes can be observed also in the temperature domain. Compared to the α-relaxation process of the pure PBAC, the α-peak of PCC033 becomes broader (Fig. 5- 18a). Further investigation in the frequency domain (Fig. 5- 18b) shows this effect is due to the enhanced conductivity of the sample. This issue will be discussed in more detail in a later part of this section.

The α-relaxation was analyzed by fitting the HN function to the dielectric spectra (Fig. 5- 19). The obtained relaxation rate of the α-relaxation was then plotted versus reciprocal temperature. The data were fitted by the VFTH function. The fitting parameters of the VFTH function are given in Tab. 5- 3. The fitting results of PBAC-based ChloropropylPOSS nanocomposites show that the dynamic glass transition temperature of the nanocomposites shifts to lower temperatures compared to that of the pure PBAC. This means that there is a certain low miscibility of ChloropropylPOSS within PBAC. For all concentration of POSS, the fits of the VFTH function collapse into one curve and therefore their T_g^{Diel} values are identical. From these results, one has to

conclude that the miscibility of Chloropropyl-POSS in PBAC is low. Even for lower concentrations of POSS, the phase separation should be observed.

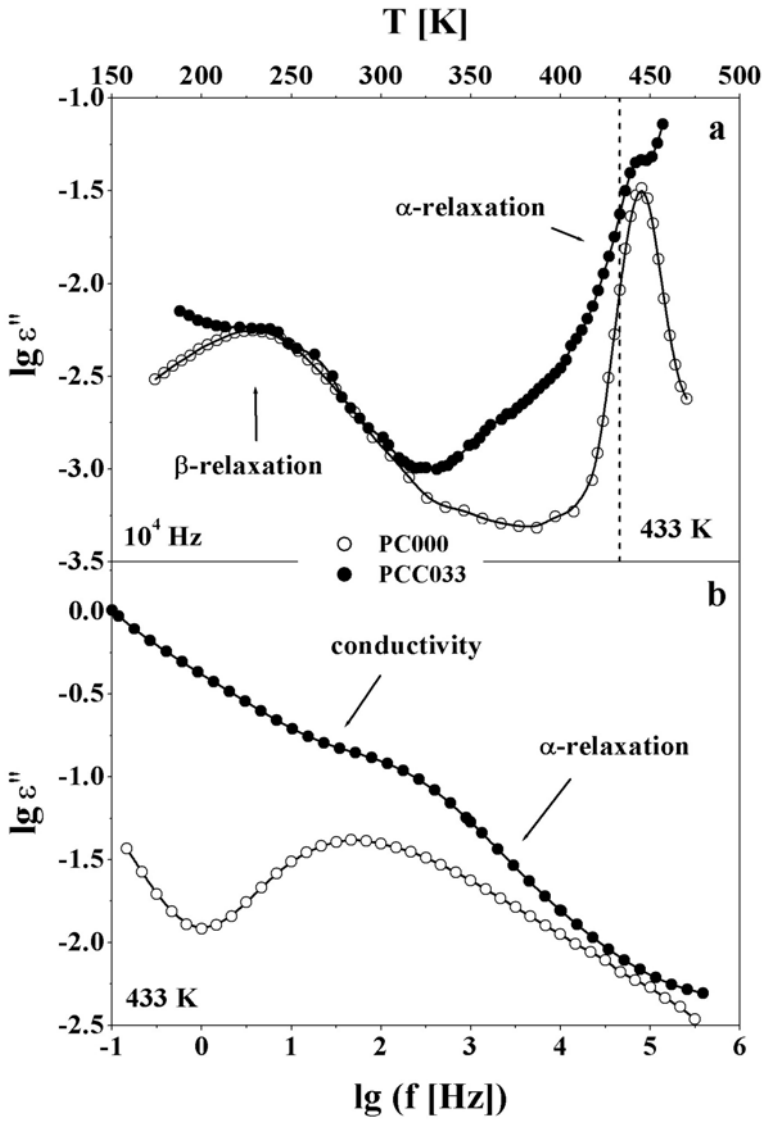

Fig. 5- 18 a: Dielectric loss of the pure PBAC (PC000) and a PBAC-based Chloropropyl-POSS nanocomposite (PCC033) versus temperature at 10^4 Hz. Lines are drawn to guide the eyes. b: Dielectric loss of the pure PBAC (PC000) and a PBAC-based Chloropropyl-POSS nanocomposite (PCC033) versus frequency at 433 K. Lines are drawn to guide the eyes.

DSC measurements were carried out to investigate the micromorphology of the nanocomposites. As shown in the Fig. 5- 20, three endothermic peaks at around 250 K, 400 K and 480 K are identified from the DSC thermogram of pure ChloropropylPOSS indicating a complex melting behavior of crystallized POSS domains.

Adding ChloropropylPOSS into PBAC only results in limited changes on the glass transition temperature. Instead, a new endothermic peak at around 480

K with increasing intensity can be observed. The peak corresponds to the melting temperature of the crystalline domains of POSS inside the nano-composites. The melting enthalpy of the nanocomposites H_m increases linearly with the content of ChloropropylPOSS (shown as the inset of the Fig. 5- 20).

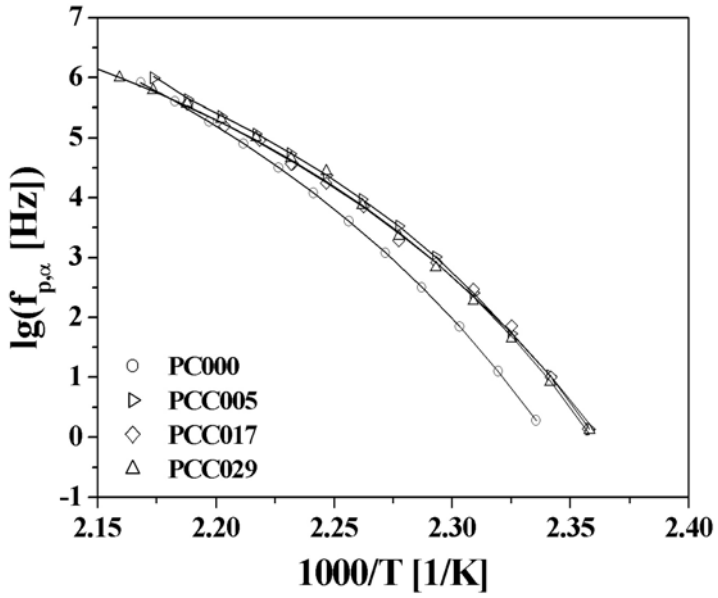

Fig. 5- 19 Relaxation rate versus reciprocal temperature of the pure PBAC (PC000) and PBAC-based ChloropropylPOSS nanocomposites (PCC005 to PCC029). The data are fitted by VFTH function. The fitting results are listed in Tab. 5- 3.

Tab. 5- 3 The VFTH fitting result of Fig. 5- 19

Sample Code	α-Relaxation		
	lg(f_∞ [Hz])	A [K]	T_0^{id} [K]
PC000	13.7	611.3	382.6
PCC005	11.7	419.2	384.8
PCC013	11.6	418.6	384.6
PCC017	11.5	418.5	384.5
PCC023	11.5	418.5	384.5
PCC029	11.6	418.8	384.6
PCC033	11.7	418.2	384.4

This assumption corresponds to the observation of dielectric measurements since the crystallized phases have sequenced structures; therefore the modification on the segmental mobility of the PBAC matrix is rather low. From this point of view, blending ChloropropylPOSS may not impact the shape and location of the dielectric spectra significantly. On the other hand, as discussed in the previous section, the pure ChloropropylPOSS is conductive at

higher temperatures (Fig. 4- 6). Thus it can be presumed that these separate ChloropropylPOSS phases enhance the conductivity of the nanocomposite. This argument is in agreement with the result in Fig. 5- 18b.

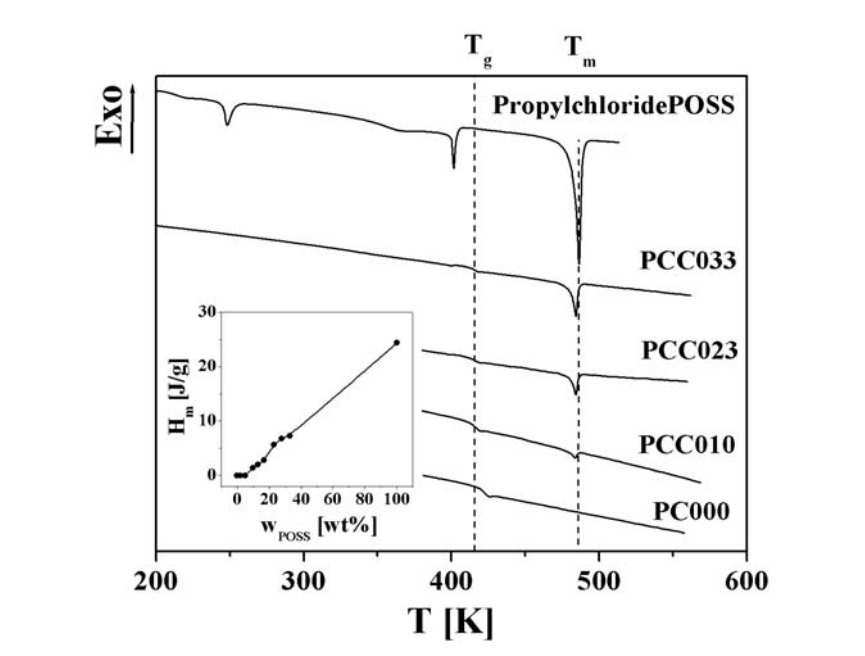

Fig. 5- 20 DSC thermograms of pure PBAC, the PBAC-based ChloropropylPOSS nanocomposites (PCC010 to PCC033) and the pure ChloropropylPOSS. The inset of the picture shows the relation between the melting enthalpy of the nanocomposites and POSS concentration.

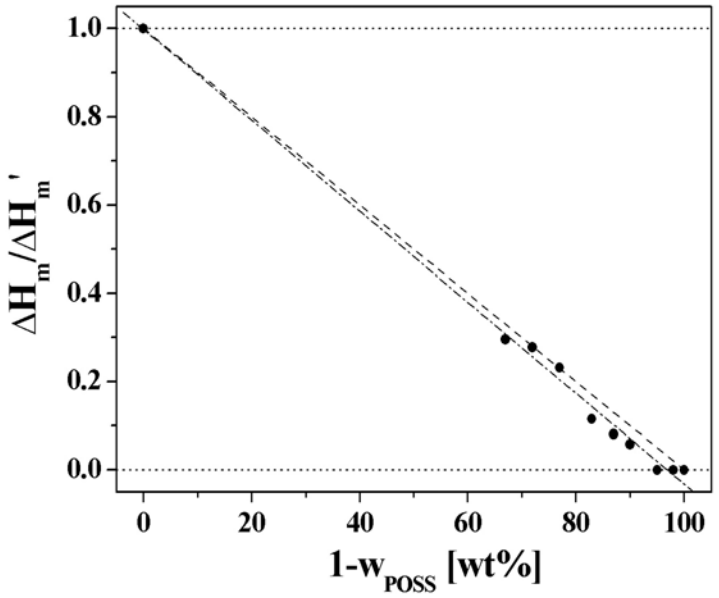

Fig. 5- 21 The normalized melting enthalpy (solid cycles) versus the concentration of ChloropropylPOSS. The dash-dotted line is the linear fitting of the normalized values. The dashed line represents the change of melting enthalpy of immiscible crystalline domains in the polymer phase.

The melting enthalpy of the nanocomposites (H_m), which are presented in the inset of Fig. 5- 20, is normalized by the melting enthalpy of the ChloropropylPOSS at around 480 K (H_m'). The normalized values are plotted in Fig. 5- 21 versus the content of PBAC ($1-w_{POSS}$). The dash-dotted line is the linear fitting of these normalized values, while the dashed line in the plot represents the change of melting enthalpy of immiscible crystalline phases in polymer domains. As shown from the figure, the normalized melting enthalpy of the nanocomposites is slightly lower than the value given by the dashed line. This indicates that a certain amount of ChloropropylPOSS is dissolved in the PBAC phase. This assumption corresponds to the conclusion given from the dielectric analysis (Fig. 5- 19), in which a slight difference between the dynamic glass transition temperature of the nanocomposites and the pure PBAC can be observed.

5.1.3 Morphology of Nanocomposites

As shown in section 4.4, POSS molecules can be blended into matrix polymers to form transparent film-like samples. The samples were investigated by dielectric relaxation spectroscopy and show different relaxation behavior in depending both on the type of POSS and on the matrix polymers. Based on the results of the molecular mobility, phase diagrams are deduced to describe the changes of the micromorphology of the nanocomposites. Fig. 5- 22 shows the changes of T_g^{Diel} of the samples versus POSS concentration.

It needs to be noted that in Fig. 5- 22 the dynamic glass transition temperatures (T_g^{Diel}) of the sample were normalized by the dynamic glass transition temperature of pure polymer for comparison. The plot indicates that adding PhenethylPOSS molecules has strong influence on the molecular mobility of PBAC. That is due to the formation of a purely organic surface outside of the silica core by Phenethyl sidegroups. This unique structure improves the solution compatibility of the PhenethylPOSS particles.

In general, the PhenethylPOSS molecules can be blended into PBAC at a molecular level up to a certain concentration around 7 wt%. Above this concentration, the POSS molecules aggregate and form POSS-rich domains inside the PBAC-rich phase. Compared with the PBAC-based PhenethylPOSS

nanocomposites, adding PhenethylPOSS into PS shifts the dynamic glass transition temperature significantly. This is because the phenethyl sidegroups of POSS have stronger interactions with the phenyl sidegroups in PS than with the phenyl rings of PBAC. Therefore the polymer matrix forms a denser packing structure with PhenethylPOSS molecules. As a result, the solution compatibility of the PhenethylPOSS in PS is higher than in PBAC. Compared with the PBAC-based PhenethylPOSS nanocomposites, the dynamic glass transition temperature of the PS-based PhenethylPOSS nanocomposites shows less deviation from the prediction given by the Fox function.

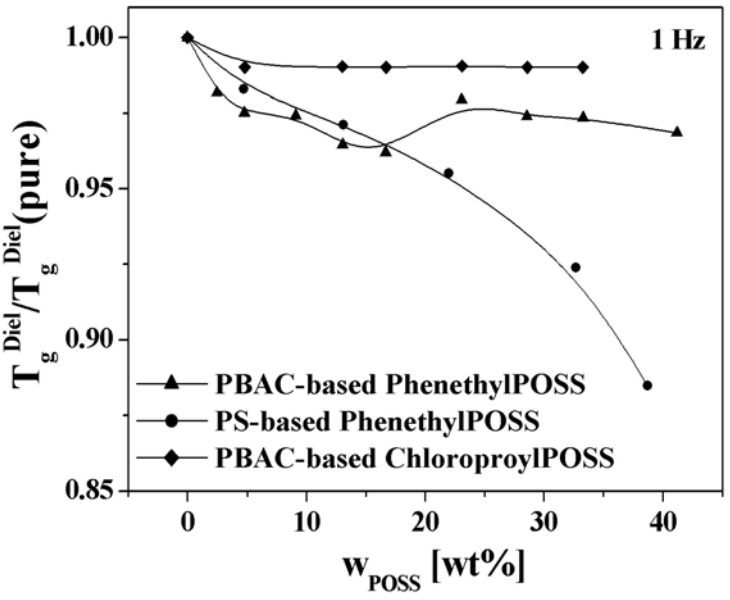

Fig. 5- 22 Normalized dynamic glass transition temperature of the POSS-based nanocomposite samples versus POSS concentration. Lines are drawn to guide the eyes. The abbrievation: PCP, PSP and PCC stand for PBAC-based PhenethylPOSS nanocomposites, PS-based PhenethylPOSS nanocomposites and PBAC-based ChloropropylPOSS nanocomposites, respectively.

Compared with PhenethylPOSS, mixing ChloropropylPOSS into PBAC has only limited influence on the dynamic glass transition temperature of PBAC because there is no specific interaction between the polymer segments and the subunits of ChloropropylPOSS. The DSC measurements have shown that blending ChloropropylPOSS molecules into PBAC enhances the crystallinity of the sample. The crystallized ChloropropylPOSS molecules form separated domains inside the PBAC matrix. Since these separated domains are conductive, the conductivity of the sample is substantially enhanced.

5.2 Gas Transport Properties of Nanocomposites

In the previous sections, the morphology and molecular mobility of polymer-based nanocomposites were investigated by dielectric relaxation spectroscopy. Such morphological changes also influence the gas transport properties of the system because the solubility of the gas molecules depends on the free volume of the polymers (see section 2.4). Moreover, as a dynamic quantity of the gas trans-port process, the diffusion coefficient depends strongly on the molecular mobility of the polymer segments.

Tab. 5- 4 σ_k and T_C of gases used for the experiments

	CO_2	O_2	N_2	CH_4
σ_k [10^{-10} m]	3.30	3.46	3.64	3.80
T_C [K]	304.2	154.4	126.2	190.7

Four gases (N_2, CH_4, O_2 and CO_2) provided by Messer-Griesheim GmbH were used in gas transport experiments as penetrants. The size and shape of the penetrant is characterized by the kinetic diameter of the gas molecules (σ_k), which is defined as the intermolecular distance of closest approaches for two molecules colliding with zero initial kinetic energy.[209] The kinetic diameter (σ_k) and critical temperatures (T_C)[98] of the penetrants are listed in Tab. 5- 4. As stated in section 4.4, the PS-based ChloropropylPOSS nanocomposites were too brittle to be investigated by the gas transport measurements. Therefore, the gas transport properties of the other three nanocomposites (Tab. 4- 2 and Tab. 4- 4) were investigated following the methods introduced in section 2.4.

5.2.1 Nanocomposites based on PhenethylPOSS

5.2.1.1 Gas Permeation of PBAC-based PhenethylPOSS Nanocomposites

The gas permeation measurements of the PBAC-based nanocomposites were carried out in a broad temperature and pressure range. The results are listed in Appendix 7.2.1.1. The obtained permeability values of the pure PBAC (PC000) are in agreement with the values reported in the literature.[140,210] The measured CO_2 permeability of the samples is plotted in Fig. 5- 23 versus upstream pressure p_1 and POSS concentration w_{POSS} in a 3-dimensional plot.

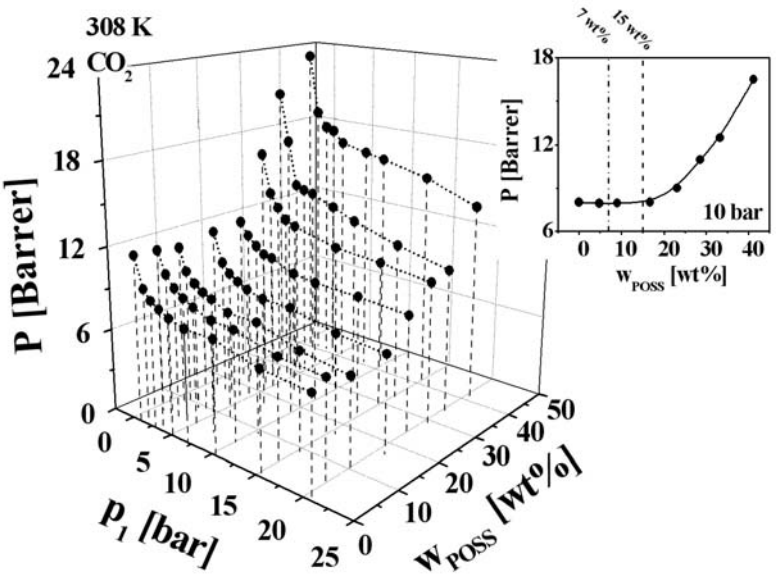

Fig. 5- 23 CO_2 permeability of the PBAC-based PhenethylPOSS nanocomposites versus upstream pressure (p_1) and concentration of POSS (w_{POSS}). The inset of the picture shows the permeability values at 10 bar versus w_{POSS}. Lines are drawn to guide the eyes.

For each sample, the permeability values decrease as the upstream pressure p_1 rises. This effect was commonly observed in gas permeation measurements of polymeric materials. Sanders attributed the reduction in permeability to the site-saturation mechanism.[211,212] The author assumed that gas molecules easily permeate through the polymer due to the existence appearance of microvoids in the polymer matrix. At higher concentrations of the penetrant, these microvoids are saturated; therefore the permeability of gas molecules decreases.

For 10 bar upstream pressure, the CO_2 permeability values of the nano-composite are plotted versus POSS concentration in the inset of Fig. 5- 23. The permeability values almost remain constant at lower concentrations and show a increase with the concentration of POSS at higher concentrations. The transition of the permeability is located around 15 wt% (shown as the dashed line in the inset of Fig. 5- 23), which is higher than the concentration of phase separation proposed by the dielectric measurements (see section 5.1.1.1, shown as the dot-dashed line in the inset of Fig. 5- 23).

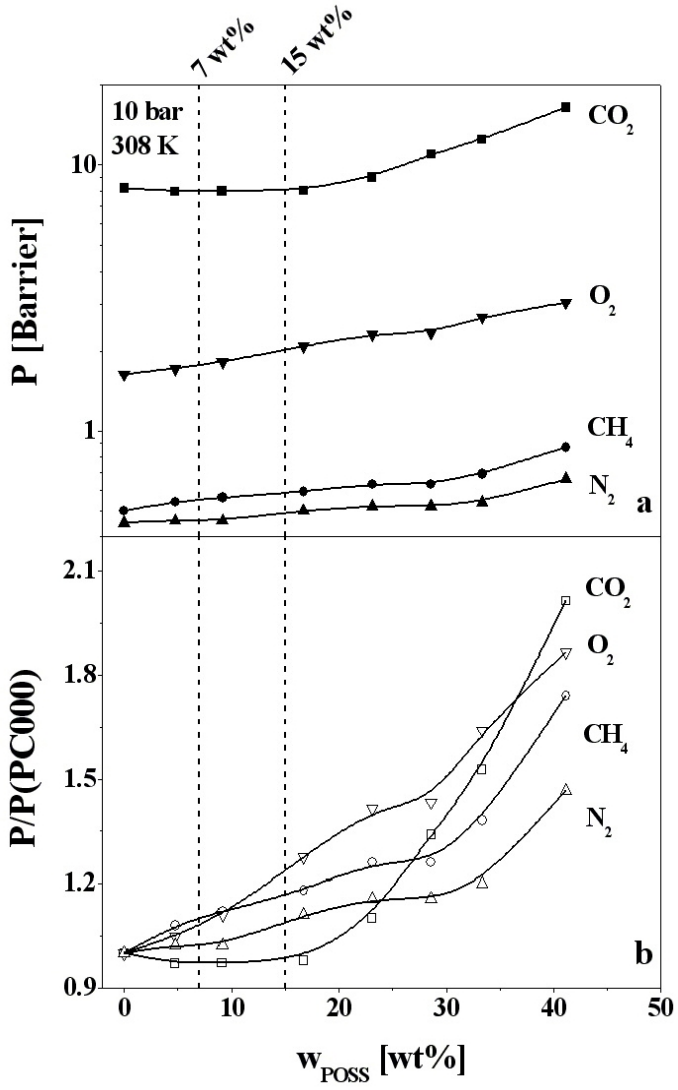

Fig. 5- 24 a: Permeability of all penetrants through PBAC-based PhenethylPOSS nanocomposites versus POSS concentration at 10 bar and 308 K. b: Relative permeability values of the gases versus POSS concentration under the same conditions. Lines are drawn to guide the eyes.

Fig. 5- 24a shows a plot of the measured permeability values for all investigated gas in PBAC-based PhenethylPOSS nanocomposites at 10 bar upstream pressure and 308 K. It can be observed that the permeability values of the samples increase with the following order of gases:

$$P(N_2)<P(CH_4)<P(O_2)<P(CO_2).$$

Further investigations are carried out by plotting the relative permeability values P/P(PC000) at 10 bar and 308 K versus w_{POSS} (Fig. 5- 24b). As shown in Fig. 5- 24b, permeability of the gases is increasing with POSS concentration. For CO_2, CH_4 and N_2, a certain transition point of the change of permeability can be observed above 15 wt%. Above this transition point, the permeability

values of the penetrants are significantly enhanced. This indicates that the phase separated POSS-rich domains have additional effects on the gas transport properties of the nanocomposite.

Tab. 5- 5 α(CO_2/CH_4) of PBAC-based PhenethylPOSS nanocomposites at 10 bar

Sample	w_{POSS} [wt%]	α(CO_2/CH_4)			
		308 K	318 K	328 K	338 K
PC000	0	16.0	13.7	11.7	10.1
PCP005	5	15.0	13.6	12.3	11.3
PCP010	10	14.5	13.0	11.8	10.7
PCP017	17	13.6	11.5	10.0	8.7
PCP023	23	14.3	12.2	10.5	9.2
PCP029	29	17.4	17.5	17.5	17.6
PCP033	33	18.2	15.5	13.3	11.5
PCP041	41	19.0	15.8	13.4	11.5

Tab. 5- 6 α(O_2/N_2) of PBAC-based PhenethylPOSS nanocomposites at 10 bar

Sample	w_{POSS} [wt%]	α(O_2/N_2)			
		308 K	318 K	328 K	338 K
PC000	0	3.6	3.5	3.4	3.3
PCP005	5	3.7	3.8	3.8	3.8
PCP010	10	3.9	3.9	3.9	3.9
PCP017	17	4.4	4.2	4.0	3.9
PCP023	23	4.5	4.3	4.2	4.1
PCP029	29	4.9	4.9	4.9	4.8
PCP033	33	4.3	4.2	4.1	4.0
PCP041	41	4.0	3.9	3.8	3.7

An important parameter to characterize gas separation process of a given membrane is the perm-selectivity α(A/B). α(A/B) of an isotropic film is defined as the ratio of the permeabilities of the gas A and B (Eq. 5- 4).

$$\alpha(A/B) = \frac{P_A}{P_B}, \quad P_A \geq P_B \qquad \textbf{Eq. 5- 4}$$

The perm-selectivities of the CO_2/CH_4 and O_2/N_2 systems have attracted considerable attentions due to their great industrial importance. Based on the permeability values presented in the Appendix 7.2.1, the perm-selectivities of

CO_2/CH_4 and O_2/N_2 of the gases at 10 bar feed pressure are calculated and listed in Tab. 5- 5 and Tab. 5- 6.

For each sample, the investigated perm-selectivity of the gases decreases as the temperature decreases. This is because the higher temperature enhances the segmental mobility of the polymer matrix. The $\alpha(CO_2/CH_4)$ initially decreases with increasing content of PhenethylPOSS but increases with the concentration of POSS at higher concentrations. That is due to the influence of the Phenethyl-POSS-rich domains in the nanocomposites. Comparing the sample PCP041 with PC000, the $\alpha(CO_2/CH_4)$ at this higher POSS concentration is about 10 % higher than that of the pure PBAC sample.

The $\alpha(O_2/N_2)$ increases with the concentration of POSS molecules in the lower concentration range up to 29 wt%. That is due to the fact that the relative permeability of O_2 increases linearly even in the lower concentration range (shown in Fig. 5- 24a and b). In the higher concentration range (above 33 wt%), the perm-selectivity values show smaller dependency on the concentration of POSS.

In order to understand such particular changes on the permeability values, the diffusivity and solubility values were evaluated at 10 bar upstream pressure for comparison. Fig. 5- 25a shows the dependency of the diffusion coefficients on the concentration of POSS. Here, the O_2 molecules move faster than the other gas molecules due to its smaller size. In contrast to the permeability values, the diffusion coefficients of the gas molecules increase in the following order:

$$D(CH_4)<D(N_2)<D(CO_2)<D(O_2).$$

For all the penetrants, the diffusion coefficients increase with the content of POSS molecules monotonously. Such a behavior can be explained in terms of morphology changes of the PBAC-based PhenethylPOSS nanocomposites. The dielectric investigations prove that adding Phenethyl-POSS molecules leads to a phase separation of POSS-rich domains. The higher segmental mobility inside POSS-rich domains favors a faster diffusion process of the gas molecules. As a result, the overall diffusion coefficient of the gas molecules is enhanced.

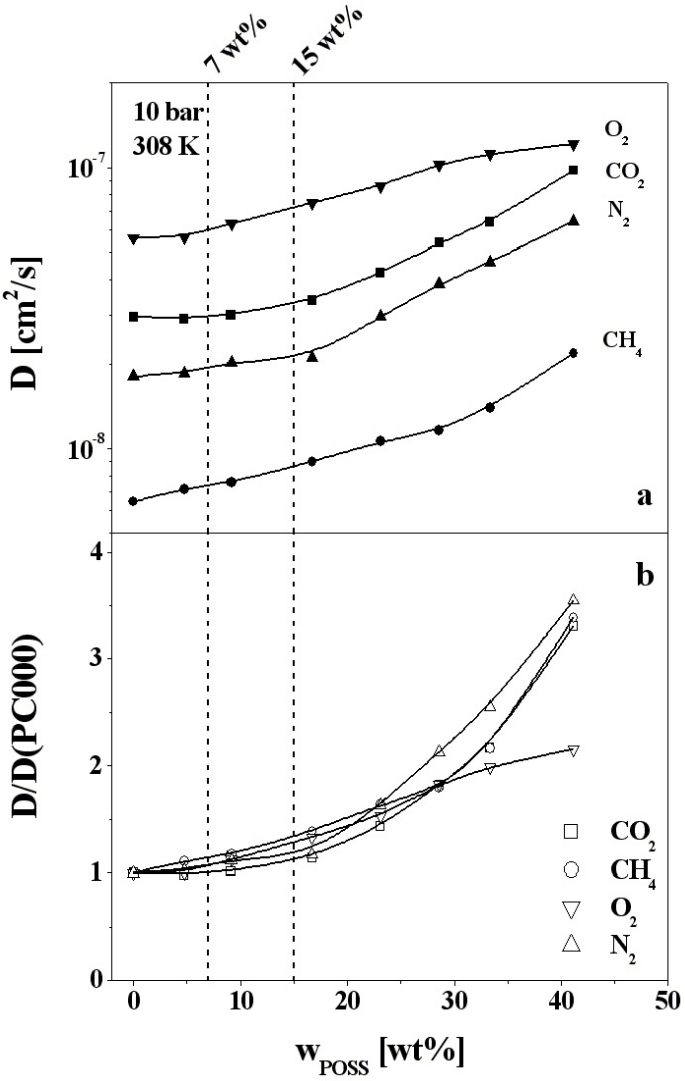

Fig. 5- 25 a: Diffusion coefficients of all penetrants through PBAC-based PhenethylPOSS nanocomposites versus POSS concentration at 10 bar feed pressure and 308 K. b: Relative diffusion coefficients of the gases versus POSS concentration under the same conditions. Lines are drawn to guide the eyes.

The relative diffusion coefficients of the gas molecules D/D(PC000) are plotted versus POSS concentration in Fig. 5- 25b. Similar to Fig. 5- 24b, the plot shows that the increase of the diffusion coefficient of CO_2, CH_4 and N_2 is significantly enhanced above 15 wt%. This result tends to support the argument that the increase of permeability for higher POSS concentrations is due to the increase of the diffusion coefficient of the gas molecules in the POSS-rich domains. The solubility values can be estimated as the ratio of permeability and diffusion coefficient (Eq. 2- 42, results are presented in Appendix 7.1). For the highly sorbing gases, CO_2 and CH_4, the calculated solubility values are about 5 to 10 times higher than those of the other penetrants.

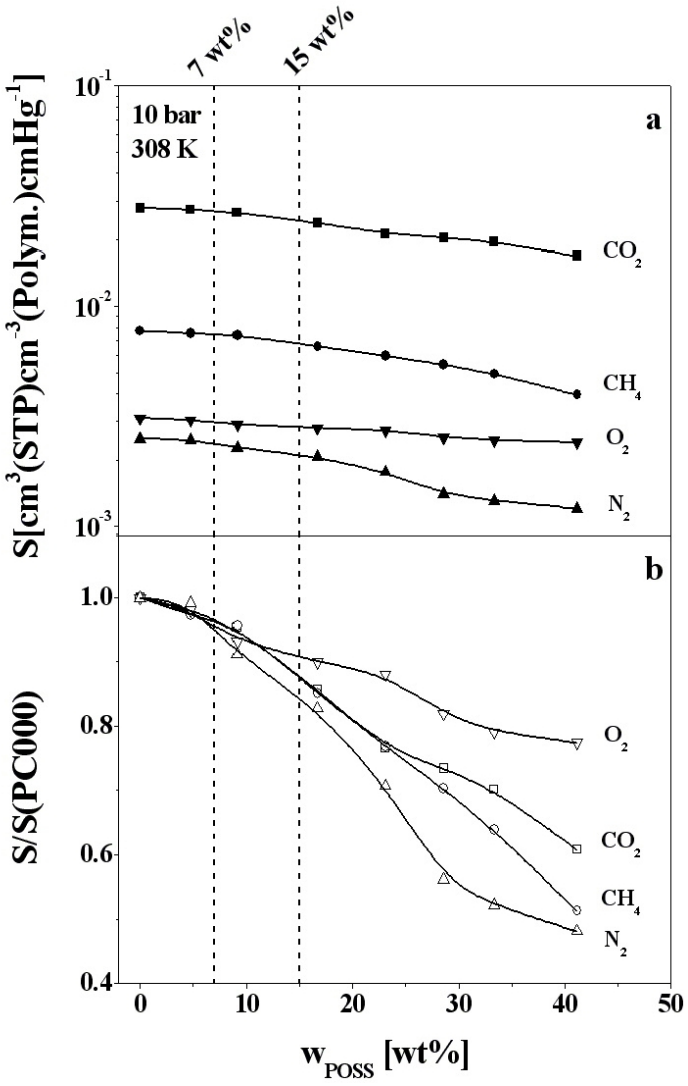

Fig. 5- 26 a: Solubility of all penetrants through PBAC-based PhenethylPOSS nanocomposites versus POSS concentration at 10 bar feed pressure and 308 K. b: Relative solubility values of the gases versus POSS concentration under the same conditions. Lines are drawn to guide the eyes.

The solubility values as well as the relative solubility values S/S(PC000) are plotted versus POSS concentration in Fig. 5- 26a and b, respectively. These plots show that the solubility of the gases decreases with the PhenethylPOSS concentration. Moreover, it needs to be pointed out that the reduction of the solubility is much more significant above 15 wt%. It is concluded that for the PBAC-based PhenethylPOSS nanocomposites, the solubility of the gas decreases as the concentration of PhenethylPOSS is increasing. With the respect to permeability, this effect is overcompensated by the increased diffusion coefficients in POSS-rich domains. As a result, the permeability of the gas increases at higher POSS concentrations.

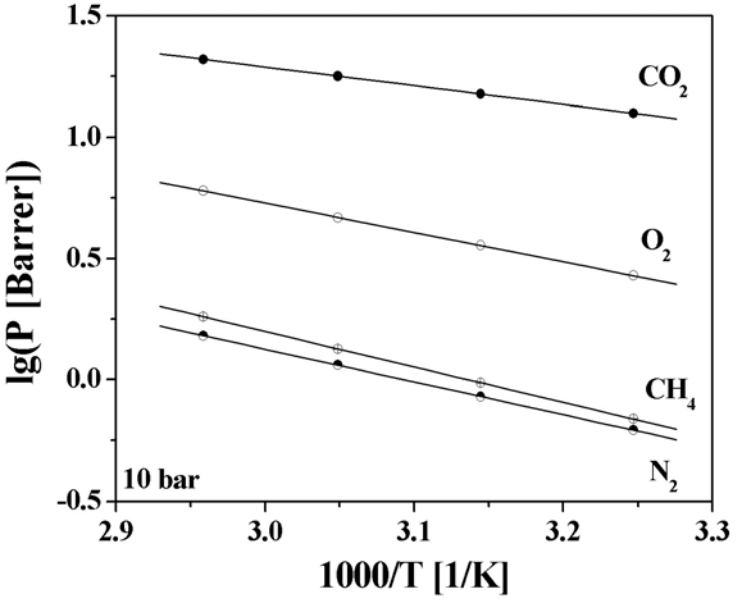

Fig. 5- 27 Permeability versus reciprocal temperature at 10 bar feed pressure. The data are taken from the temperature dependent permeation measurements of the sample PCP033 and fitted by Eq. 2- 57 (the solid lines).

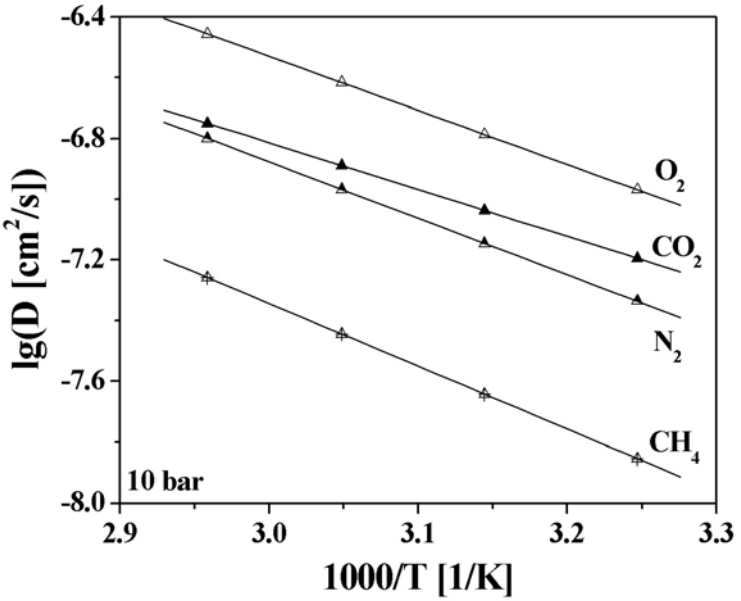

Fig. 5- 28 Diffusion coefficients versus reciprocal temperature at 10 bar feed pressure. The data are taken from the temperature dependent permeation measurements of the sample PCP033 and fitted by Eq. 2- 58 (the solid lines).

In the discussions presented above, the changes of the gas transport parameters with POSS concentration were investigated in the concentration and pressure dependent domains. In addition, the modification on the gas transport properties can also be studied in the temperature dependent domain. The

temperature-dependent permeation measurements were carried out at 10 bar feed pressure at 4 different temperatures (308 K, 318 K, 328 K and 338 K). The obtained permeabilities and diffusion coefficients are listed in Appendix 7.2.1.2. For each specific sample, the gas transport parameters were fitted by an Arrhenius function. Fig. 5- 27 and Fig. 5- 28 show examples of such exponential dependences on reciprocal temperature in Arrhenius plots (see section 2.4.4).

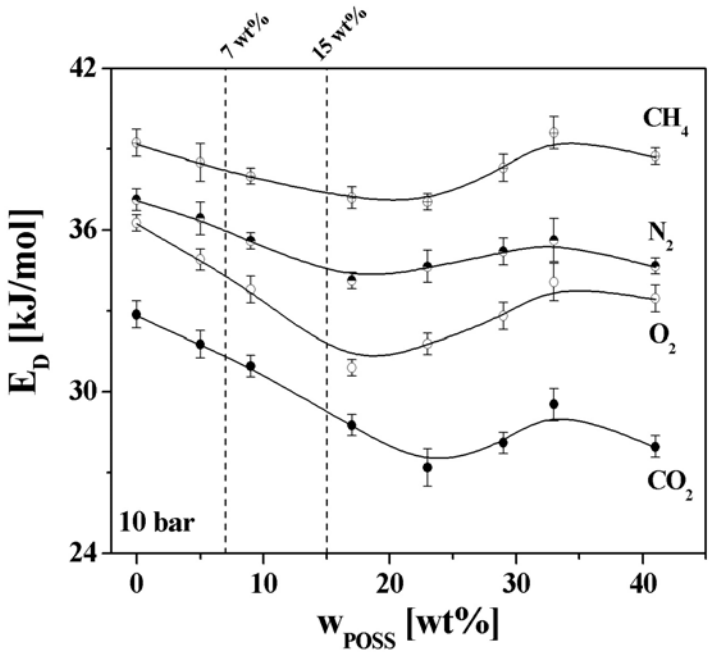

Fig. 5- 29 Activation energy of diffusion versus PhenethylPOSS concentration. Lines are drawn to guide the eyes. The dashed lines represent the content 7 wt% and 15 wt%.

The activation energies of permeation and diffusion (E_p and E_D) were determined from the fitting parameters (Eq. 2- 57 and Eq. 2- 58) and the ΔH_S values are calculated as the difference between E_P and E_D (Eq. 2- 60). The results were listed in the Appendix 7.2.1.3. The uncertainties of the parameters are estimated following the methods presented by Costello.[140] Compared with the literature results, the obtained E_P and E_D values are in the same range but lower than those reported by Costello[140] and Norton[213]. This may be due to dissimilarities of the experimental procedures, including the temperature range and pre-conditioning process.

The activation energy of diffusion, which is a kinetic component of the temperature dependence of permeation, is primarily related to the size and

shape of the penetrants. As shown in Fig. 5- 29, for all of the nanocomposite samples, the calculated E_D values decrease in the order of

$$E_D(CO_2) < E_D(O_2) < E_D(N_2) < E_D(CH_4)$$

This corresponds to the kinetic diameter of the penetrants (Tab. 5- 4):

$$\sigma_k(CO_2) < \sigma_k(O_2) < \sigma_k(N_2) < \sigma_k(CH_4)$$

The activation energy of diffusion of the gas molecules increases with increasing penetrant size. This because that the large-scale motions of polymer segments enable the diffusion of the penetrants with relatively bigger size by producing gaps or channels to allow these gas molecules to permeate through.

In Fig. 5- 29, the activation energies of diffusion of the nanocomposites show a difference dependent on the concentration of POSS at lower concentrations compared to higher concentrations. For lower concentrations of POSS (w_{POSS} < 15 wt%), the E_D values initially decrease with the POSS concentration. This indicates that the enhancement of the polymer segmental motions due to the interaction with the PhenethylPOSS favor the diffusion process of the gas molecules. As a result, the diffusion coefficient of the gas molecules is increasing with the POSS concentration (Fig. 5- 25a). The change of E_D values becomes more complicated when the concentration of POSS is higher than 17 wt%. This is because that the formation of PhenethylPOSS-rich domains gives additional influence on the diffusion of the gas molecules.

Since the ΔH_S values are not directly obtained from the gas permeation measurements, their uncertainties are higher than those of E_D or E_P. The ΔH_S value can be regarded as a thermodynamic component of E_P and depends on the condensability of the penetrant molecules. From this point of view, it is suggested to use the critical temperature to characterize the heat of sorption of the penetrant.[140,214,215] As one of the highly condensable gases, CO_2 has the most negative values of the heat of sorption (shown in Appendix 7.2.1.3).

5.2.1.2 Gas Sorption of PBAC-based PhenethylPOSS Nanocomposites

The gas transport parameters discussed in the previous section were measured by the time-lag method. During the permeation experiments, the solubility of the gas was not directly measured (section 3.2.1). Instead, it was calculated as the ratio of the permeability and the diffusion coefficient following the solution diffusion mechanism (section 2.4.1). For this reason, the obtained solubility and heat of sorption values might have relatively larger errors compared to the permeability and the diffusion coefficients. For this reason, a more precise method, the gas sorption technique (section 3.2.2), was applied to acquire the diffusion coefficient and solubility values (as well as the volume gas concentration c) directly from the experimental results.

Diffusion coefficients

The diffusion coefficients of the gases were estimated by fitting kinetic functions to the data (section 3.2.2). For the gases with lower solubility values, such as N_2 and O_2, the solution of Fick's second law (Eq. 2- 55) was used as description of the sorption process. For the highly sorbing gases, such as CO_2 and CH_4, a penetrant induced relaxation process has to be taken into account, especially at high pressures and penetrant concentration levels. As discussed in section 3.2.2.3, Eq. 3- 12 is applied to kinetically separate the penetrant induced relaxation processes from the Fickian diffusion dominated gas uptake.

The obtained diffusion coefficients are listed in the Appendix 7.3.1 and plotted versus pressure in Fig. 5- 30 to Fig. 5- 33. The calculated values increase with increasing pressure. At each pressure, the diffusion coefficients increase with increasing POSS concentration. This is in agreement with the diffusion coefficients obtained from the plot Fig. 5- 25. For p=10 bar, the diffusion coefficients obtained from gas sorption measurements (open circles in Fig. 5- 34) are compared with the results estimated from the gas permeation measurements (solid symbols in Fig. 5- 34). The two methods give a similar dependence on the POSS concentration.

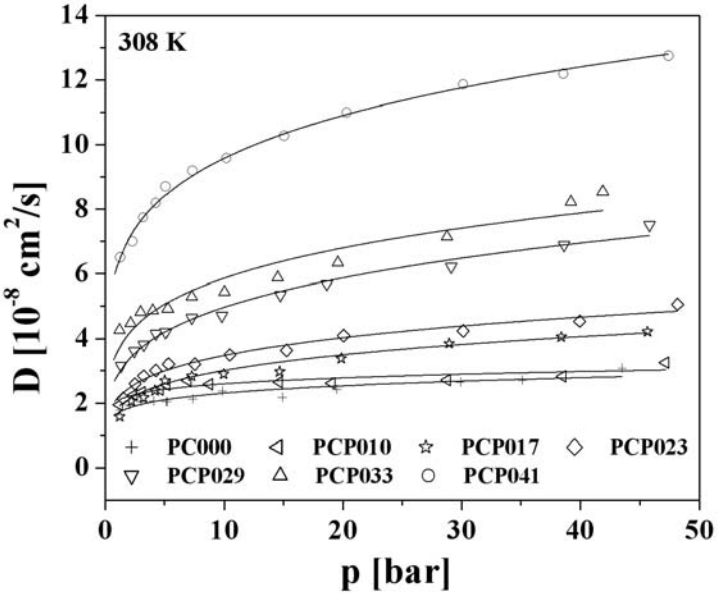

Fig. 5- 30 Diffusion coefficient for CO_2 of PBAC-based PhenethylPOSS nanocomposites versus pressure. Lines are drawn to guide the eyes.

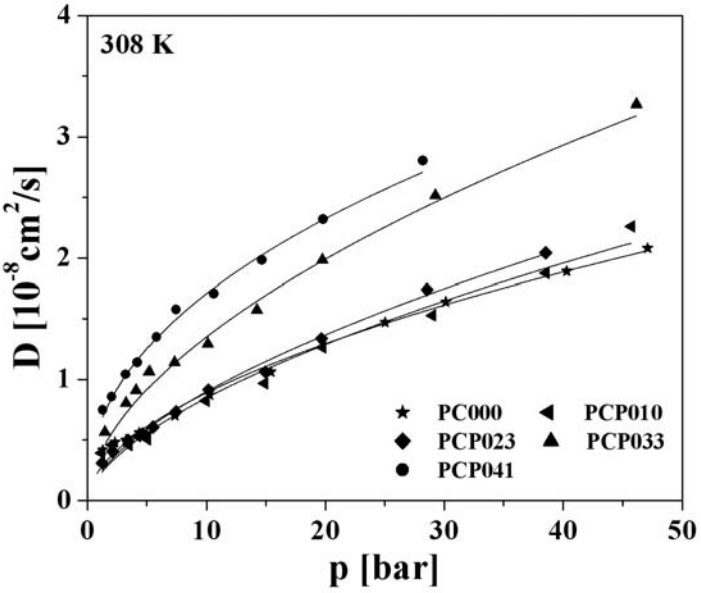

Fig. 5- 31 Diffusion coefficient for CH_4 of PBAC-based PhenethylPOSS nanocomposites versus pressure. Lines are drawn to guide the eyes.

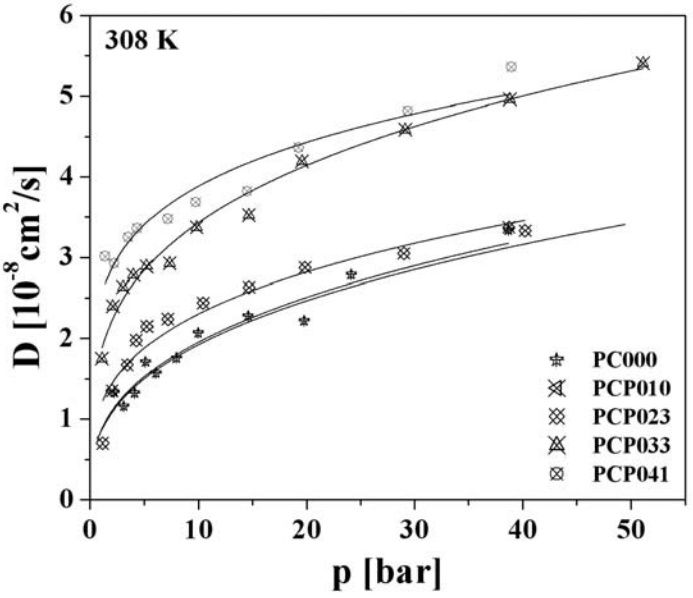

Fig. 5- 32 Diffusion coefficient of N_2 for PBAC-based PhenethylPOSS nanocomposites versus pressure. Lines are drawn to guide the eyes.

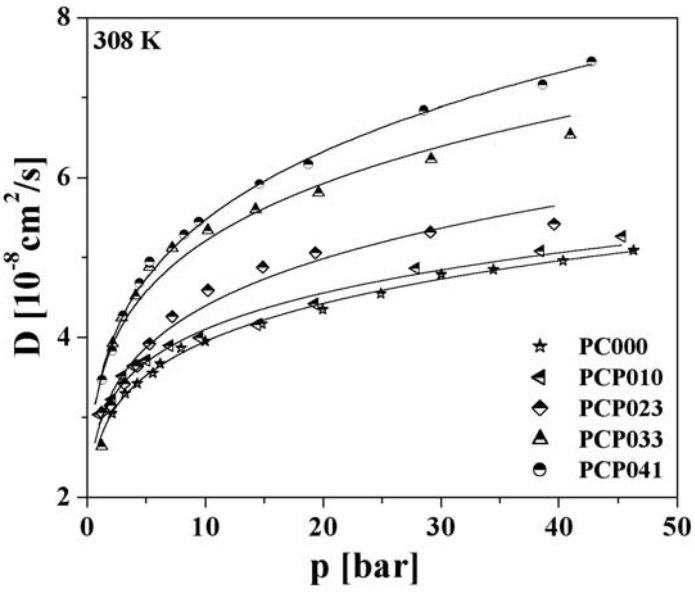

Fig. 5- 33 Diffusion coefficient of O_2 for PBAC-based PhenethylPOSS nanocomposites versus pressure. Lines are drawn to guide the eyes.

For the highly sorbing gases, such as CO_2 and CH_4, the diffusion coefficients obtained from gas sorption measurements are quite similar to those determined from gas permeation measurements. In most cases, the diffusion coefficients obtained from the gas sorption measurements are lower than the ones obtained from the gas permeation measurements.

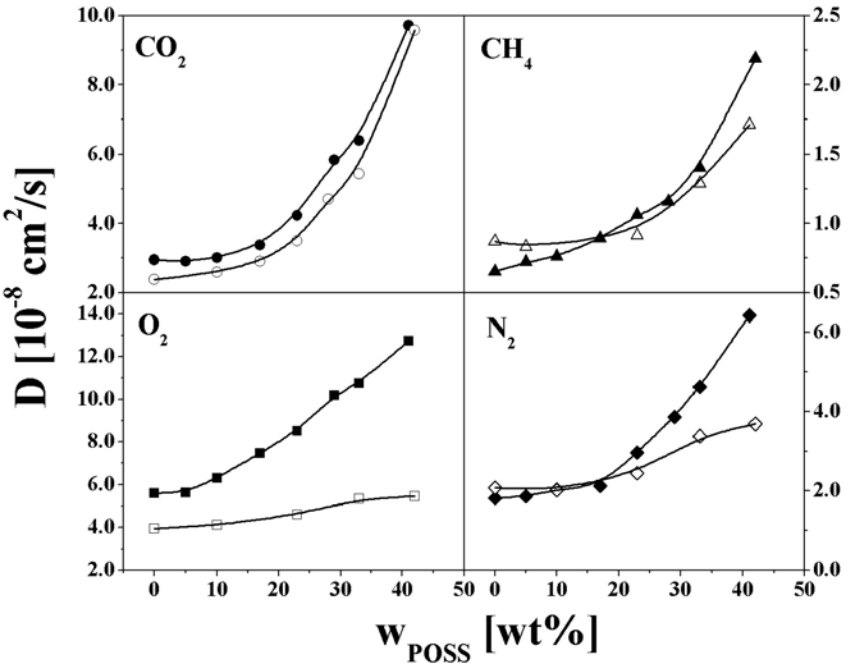

Fig. 5- 34 Comparison of the diffusion coefficients determined from the gas permeation measurements (the solid symbols) and the gas sorption measurements (the open circles). The data are taken at 308 K and 10 bar. Lines are drawn to guide the eyes.

Such differences in the diffusion coefficient have been discussed in the literature in terms of the effective concentration gradient of the gas molecules during gas transport. As shown in Fig. 5- 35, during a gas permeation measurement, a concentration gradient is established across the membrane between the upstream phase and the downstream phase (vacuum) of the membrane. This is not the case for the gas sorption measurement. During a gas sorption measurement, the concentration of the gas molecules is initially uniform at each surface of the sample. From this point of view, the effective concentrations gradient of the penetrant in the two methods is not identical to each other even at the same feed pressure. For this reason, the obtained diffusion coefficient values are not equal to each other.

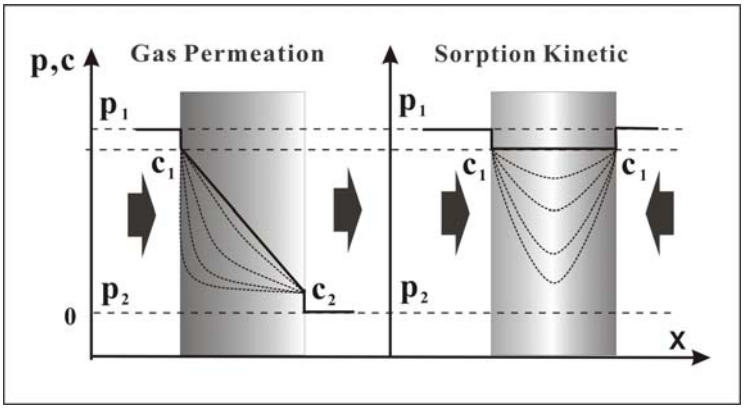

Fig. 5- 35 A schematic illustration on the difference of the concentration gradient between the gas permeation measurement (left) and the gas sorption measurement (right).

For N_2 and O_2, the difference between the diffusion coefficients calculated from the gas permeation and gas sorption measurement is larger than that for the other penetrants. Besides the above-stated reason, the faster diffusion process of these gas molecules may also have a strong influence on the measured diffusivities. In these cases, the time for the sample mass to reach its saturation point is relative short (t_1'-t_1 in Fig. 3- 8), which may bring relatively larger error on determining the value of diffusion coefficient.

Volume Gas Concentration

The volume gas concentration c can be evaluated from the mass uptake of the gas molecules in each sorption step (section 3.2.2.3). The calculated volume gas concentration of all investigated penetrants is plotted in Fig. 5- 36 to Fig. 5- 39. The sorption isotherms (shown as solid curves) are established by fitting the Dual Mode Sorption Model to the data (section 2.4.3.2 and section 3.2.2.3). The insets of the plots show the volume gas concentration at 10 bar and 30 bar versus concentration of PhenethylPOSS in the nanocomposites. The volume gas concentration of the penetrants decreases with the concentration of PhenethylPOSS. This is in agreement with the gas permeation results presented in Fig. 5- 26.

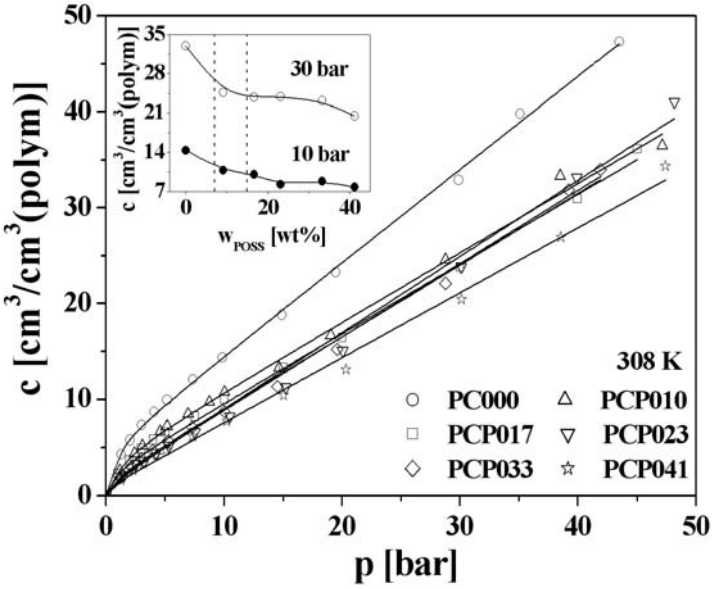

Fig. 5- 36 CO_2 sorption isotherms of PBAC-based PhenethylPOSS nanocomposites at 308K. The lines are fitted by DMSM. The inset of the picture shows the volume gas concentration at 10 bar (solid symbols) and 30 bar (open symbols) versus POSS concentration. The solid lines are drawn to guide the eyes. The dashed lines represent the content of POSS at 7 wt% and 15 wt%.

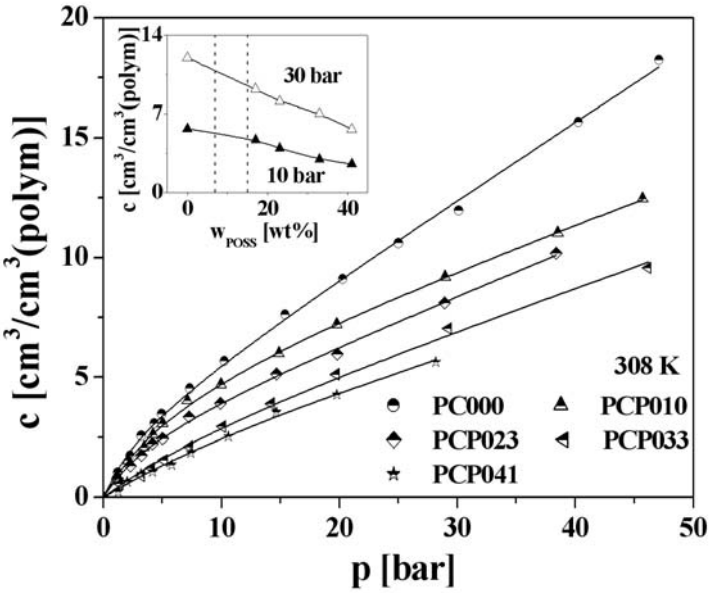

Fig. 5- 37 CH_4 sorption isotherms of PBAC-based PhenethylPOSS nanocomposites at 308K. The lines are fitted by DMSM. The inset of the picture shows the volume gas concentration at 10 bar (solid symbols) and 30 bar (open symbols) versus the concentration of POSS. The solid lines are drawn to guide the eyes. The dashed lines represent the concentration of POSS at 7 wt% and 15 wt%

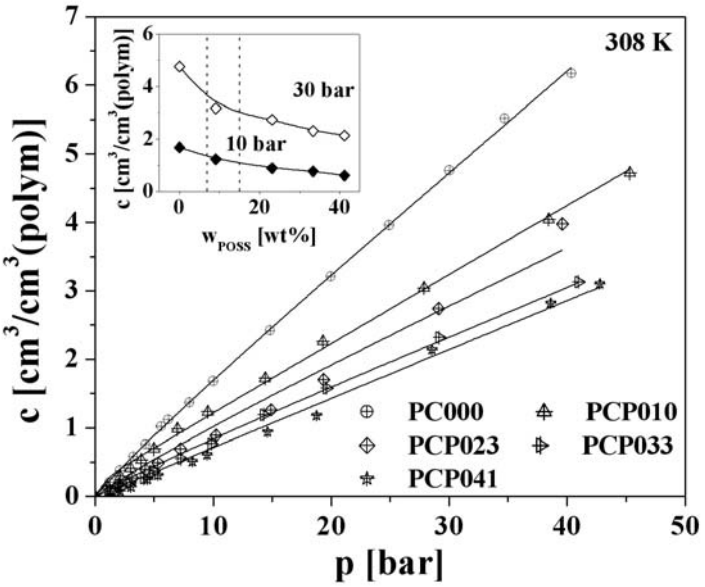

Fig. 5- 38 O_2 sorption isotherms of PBAC-based PhenethylPOSS nanocomposites at 308K. The lines are fitted by DMSM. The inset of the picture shows the volume gas concentration at 10 bar (solid symbols) and 30 bar (open symbols) versus the concentration of POSS. The solid lines are drawn to guide the eyes. The dashed lines represent the concentration of POSS at 7 wt% and 15 wt%

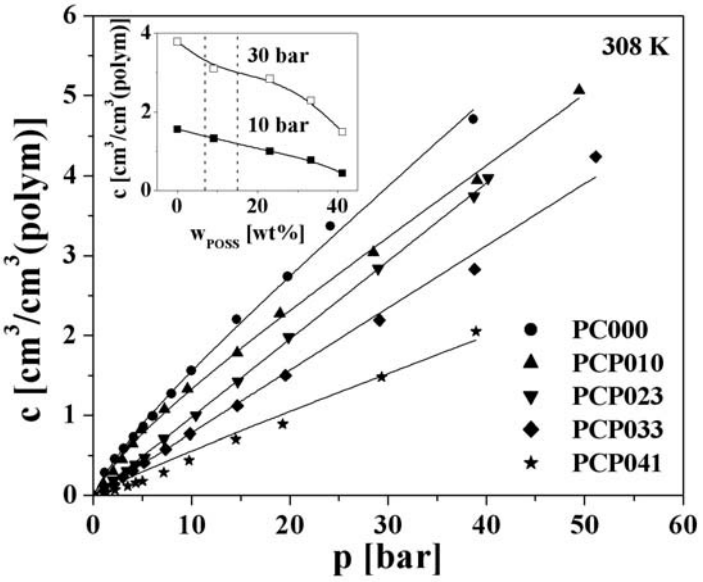

Fig. 5- 39 N_2 sorption isotherms of PBAC-based PhenethylPOSS nanocomposites at 308K. The lines are fitted by DMSM. The inset of the picture shows the volume gas concentration at 10 bar (solid symbols) and 30 bar (open symbols) versus the concentration of POSS. The solid lines are drawn to guide the eyes. The dashed lines represent the concentration of POSS at 7 wt% and 15 wt%

Tab. 5- 7 DMSM parameters for CO_2 in PBAC-based PhenethylPOSS nanocomposites*

Sample	k_d	c_H'	b
PC000	0.97	5.10	1.57
PCP010	0.72	3.82	0.92
PCP017	0.72	3.90	2.05
PCP023	0.45	3.58	0.47
PCP033	0.47	3.54	0.39
PCP041	0.42	3.07	0.49

Tab. 5- 8 DMSM parameters for CH_4 in PBAC-based PhenethylPOSS nanocomposites*

Sample	k_d	c_H'	b
PC000	0.32	3.12	0.27
PCP010	0.22	3.65	0.21
PCP023	0.20	2.86	0.22
PCP033	0.18	2.83	0.08
PCP041	0.16	2.76	0.03

Tab. 5- 9 DMSM parameters for O_2 in PBAC-based PhenethylPOSS nanocomposites*

Sample	k_d	c_H'	b
PC000	0.11	0.77	0.17
PCP010	0.10	0.77	0.16
PCP023	0.09	0.68	0.01
PCP033	0.08	0.63	0.04
PCP041	0.05	0.19	0.11

Tab. 5- 10 DMSM parameters for N_2 in PBAC-based PhenethylPOSS nanocomposites*

Sample	k_d	c_H'	b
PC000	0.15	0.48	0.10
PCP010	0.10	0.22	2.67
PCP023	0.08	0.23	0.08
PCP033	0.07	0.26	0.10
PCP041	0.07	0.10	0

***: $[k_d] = cm^3(STP)cm^{-3}(polym.)(cmHg)^{-1}$; $[c_H'] = cm^3(STP)cm^{-3}(polym.)$; $[b]=bar^{-1}$**

The DMSM fitting parameters are listed in the Tab. 5- 7 to Tab. 5- 10. The fitting results show that both the Henry parameter k_d and Langmuir parameter c_H' decrease with the PhenethylPOSS concentration.

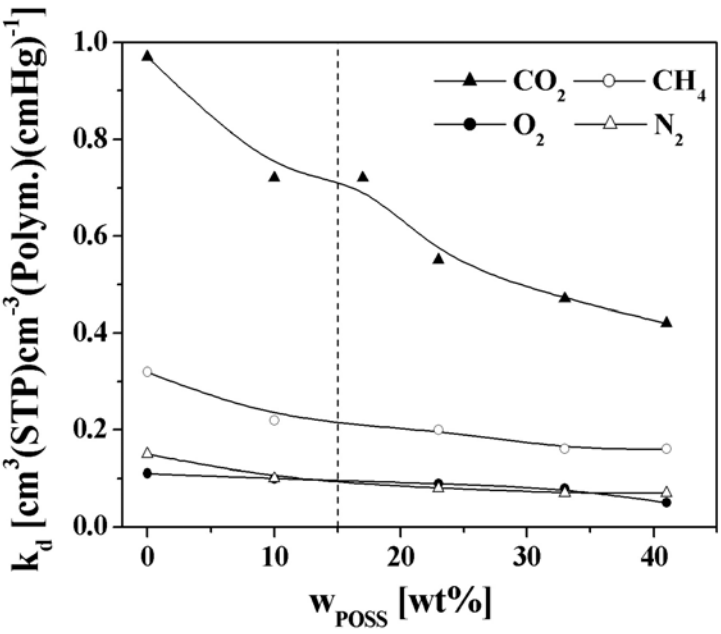

Fig. 5- 40 k_d versus PhenethylPOSS concentration. The lines are drawn to guide the eyes.

For all the penetrants, k_d is plotted versus w_{POSS} in Fig. 5- 40. As shown in the plot, k_d decreases with the concentration of POSS in all cases. According to the DMSM discussed in section 2.4.3.2, the decrease indicates that the fraction of highly fluctuating free volume of the polymer matrix is decreasing as the concentration of POSS is increasing. It can be further concluded that adding PhenethylPOSS enhances the molecular mobility of the PBAC matrix. This conclusion corresponds to the arguments given from the density measurements (Fig. 5- 2), which shows an increased packing density of the PBAC chains in the higher concentration range. On the other hand, Tab. 5- 7 to Tab. 5- 10 show that the c_H' values are also decreased as the concentration of POSS is increasing. Such a modified behavior implies the fraction of frozen-in free volume is reduced due to adding PhenethylPOSS molecules.

5.2.1.3 Gas Sorption of PS-based PhenethylPOSS Nanocomposites

As discussed in section 4.4, most of the samples prepared by PS-based PhenethylPOSS nanocomposites were brittle. Therefore, they were not suitable for the gas permeation measurements. Only the samples with lower Phenethyl-

POSS concentration (<25 wt%) could be obtained as films suitable for the gas sorption measurements. It has to be noted that the gas sorption measurements of O_2 and N_2 were excluded from this discussion, since the fast diffusion processes of these gas molecules cause difficulties on separating the buoyancy effect from the kinetic sorption curve.

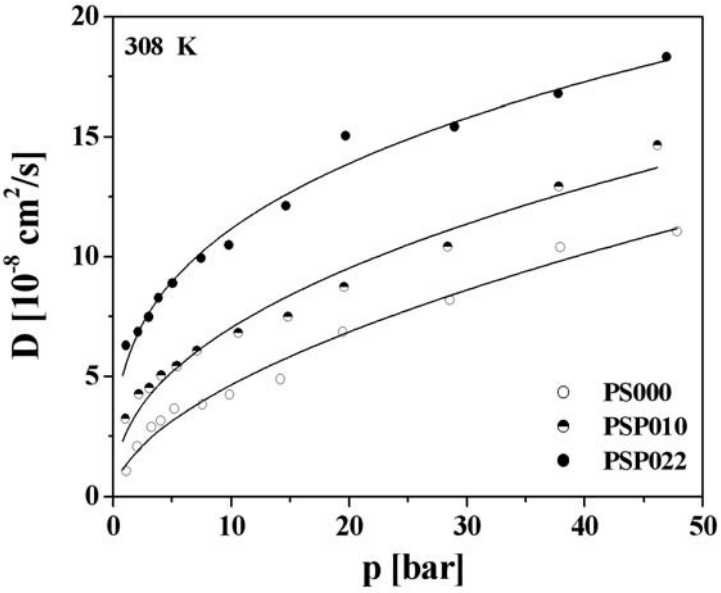

Fig. 5- 41 Diffusion coefficient of CO_2 for PS-based PhenethylPOSS nanocomposites versus pressure. Lines are drawn to guide the eyes.

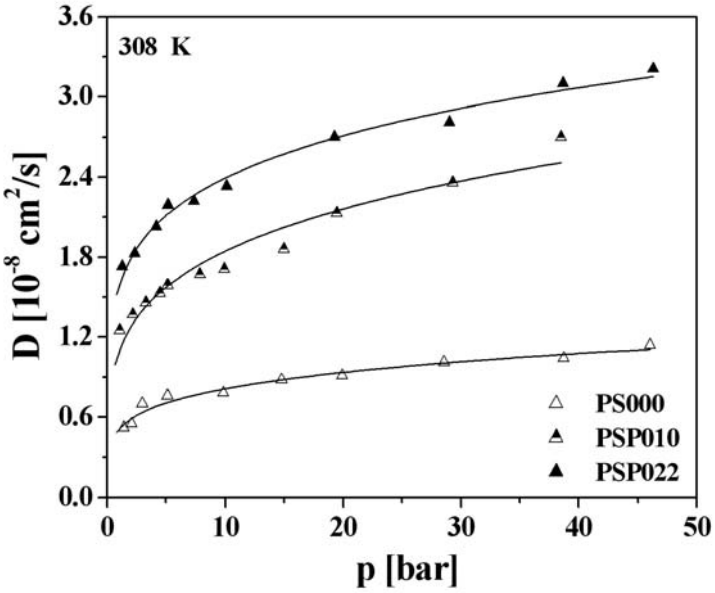

Fig. 5- 42 Diffusion coefficient of CH_4 for PS-based PhenethylPOSS nanocomposites versus pressure. Lines are drawn to guide the eyes.

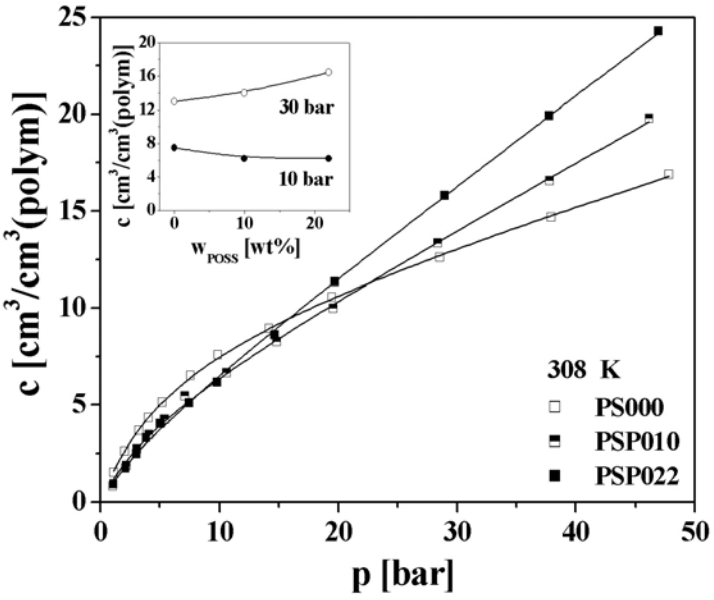

Fig. 5- 43 CO_2 sorption isotherms of PS-based PhenethylPOSS nanocomposites at 308K. The lines are fitted by DMSM. The inset of the picture shows the volume gas concentration at 10 bar (solid symbols) and 30 bar (open symbols) versus the concentration of POSS. The solid lines are drawn to guide the eyes.

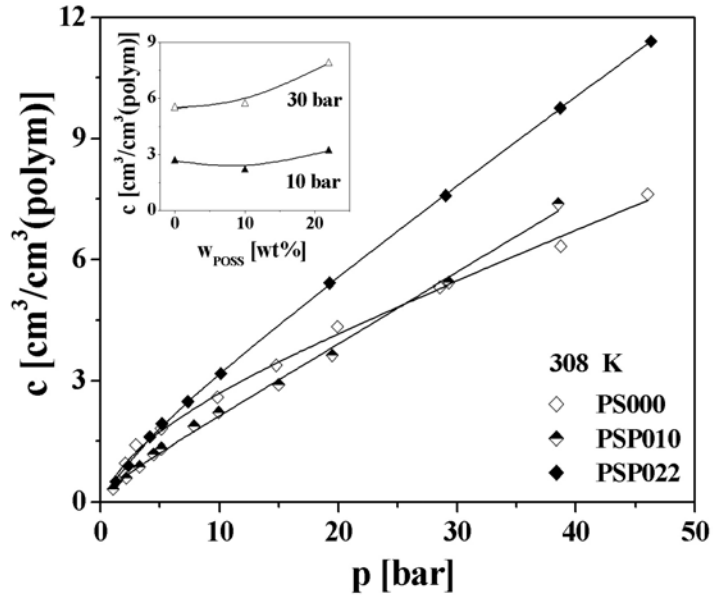

Fig. 5- 44 CH_4 sorption isotherms of PS-based PhenethylPOSS nanocomposites at 308K. The lines are fitted by DMSM. The inset of the picture shows the volume gas concentration at 10 bar (solid symbols) and 30 bar (open symbols) versus the concentration of POSS. The solid lines are drawn to guide the eyes.

The obtained diffusion coefficients of CO_2 and CH_4 are listed in Appendix 7.3.2 and plotted versus pressure in Fig. 5- 41 and Fig. 5- 42. The diffusion

coefficients of the gas in PS-based PhenethylPOSS nanocomposites increase with pressure. At each specific pressure, the presence of PhenethylPOSS leads to higher diffusion coefficients. This can be understood taking into account that adding PhenethylPOSS enhances molecular mobility of the PS (section 5.1.1.2). As a result, the higher molecular mobility of the PS segments allows a faster transport of the gas molecules through the nanocomposites.

Tab. 5- 11 DMSM parameters for CO_2 in PS-based PhenethylPOSS nanocomposites*

Sample	k_d	c_H'	b
PS000	0.18	9.36	0.16
PSP010	0.34	4.56	0.20
PSP022	0.46	2.90	0.20

Tab. 5- 12 DMSM parameters for CH_4 in PS-based PhenethylPOSS nanocomposites*

Sample	k_d	c_H'	b
PS000	0.12	2.17	0.23
PSP010	0.18	1.88	0.19
PSP022	0.21	1.74	0.15

***: $[k_d] = cm^3(STP)cm^{-3}(polym.)(cmHg)^{-1}$; $[c_H'] = cm^3(STP)cm^{-3}(polym.)$; $[b]=bar^{-1}$**

The concentration of CO_2 and CH_4 in the PS-based PhenethylPOSS nanocomposites can be determined from the gas sorption measurements. The calculated volume concentration values are listed in Appendix 7.3.2. The observed sorption isotherms of the samples are well represented by the fitting curve obeying the DMSM (shown in Fig. 5- 43 and Fig. 5- 44). The DMSM fitting parameters are listed in Tab. 5- 11 and Tab. 5- 12.

In contrast to the PBAC-based PhenethylPOSS nanocomposites, the volume gas concentration of the gas molecules in PS-based nanocomposites shows different dependence on the concentration of PhenethylPOSS. In general, adding POSS molecules into the polymer matrix increases the Henry parameter k_d and reduces the Langmuir capacity c_H'. According to the section 2.4.3.2, the increased k_d value corresponds to the increasing fraction of the highly fluctuating free volume of the matrix polymer. This argument is in agreement with the results of dielectric measurements given in Fig. 5- 14, which shows

the cooperative molecular mobility of the PS matrix is enhanced due to adding of PhenethylPOSS molecules.

5.2.2 Nanocomposites based on ChloropropylPOSS

The gas permeation measurement of PBAC-based ChloropropylPOSS nanocomposites was carried out at 10 bar at 308 K. The calculated transport parameters are listed in Appendix 7.2.2. The permeability and relative permeability values are plotted in Fig. 5- 45 versus concentration of ChloropropylPOSS.

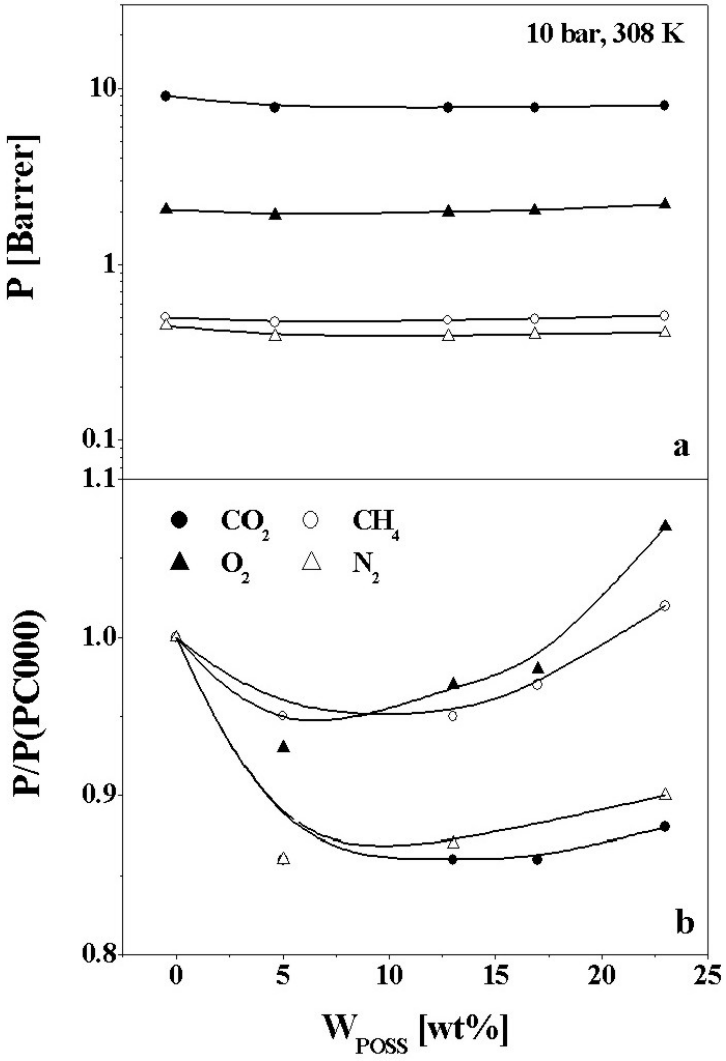

Fig. 5- 45 Permeability of all penetrants through PBAC-based ChloropropylPOSS nanocomposites versus POSS concentration at 10 bar feed pressure and 308 K. b: The relative permeability values of the penetrants versus POSS concentration under the same conditions. Lines are drawn to guide the eyes.

It needs to be mentioned that during the gas permeation measurements of the samples PCC029 and PCC033, a dramatically increased downstream pressure can be observed after the instantaneous upstream pressure change. In this case, no time-lag process can be identified from the pressure-time plot. As shown in Fig. 5- 45, blending ChloropropylPOSS into PBAC shows limited influence on the permeability of the nanocomposites. The measured permeability values are slightly decreasing with the concentration of POSS initially, but increase when the concentration of POSS is above 10 wt%.

Considering the results of dielectric measurements in the previous section 5.1.1.2, ChloropropylPOSS forms crystalline domains inside PBAC-rich phase. Because these crystallized domains has only limited influence on the segmental mobility of the PBAC matrix. The gas transport parameters remain nearly constant as the lower concentrations. Furthermore, it is presumed that the size of these crystalline domains increases as the concentration of POSS is increasing. In higher concentration range, these separate phases induce mechanical defects, such as leakages in small scale, which allows faster transport of gas molecules. In this case, the sample membranes are not nonporous and the downstream pressure increases dramatically after the measurement starts.

6 Conclusion

In this work, Polyhedral Oligomeric Silsesquioxane (POSS) molecules were blended into polymer matrix to prepare nanocomposites. In order to characterize the influence of the sidegroup polarity of the POSS molecules, PhenethylPOSS and the ChloropropylPOSS were applied as nanofillers. Poly(bisphenol A carbonate) (PBAC) and the polystyrene (PS), were used as matrix polymers. The nanocomposite films were prepared by film-casting under optimized conditions. The evaporation of the solvent was controlled by adjusting the vapor pressure of the solvent in a closed chamber. As a result homogeneous and almost transparent films were obtained by this procedure for a reasonable concentration range of POSS from 0 to 40 wt%.

Three different types of nanocomposites, PBAC-based Phenethyl-POSS nanocomposites, PBAC-based ChloropropylPOSS nanocomposites and PS-based PhenethylPOSS nanocomposites were obtained. The sample films were annealed below their glass transition temperature in order to sustain the planarity and uniform thickness of the polymer films. The flexibility of PBAC-based PhenethylPOSS nanocomposites increases as the concentration of POSS is increasing, while the flexibility of the others decreases as the concen-tration of POSS is increasing.

The physical properties of the nanocomposites were investigated by different methods. The density of the sample is measured by Density Gradient Column (DGC). The glass transition temperature of the sample was determined by DSC (Differential Scanning Calorimetry). The structure-property relationships of samples were investigated by dielectric relaxation spectroscopy and gas transport measurements. The obtained sample properties are listed in Tab. 6- 1.

Tab. 6- 1 Summary of the physical properties of the nanocomposites

	PhenethylPOSS	ChloropropylPOSS
PBAC	**Lower concentrations**: POSS molecules can be mixed into PBAC on a molecular level • The density of samples decreases as the concentration of POSS increases • The dynamic glass transition temperature shifts to lower temperatures. • No significant changes on the gas permeability **Higher concentrations**: POSS molecules forms separated phases inside nanocomposites • The density of the sample increases as the concentration of POSS increases. • No significant changes on the dynamic glass transition temperature. • The gas permeability of the sample is increasing with POSS concentration.	• Dynamic glass transition temperatures of the nanocomposites are almost identical to each other but slightly higher than that of the pure PBAC. • No significant change on gas permeation properties below 25 wt%.
PS	• The density of samples increases as the concentration of POSS increases. • The dynamic glass transition temperature is decreasing with the concentration of POSS. • The dynamic glass transition temperature has less deviation from the prediction given by Fox function.	Samples are not suitable for the measurements

Dielectric spectroscopy shows that for low concentrations of Phenethyl-POSS (below 10 wt %) the dynamic glass transition process of the PBAC matrix is shifted to lower temperatures with increasing PhenethylPOSS concentration. This means at this concentrations level PhenethylPOSS acts as a plasticizer. In contrast to low molecular weight plasticizers, this plasticization effect is due to the reduced molecular packing density (increase of free volume), which is experimentally confirmed by density measurements. For higher concentrations of PhenethylPOSS (above 10 wt %) the dielectric spectra show a double peak structure. The two corresponding relaxation processes are assigned to the dynamic glass transitions of a PBAC-rich phase and an interfacial layer having higher concentrations of PhenethylPOSS. In parallel at temperatures close to the glass transition temperature of PhenethylPOSS, a third peak is observed with an increased intensity as the content of Phenethyl-POSS is increasing. This relaxation process is assigned to the dynamic glass transition of PhenethylPOSS-rich domains. As the concentration of Phenethyl-POSS is increasing, this relaxation process shifts to lower temperatures.

From the DSC measurements and the dielectric studies, a phase diagram of nanocomposites is deduced. This phase diagram shows that PhenethylPOSS is miscible in PBAC on a molecular level up to 7 wt%. Approximately the same concentration limit for the molecular miscibility of PhenethylPOSS into PBAC is obtained by a quantitative analysis of the α-relaxation of PBAC. Its activation energy decreases up to 10 wt% of dispersed PhenethylPOSS and remains constant at this level for higher concentrations of POSS. For the phase separate nanocomposites, in addition to the relaxation processes, an interfacial polarization process is observed. It is assigned to the blocking of charge carriers at internal phase boundaries. The relative growth of these separate phases with concentration of PhenethylPOSS can be estimated by analyzing the time constant of MWS polarization process.

Such morphological modifications can also be investigated by the gas transport measurements. The gas permeability of the samples is constant at lower concentrations but increases above 15 wt% of PhenethylPOSS. That is because the faster diffusion process of the gas molecule in PhenethylPOSS-rich phase than in PBAC matrix. Similar changes are observed from the change of

activation energy of diffusion of the gas molecules. The sorption isotherms of the nanocomposites can be well described by the Dual Mode Sorption Model (DMSM). Analyzing the fitting parameters with the concentration of POSS, it shows that both the fraction of fluctuating free volume and the fraction of 'frozen-in' free volume of the nanocomposites are reduced as the concentration of POSS increases. That is in agreement with the conclusion given from the dielectric measurement.

Blending PhenethylPOSS into PS forms brittle samples. The α-relaxation process of pure PS shifts to the lower temperatures as the concentration of POSS is increasing. It corresponds to the reduction of the glass transition temperature of the sample measured by DSC. Compared to the phase diagram of PBAC-based PhenethylPOSS nanocomposites, the dynamic glass transition temperature of PS-based PhenethylPOSS nanocomposites have less deviation from the prediction given by the Fox function. That indicates the Phenethyl-POSS molecules are dispersed into the PS matrix on molecular level up to a higher concentration. This effect is attributed to the specific interaction between the phenyl sidegroups of PS and the phenethyl sidegroups of POSS. In addition, this interaction behavior also influences the gas transport properties of the nanocomposites as well. As shown from the result of gas sorption measurements, due to the enhanced segmental mobility of PS matrix, the diffusion coefficient of penetrants are increasing as the concentration of POSS increases. Compared to the DMSM parameters of PBAC-based PhenethylPOSS nanocomposites, the DMSM parameters of PS-based PhenethylPOSS nanocomposites have different dependence on the oncentration of POSS.

Blending ChloropropylPOSS into PBAC does not change the α- and β-relaxation processes of PBAC significantly. Instead, it is presumed that the ChloropropylPOSS molecules crystallize inside the PBAC matrix and form separated domains. Such crystallized domains have only limited influence on the molecular mobility of the PBAC matrix but enhance the conductivity of nanocomposites. In this concentration range, blending POSS molecules into PBAC have only limited influence on the permeability of the sample.

7 Appendix

7.1 Index of Symbols, Abbreviations and Constants

7.1.1 List of Symbols

A	effective area of permeation
A_0	constant of VFTH function
A_i	area of each layer (double layer model)
b	hole affinity constant
c	concentration of the gas
c_H'	hole saturation constant (Langmuir capacity)
C(ω)	complex capacity
d	thickness of each layer (double layer model)
D, D(ω)	dielectric displacement, complex dielectric displacement
D	diffusion coefficient (gas transport)
E, E(ω)	electric field, periodical electric field
E_A	activation energy of secondary relaxation
E_D	activation energy of diffusion
E_P	activation energy of permeation
F	Onsager's parameter
f	frequency
f_p	relaxation rate
f_∞	frequency pre-exponential factor
g	Kirkwood-Fröhlich correlation factor
G, G´,G´´	complex shear modulus, real part of the complex shear modulus and imaginary part of the complex shear modulus
J	flux of a substance diffusing through a membrane
J_S	steady state flux
l	thickness of the sample film
k_d	Henry parameter
L_D	Debye length

m, m_t, m_∞	mass of the sample, mass of the sample at time t and equilibrium mass of sorption attained theoretically after infinite time
$\mathbf{P}$	polarization (dielectric relaxation)
P	permeability (gas transport)
p	pressure
$\mathbf{p}_i$	microscopic dipole moments
$\mathbf{P}_\infty$	induced polarization
R	organic side groups
R_i	electrical resistance
S	solubility,
T	temperature
T_g	glass transition temperature
T_0^{id}	ideal glass transition temperature calculated from VFTH function
U*	voltage
V*	minimum free volume required for a 'jump'
V_f	free volume
$\overline{V_f}$	average free volume
V_S	specific volume
V_0	occupied volume
V_2	downstream volume
w_i	weighting factor
w_{POSS}	Weight fraction of the POSS molecules in the polymer material
x	coordination of gas molecules during transport
$Z^*(\omega)$	complex dielectric impedance
z(T)*	number of molecules in the CRR
ΔH_S	enthalpy of sorption
α_f	thermal expansion factor
α(A/B)	perm-selectivity
$\Delta\varepsilon$	relaxation strength
$\sigma^*(\omega)$ σ', σ''	complex conductivity, real part of the complex conductivity and imaginary part of the complex conductivity
$\varepsilon^*(\omega)$, $\varepsilon', \varepsilon''$	complex dielectric function, real part of the complex dielectric function and imaginary part of the complex dielectric function
ε_S	dielectric storage at time 0
ε_∞	dielectric storage at infinite time
Φ (t)	autocorrelation function
$\boldsymbol{\mu}_i$	permanent dipoles
ρ	density
$\tau_{CC}, \tau_{CD}, \tau_D, \tau_{HN}$	characteristic time of the Cole-Cole, Cole-Davidson, Debye and Havriliak-Negami functions
ω	angular frequency
ξ	cooperative length of CRR

7.1.2 List of Abbreviations

ATR-IR	Attenuated Total Reflection Infrared Spectroscopy
BDRS	Broadband Dielectric Relaxation Spectroscopy
CC	Cole-Cole function
CD	Cole-Davidson function
CRR	Cooperatively Rearrange Region
DCM	dichloromethane
DGC	Density Gradient Column
DMSM	Dual Mode Sorption Model
DMSO	dimethyl sulfoxide
DSC	Differential Scanning Calorimetry
FTIR	Fourier Transform Infrared Spectroscopy
FV	Free Volume Assumption
GPMM	Gas Polymer Matrix Model
HDPE	high density polyethylene
HN	Havriliak-Negami function
KK	Kramers-Kronig relation
FDT	Fluctuation Dissipation Theorem
MCT	Molecular-Coupling Theory
DMA	Dynamic-Mechanical Analysis
MWS	Maxwell-Wagner-Sillars polarization
NMR	nuclear magnetic resonance
PBAC	poly(bisphenol A carbonate)
PEN	polyethylene naphthalate
PET	poly(ethylene terephthalate)
PMMA	poly(methyl methacrylate)
POSS	polyhedral Oligomeric Silsesquioxane
PP	Polypropylene
PS	Polystyrene
PVC	poly(vinyl chloride)
THF	tetrahydrofuran
TGA	Thermal Gravimetric Analysis
VFTH	Vogel-Fulcher-Tammann-Hesse function

7.1.3 List of Constants

k_B	Boltzmann constant $k_B = 1.381 \times 10\text{-}23\ m^2\ kg\ s^{-2}\ K^{-1}$
i	complex unit $i = \sqrt{-1}$
p_0	standard pressure $p_0 = 76$ mmHg $= 1.013$ bar
R	ideal gas constant $R = 8.314\ Jmol^{-1}K^{-1}$
ε_0	dielectric permittivity constant in vacuum $\varepsilon_0 = 8.854x10^{-12}\ AsV^{-1}m^{-1}$

7.2 Results of Gas Permeation Measurements

7.2.1 PBAC-based PhenethylPOSS Nanocomposites

7.2.1.1 Pressure-dependent Permeability of CO_2 at 308 K

PC000

p_1 [bar]	P [Barrer]	D [10^{-8} cm^2s^{-1}]	S [10^{-2} cm^3(STP) cm^{-3}(Polym.)$cmHg^{-1}$]
1.02	11.95	1.58	7.75
2.11	9.79	2.09	5.75
2.98	9.14	2.23	4.61
4.02	8.73	2.37	4.34
5.24	8.35	2.44	4.12
7.13	8.01	2.59	3.72
10.43	8.02	2.95	3.04
15.60	7.24	3.31	2.55
20.92	6.99	3.70	2.17

PCP0050

p_1 [bar]	P [Barrer]	D [10^{-8} cm^2s^{-1}]	S [10^{-2} cm^3(STP) cm^{-3}(Polym.)$cmHg^{-1}$]
0.94	11.78	1.59	7.41
1.97	10.25	2	5.13
2.99	9.43	2.16	4.37
4.08	8.92	2.28	3.91
5.31	8.54	2.47	3.46
7.41	8.03	2.64	3.04
10.09	7.95	2.91	2.73
15.02	7.2	3.13	2.30
20.06	6.58	3.48	1.89

PCP010

p_1 [bar]	P [Barrer]	D [10^{-8} cm^2s^{-1}]	S [10^{-2} cm^3(STP) cm^{-3}(Polym.)$cmHg^{-1}$]
1.08	11.54	1.79	6.45
1.95	9.96	1.96	5.08
2.95	9.28	2.17	4.27
3.97	8.81	2.31	3.81
5.01	8.51	2.40	3.54
7.02	7.94	2.69	2.95
10.42	7.96	3.00	2.65
15.23	7.03	3.35	2.10
20.59	6.58	3.77	1.74

PCP017

p_1 [bar]	P [Barrer]	D [10^{-8} cm^2s^{-1}]	S [10^{-2} cm^3(STP) cm^{-3}(Polym.)$cmHg^{-1}$]
1.02	11.95	2.29	5.22
2.11	9.79	2.32	4.22
2.98	9.14	2.41	3.79
4.02	8.73	2.59	3.37
5.24	8.35	2.71	3.07
7.13	8.01	2.87	2.79
10.43	8.02	3.37	2.38
15.60	7.24	3.58	2.02
20.92	6.99	3.97	1.76

PCP023

p_1 [bar]	P [Barrer]	D [10^{-8} cm^2s^{-1}]	S [10^{-2} cm^3(STP) cm^{-3}(Polym.)$cmHg^{-1}$]
0.99	12.06	1.99	6.05
1.95	11.17	2.48	4.5
2.98	10.51	3.03	3.47
3.95	10.03	3.41	2.94
4.97	9.94	3.35	2.97
7.61	9.22	3.90	2.37
10.21	9.01	4.23	2.13
15.14	8.94	4.53	1.98
20.53	8.68	5.12	1.69

PCP029

p_1 [bar]	P [Barrer]	D [10^{-8} cm^2s^{-1}]	S [10^{-2} cm^3(STP) cm^{-3}(Polym.)$cmHg^{-1}$]
0.99	16.72	3.66	4.57
1.99	13.9	3.71	3.74
2.96	12.91	4.01	3.22
3.95	12.14	4.04	3.01
5.07	11.79	4.23	2.79
10.11	10.98	4.89	2.25
15.18	10.72	5.38	1.99
20.61	10.3	6.13	1.68

PCP033

p_1 [bar]	P [Barrer]	D [10^{-8} cm^2s^{-1}]	S [10^{-2} cm^3(STP) cm^{-3}(Polym.)$cmHg^{-1}$]
0.96	20.96	4.45	4.71
1.99	17.49	4.72	3.70
3.00	14.27	4.83	2.95
3.94	14.01	4.95	2.83
5.02	13.86	5.39	2.57
7.60	13.2	5.88	2.24
10.15	12.5	6.40	1.95
15.12	11.48	7.69	1.49
20.65	10.63	8.11	1.31

PCP041

p_1 [bar]	P [Barrer]	D [10^{-8} cm^2s^{-1}]	S [10^{-2} cm^3(STP) cm^{-3}(Polym.)$cmHg^{-1}$]
0.96	23.47	6.81	3.46
1.98	19.21	7.38	2.62
3.11	18.21	7.64	2.40
4.01	18.01	8.02	2.26
5.18	17.19	8.37	2.06
8.04	16.79	9.11	1.75
10.15	16.50	9.76	1.70
15.11	15.71	11.2	1.41
20.51	14.35	11.2	1.23

7.2.1.2 Temperature-dependent Permeability at 10 bar

PC000

	T [K]	P [Barrer]	D [10^{-8} cm^2s^{-1}]	S [10^{-2} cm^3(STP) cm^{-3}(Polym.)$cmHg^{-1}$]
CO_2	308	8.19	2.95	2.78
	318	9.46	4.41	2.14
	328	10.82	6.44	1.68
	338	12.29	9.20	1.33
CH_4	308	0.5	0.65	0.77
	318	0.63	1.05	0.60
	328	0.79	1.65	0.48
	338	0.98	2.53	0.39
O_2	308	1.64	5.61	0.31
	318	2.04	8.76	0.25
	328	2.51	13.32	0.20
	338	3.05	19.74	0.16
N_2	308	0.45	1.81	0.25
	318	0.58	2.85	0.20
	328	0.74	4.38	0.17
	338	0.93	6.55	0.14

PCP005

	T [K]	P [Barrer]	D [10^{-8} cm^2s^{-1}]	S [10^{-2} cm^3(STP) cm^{-3}(Polym.)$cmHg^{-1}$]
CO_2	308	7.95	2.91	2.73
	318	9.10	4.30	2.12
	328	10.33	6.21	1.66
	338	11.64	8.76	1.33
CH_4	308	0.53	0.69	0.77
	318	0.67	1.11	0.61
	328	0.84	1.73	0.49
	338	1.03	2.62	0.39
O_2	308	1.76	6.02	0.29
	318	2.23	9.24	0.24
	328	2.78	13.82	0.20
	338	3.42	20.18	0.17
N_2	308	0.47	2.02	0.23
	318	0.59	3.16	0.19
	328	0.74	4.81	0.15
	338	0.91	7.13	0.13

PCP010

	T [K]	P [Barrer]	D [10^{-8} cm^2s^{-1}]	S [10^{-2} cm^3(STP) cm^{-3}(Polym.)$cmHg^{-1}$]
CO_2	308	7.96	3	2.65
	318	9.07	4.39	2.07
	328	10.25	6.28	1.63
	338	11.49	8.79	1.31
CH_4	308	0.55	0.78	0.71
	318	0.70	1.24	0.56
	328	0.87	1.93	0.45
	338	1.07	2.91	0.37
O_2	308	1.85	6.69	0.28
	318	2.33	10.13	0.23
	328	2.89	14.96	0.19
	338	3.55	21.59	0.16
N_2	308	0.47	2	0.24
	318	0.59	3.10	0.19
	328	0.74	4.67	0.16
	338	0.91	6.87	0.13

PCP017

	T [K]	P [Barrer]	D [10^{-8} cm^2s^{-1}]	S [10^{-2} cm^3(STP) cm^{-3}(Polym.)$cmHg^{-1}$]
CO_2	308	8.02	3.37	2.08
	318	8.64	4.80	1.58
	328	9.27	6.69	1.21
	338	9.91	9.14	0.95
CH_4	308	0.59	8.97	0.66
	318	0.75	14.16	0.53
	328	0.93	21.75	0.43
	338	1.14	32.57	0.35
O_2	308	2.09	7.48	0.28
	318	2.56	10.93	0.23
	328	3.09	15.61	0.20
	338	3.69	21.83	0.17
N_2	308	0.48	2.12	0.24
	318	0.61	3.22	0.20
	328	0.77	4.78	0.17
	338	0.95	6.91	0.15

PCP023

	T [K]	P [Barrer]	D [10^{-8} cm^2s^{-1}]	S [10^{-2} cm^3(STP) cm^{-3}(Polym.)$cmHg^{-1}$]
CO_2	308	9.01	4.23	2.13
	318	10.14	5.91	1.72
	328	11.32	8.08	1.40
	338	12.57	10.86	1.16
CH_4	308	0.63	1.06	0.59
	318	0.83	1.67	0.49
	328	1.08	2.56	0.42
	338	1.37	3.82	0.36
O_2	308	2.23	8.51	0.27
	318	2.80	12.58	0.23
	328	3.46	18.15	0.20
	338	4.22	25.62	0.17
N_2	308	0.5	0.29	0.176
	318	0.65	0.44	0.15
	328	0.82	0.66	0.13
	338	1.04	0.96	0.11

PCP029

	T [K]	P [Barrer]	D [10^{-8} cm^2s^{-1}]	S [10^{-2} cm^3(STP) cm^{-3}(Polym.)$cmHg^{-1}$]
CO_2	308	10.98	5.38	2.04
	318	13.97	7.60	1.68
	328	17.51	10.50	1.40
	338	21.66	14.25	1.18
CH_4	308	0.63	1.16	0.54
	318	0.80	1.86	0.47
	328	1.00	2.89	0.40
	338	1.23	4.38	0.35
O_2	308	2.55	10.20	0.25
	318	3.21	15.26	0.22
	328	3.99	22.27	0.19
	338	4.89	31.79	0.17
N_2	308	0.52	3.86	0.13
	318	0.66	5.95	0.12
	328	0.82	8.92	0.10
	338	1.01	13.08	0.09

PCP033

	T [K]	P [Barrer]	D [10^{-8} cm^2s^{-1}]	S [10^{-2} cm^3(STP) cm^{-3}(Polym.)$cmHg^{-1}$]
CO_2	308	12.56	6.4	1.96
	318	15.04	9.19	1.64
	328	17.82	12.92	1.38
	338	20.91	17.79	1.17
CH_4	308	0.69	1.4	0.49
	318	0.97	2.28	0.43
	328	1.34	3.59	0.37
	338	1.82	5.52	0.33
O_2	308	2.69	10.76	0.25
	318	3.58	16.34	0.22
	328	4.67	24.18	0.19
	338	6.01	34.96	0.17
N_2	308	0.62	4.62	0.13
	318	0.85	7.15	0.12
	328	1.15	10.78	0.11
	338	1.52	15.87	0.10

PCP041

	T [K]	P [Barrer]	D [10^{-8} cm^2s^{-1}]	S [10^{-2} cm^3(STP) cm^{-3}(Polym.)$cmHg^{-1}$]
CO_2	308	16.5	9.76	1.69
	318	19.79	13.77	1.44
	328	23.47	19.01	1.23
	338	27.56	25.76	1.07
CH_4	308	0.87	2.19	0.40
	318	1.25	3.52	0.35
	328	1.75	5.50	0.32
	338	2.40	8.38	0.29
O_2	308	3.06	12.75	0.24
	318	4.15	19.22	0.22
	328	5.52	28.24	0.20
	338	7.23	40.58	0.18
N_2	308	0.76	6.42	0.12
	318	1.07	9.83	0.11
	328	1.47	14.67	0.10
	338	1.98	21.37	0.09

7.2.1.3 E_P, E_D and ΔH_S at 10 bar

sample	gas	E_P [kJ/mol]	E_D [kJ/mol]	ΔH_S [kJ/mol]
PC000	O_2	17.9 ± 0.6	36.3 ± 0.3	-18.4 ± 0.9
	CO_2	11.7 ± 0.3	32.8 ± 0.5	-21.2 ± 0.8
	N_2	20.9 ± 0.5	37.1 ± 0.4	-16.3 ± 0.9
	CH_4	19.3 ± 0.5	39.2 ± 0.5	-19.9 ± 1.0
PCP005	O_2	19.2 ± 0.5	34.9 ± 0.4	-15.7 ± 0.9
	CO_2	11.0 ± 0.6	31.8 ± 0.5	-20.8 ± 1.1
	N_2	19.2 ± 0.2	36.4 ± 0.6	-17.2 ± 0.8
	CH_4	19.2 ± 0.4	38.5 ± 0.7	-19.3 ± 1.1
PCP010	O_2	18.8 ± 0.4	33.8 ± 0.5	-15.0 ± 0.9
	CO_2	10.6 ± 0.6	31.0 ± 0.4	-20.4 ± 1.0
	N_2	19.2 ± 0.5	35.6 ± 0.3	-16.4 ± 0.8
	CH_4	19.3 ± 0.7	38.0 ± 0.3	-18.7 ± 1.0
PCP017	O_2	16.4 ± 0.4	30.9 ± 0.3	-14.5 ± 0.7
	CO_2	6.1 ± 0.4	28.8 ± 0.4	-22.6 ± 0.8
	N_2	19.7 ± 0.7	34.1 ± 0.3	-14.4 ± 1.0
	CH_4	19.1 ± 0.5	37.2 ± 0.4	-18.1 ± 0.9
PCP023	O_2	18.4 ± 0.5	31.8 ± 0.2	-13.4 ± 0.7
	CO_2	9.6 ± 0.5	27.2 ± 0.7	-17.6 ± 1.2
	N_2	21.0 ± 0.4	34.6 ± 0.6	-13.7 ± 1.0
	CH_4	22.5 ± 0.6	37.0 ± 0.3	-14.6 ± 0.9
PCP029	O_2	18.8 ± 0.5	32.8 ± 0.5	-11.4 ± 0.9
	CO_2	19.6 ± 0.5	28.1 ± 0.4	-15.8 ± 0.9
	N_2	19.2 ± 0.3	35.2 ± 0.5	-11.4 ± 0.8
	CH_4	19.3 ± 0.6	38.3 ± 0.5	-12.6 ± 1.1
PCP033	O_2	23.2 ± 0.4	34.0 ± 0.7	-10.8 ± 1.1
	CO_2	14.7 ± 0.4	29.5 ± 0.6	-14.8 ± 1.0
	N_2	25.8 ± 0.3	35.6 ± 0.8	-9.8 ± 1.1
	CH_4	28.0 ± 0.5	39.6 ± 0.8	-11.6 ± 1.3
PCP041	O_2	24.8 ± 0.8	33.4 ± 0.5	-8.7 ± 1.3
	CO_2	14.8 ± 0.4	28.0 ± 0.4	-13.2 ± 0.8
	N_2	27.6 ± 0.5	34.7 ± 0.3	-7.1 ± 0.8
	CH_4	29.3 ± 0.7	38.7 ± 0.3	-9.5 ± 1.0

7.2.2 PBAC-based ChloropropylPOSS Nanocomposites

The measurements are carried out in 308 K and 10bar

CO_2

Sample	P [Barrer]	D [10^{-8} cm^2s^{-1}]	S [10^{-2} cm^3(STP) cm^{-3}(Polym.)$cmHg^{-1}$]
PC000	8.98	3.00	3.04
PCC005	7.73	2.10	3.64
PCC013	7.7	2.30	3.37
PCC017	7.75	2.70	2.87
PCC023	7.93	3.20	2.45

CH_4

Sample	P [Barrer]	D [10^{-8} cm^2s^{-1}]	S [10^{-2} cm^3(STP) cm^{-3}(Polym.)$cmHg^{-1}$]
PC000	0.5	0.65	0.77
PCC005	0.47	0.63	0.75
PCC013	0.48	0.62	0.76
PCC017	0.49	0.64	0.76
PCC023	0.51	0.82	0.62

O_2

Sample	P [Barrer]	D [10^{-8} cm^2s^{-1}]	S [10^{-2} cm^3(STP) cm^{-3}(Polym.)$cmHg^{-1}$]
PC000	2.06	2.90	0.72
PCC005	1.91	3.20	0.59
PCC013	1.99	3.40	0.59
PCC017	2.03	4.04	0.50
PCC023	2.2	4.20	0.52

N_2

Sample	P [Barrer]	D [10^{-8} cm^2s^{-1}]	S [10^{-2} cm^3(STP) cm^{-3}(Polym.)$cmHg^{-1}$]
PC000	0.45	1.80	0.25
PCC005	0.39	1.40	0.28
PCC013	0.39	1.30	0.30
PCC017	0.4	1.35	0.30
PCC023	0.41	1.70	0.24

7.3 Results of Gas Sorption Measurements

7.3.1 PBAC-based PhenethylPOSS Nanocomposites (308 K)

PC000

CO_2			CH_4			N_2			O_2		
p	D	C	p	D	C	p	D	C	p	D	C
0	--	0	0	--	0	0	--	0	0	--	0
1.29	1.78	4.31	1.27	0.42	1.20	1.18	1.11	0.29	2.12	3.05	0.21
2.05	1.93	5.78	2.31	0.48	1.93	2.24	1.33	0.46	3.26	3.30	0.38
3.02	2.05	7.32	3.26	0.50	2.50	3.12	1.16	0.59	4.27	3.42	0.58
4.09	2.06	8.71	4.34	0.56	3.07	4.12	1.32	0.73	5.56	3.55	0.76
5.18	2.03	9.96	4.97	0.55	3.37	5.14	1.71	0.86	6.18	3.67	1.02
7.35	2.13	12.08	7.32	0.70	4.41	6.06	1.57	0.99	7.97	3.87	1.12
9.86	2.37	14.37	10.26	0.87	5.57	7.95	1.76	1.27	9.99	3.95	1.37
14.90	2.17	18.82	15.41	1.06	7.44	9.97	2.07	1.56	14.82	4.17	1.68
19.47	2.42	23.28	20.15	1.47	9.12	14.58	2.28	2.2	19.97	4.35	2.42
29.91	2.64	32.91	25.03	1.64	10.71	19.76	2.22	2.74	24.91	4.55	3.21
35.12	2.70	39.84	30.14	1.89	12.40	24.12	2.79	3.37	30.05	4.79	3.96
43.50	3.07	47.28	40.32	2.08	15.74	38.68	3.34	4.71	34.47	4.85	4.76
			47.1	2.25	17.94				40.38	4.96	5.52
									46.32	5.09	6.17

[p] = 1 bar, [D] = 10^{-8} cm^2s^{-1}, [c] = 1 cm^3(STP) cm^{-3}(Polym.)

PCP010

CO_2			CH_4			N_2			O_2		
p	D	C	p	D	C	p	D	C	p	D	C
0	--	0	0	--	0	0	--	0	0	--	0
1.20	1.94	2.62	1.20	0.39	0.91	1.05	0.91	0.15	1.03	3.22	0.15
2.45	2.25	4.40	2.13	0.46	1.65	2.03	1.06	0.3	2.13	3.51	0.29
3.11	2.33	5.17	3.48	0.46	2.53	2.94	1.01	0.45	3.02	3.64	0.41
4.60	2.42	6.65	4.23	0.53	3.41	4.04	1.38	0.65	3.93	3.71	0.53
5.18	2.52	7.17	5.02	0.51	3.77	4.86	1.55	0.82	5.01	3.70	0.69
6.93	2.56	8.46	7.11	0.68	4.63	7.24	1.72	1.07	6.97	3.94	0.98
8.75	2.59	9.71	9.97	0.83	4.70	9.56	2.01	1.33	9.52	4.11	1.23
10.03	2,59	10.76	14.88	0.97	6.00	14.62	2.21	1.78	14.40	4.24	1.72
14.65	2.64	13.30	19.79	1.26	7.21	18.98	2.52	2.27	19.29	4.52	2.26
19.07	2.61	16.68	29.01	1.53	9.19	28.49	2.77	3.04	27.87	4.86	3.04
28.80	2.72	24.59	38.57	1.87	11.03	39.09	3.05	3.94	38.48	5.08	4.04
38.53	2.83	33.34	45.73	2.26	12.46	49.46	3.36	5.06	45.33	5.26	4.72
47.15	3.25	36.49									

[p] = 1 bar, [D] = 10^{-8} cm^2s^{-1}, [c] = 1 cm^3(STP) cm^{-3}(Polym.)

PCP023

CO_2			CH_4			N_2			O_2		
p	D	C	p	D	C	p	D	C	p	D	C
0	--	0	0	--	0	0	--	0	0	--	0
1.52	2.14	2.15	1.24	0.31	0.77	1.16	0.70	0.09	1.27	3.06	0.1
2.51	2.59	3.29	2.11	0.41	1.32	2.04	1.35	0.19	2.00	3.15	0.18
3.24	2.84	3.61	3.42	0.49	1.76	3.45	1.67	0.31	3.17	3.42	0.27
4.26	3.01	4.45	4.63	0.55	2.24	4.27	1.98	0.39	4.30	3.64	0.39
5.32	3.21	5.20	5.49	0.61	2.45	5.22	2.15	0.47	5.30	3.92	0.49
7.51	3.21	6.60	7.41	0.73	3.36	7.16	2.24	0.71	7.21	4.26	0.69
10.47	3.50	8.23	10.14	0.91	3.928	10.42	2.44	1.00	10.23	4.59	0.89
15.24	3.63	11.25	14.93	1.06	5.14	14.67	2.63	1.42	14.89	4.88	1.26
20.06	4.09	15.08	19.67	1.34	5.98	19.85	2.88	1.98	19.37	5.06	1.70
30.13	4.24	23.84	28.55	1.74	8.10	29.00	3.05	2.84	29.11	5.32	2.74
39.96	4.54	33.16	38.55	2.04	10.19	38.72	3.37	3.74	39.62	5.42	3.98
48.17	5.06	41.03				40.20	3.33	3.97			

[p] = 1 bar, [D] = 10^{-8} cm^2s^{-1}, [c] = 1 cm^3(STP) cm^{-3}(Polym.)

PCP033

CO_2			CH_4			N_2			O_2		
p	D	C	p	D	C	p	D	C	p	D	C
0	--	0	0	--	0	0	--	0	0	--	0
1.22	4.25	2.08	1.45	0.56	0	1.09	1.75	0.06	1.27	2.64	0.07
2.16	4.47	2.80	3.27	0.80	0.58	2.10	2.40	0.14	2.00	3.92	0.14
3.00	4.81	3.44	4.09	0.91	0.91	3.04	2.63	0.23	3.17	4.24	0.2
4.01	4.86	4.21	5.18	1.06	1.23	4.01	2.78	0.31	4.30	4.52	0.27
5.25	4.92	5.17	7.31	1.14	1.55	5.21	2.89	0.41	5.30	4.88	0.37
7.28	5.28	6.72	10.11	1.29	2.11	7.32	2.93	0.58	7.21	5.12	0.55
10.01	5.44	8.81	14.24	1.57	2.95	9.82	3.38	0.77	10.23	5.34	0.77
14.52	5.88	12.26	19.74	1.98	3.9	14.65	3.52	1.12	14.89	5.60	1.09
19.56	6.33	16.12	29.26	2.51	5.13	19.56	4.19	1.50	19.37	5.81	1.36
28.77	7.14	23.17	46.18	3.27	7.04	29.13	4.59	2.19	29.11	6.23	2.19
39.23	8.23	31.18				38.80	4.96	2.83	39.62	6.54	3.28
41.90	8.54	33.22				51.08	5.40	4.24			

[p] = 1 bar, [D] = 10^{-8} cm^2s^{-1}, [c] = 1 cm^3(STP) cm^{-3}(Polym.)

PCP041

CO_2			CH_4			N_2			O_2		
p	D	C	p	D	C	p	D	C	p	D	C
0	--	0	0	--	0	0	--	0	0	--	0
1.27	6.50	1.62	1.29	0.75	0.25	1.39	3.01	0.04	1.27	3.47	0.02
2.30	7.00	2.64	2.04	0.85	0.66	2.24	2.93	0.07	2.12	3.83	0.08
3.21	7.74	3.39	3.22	1.04	0.99	3.54	3.25	0.12	3.05	4.27	0.14
4.28	8.20	4.22	4.21	1.14	1.08	4.36	3.36	0.16	4.46	4.68	0.25
5.08	8.70	4.77	5.78	1.35	1.37	5.05	3.40	0.18	5.30	4.95	0.31
7.32	9.19	6.19	7.41	1.57	1.86	7.15	3.48	0.29	8.21	5.29	0.51
10.20	9.58	7.74	10.59	1.71	2.53	9.73	3.69	0.44	9.47	5.45	0.61
15.04	10.28	10.44	14.66	1.98	3.55	14.50	3.82	0.7	14.60	5.92	0.94
20.33	11.00	13.13	19.80	2.32	4.28	19.26	4.37	0.89	18.76	6.17	1.18
30.14	11.86	20.45	28.21	2.80	5.64	29.35	4.82	1.48	28.56	6.84	2.14
38.58	12.19	26.95				38.95	5.36	2.05	38.64	7.16	2.82
47.41	12.75	34.37							42.75	7.45	3.1

[p] = 1 bar, [D] = 10^{-8} cm^2s^{-1}, [c] = 1 cm^3(STP) cm^{-3}(Polym.)

PC017			**PC029**		
	CO_2			CO_2	
p	D	C	p	D	C
0	--	0	0	--	0
1.22	1.57	2.31	1.33	3.16	3.53
2.21	2.06	3.73	2.44	3.61	5.99
3.24	2.16	4.94	3.25	3.80	7.50
4.21	2.38	5.83	4.28	4.16	9.32
5.03	2.69	6.55	5.1	4.20	10.54
7.26	2.83	8.24	7.26	4.64	13.81
9.95	2.90	10.02	9.79	4.70	17.34
14.66	2.98	13.34	14.74	5.34	24.53
19.86	3.39	16.45	18.66	5.68	29.15
28.97	3.85	23.81	29.14	6.20	44.16
38.42	4.05	30.96	38.63	6.89	56.43
45.63	4.21	36.16	45.79	7.51	66.98

[p] = 1 bar, [D] = 10^{-8} cm^2s^{-1}, [c] = 1 cm^3(STP) cm^{-3}(Polym.)

7.3.2 PS-based PhenethylPOSS Nanocomposites (308 K)

PS000

CO_2			CH_4		
p	D	C	p	D	C
0	--	0	0	--	0
1.11	1.07	1.52	1.42	0.52	0.55
2.06	2.09	2.62	2.09	0.55	0.97
3.24	2.89	3.70	3.00	0.70	1.41
4.04	3.15	4.35	5.11	0.76	1.81
5.19	3.65	5.15	9.82	0.78	2.59
7.54	3.82	6.53	14.78	0.88	3.38
9.85	4.23	7.58	19.93	0.91	4.34
14.17	4.88	8.96	28.57	1.01	5.32
19.44	6.87	10.57	38.72	1.04	6.33
28.54	8.19	12.61	46.00	1.14	7.62
37.94	10.40	14.69			
47.82	11.05	16.90			

PSP010

CO_2			CH_4		
p	D	C	p	D	C
0	--	0	0	--	0
1.05	3.23	0.81	1.06	1.25	0.33
2.18	4.26	1.89	2.18	1.37	0.60
3.06	4.51	2.73	3.31	1.46	0.88
4.10	5.03	3.48	4.48	1.53	1.18
5.37	5.43	4.27	5.12	1.59	1.32
7.05	6.08	5.47	7.85	1.67	1.87
10.58	6.82	6.67	9.93	1.71	2.21
14.82	7.50	8.28	14.96	1.86	2.90
19.56	8.73	10.01	19.48	2.13	3.63
28.37	10.42	13.34	29.30	2.36	5.43
37.81	12.92	16.57	38.5	2.70	7.38
46.14	14.66	19.79			

PSP022

CO_2			CH_4		
p	D	C	p	D	C
0	--	0	0	--	0
1.09	6.30	0.93	1.29	1.73	0.50
2.12	6.86	1.75	2.35	1.83	0.90
3.02	7.48	2.50	4.17	2.03	1.61
3.85	8.28	3.31	5.16	2.19	1.93
5.03	8.89	4.05	7.32	2.22	2.48
7.42	9.93	5.11	10.12	2.33	3.18
9.80	10.47	6.16	19.28	2.70	5.42
14.62	12.12	8.63	29.04	2.81	7.59
19.70	15.03	11.37	38.68	3.10	9.76
28.95	15.41	15.80	46.28	3.21	11.41
37.77	16.79	19.94			
46.89	18.33	24.29			

[p] = 1 bar, [D] = 10^{-8} cm^2s^{-1}, [c] = 1 cm^3(STP) cm^{-3}(Polym.)

Reference List

(1) Ishida, H.; Campbell, S.; Blackwell, J. *Chemistry of Materials* **2000**, *15,* 1260

(2) Gangopadhyay, R.; De, A. *Chemistry of Materials* **2000**, *12,* 2064

(3) Guo, L.; Yang, S.; Yang, C. *Chemistry of Materials* **2000**, *12,* 2268

(4) Tang, B. Z.; Geng, Y. H.; Lam, J. W. Y.; Li, B. S.; Jing, X. B.; Wang, X. H.; Wang, F. S.; Pakhomov, A. B.; Zhang, X. X. *Chemistry of Materials* **1999**, *11,* 1581

(5) Burnside, S. D.; Giannelis, E. P. *Chemistry of Materials* **1995**, *7,* 1597

(6) Merkel, T. C.; Freeman, B. D.; Spontak, R. J.; He, Z.; Pinnau, I.; Meakin, P.; Hill, A. J. *Science* **2002**, *296,* 519

(7) Kawashima, D.; Aihara, T.; Kobayashi, Y.; Kyotani, T.; Tomita, A. *Chemistry of Materials* **2000**, *12,* 3397

(8) Novak, B. M. *Advanced Materials* **1993**, *5,* 442

(9) Ono, Y.; Akiyama, M.; Suzuki, E. *Chemistry of Materials* **1993**, *5,* 442

(10) Joshi, M.; Butola, B. S.; Simon, G.; Kukaleva, N. *Macromolecules* **2006**, *39,* 1839

(11) Kopesky, E. T.; McKinley, G. H.; Cohen, R. E. *Polymer* **2006**, *47,* 299

(12) Kopesky, E. T.; Haddad, T. S.; McKinley, G. H.; Cohen, R. E. *Polymer* **2005**, *46,* 4743

(13) Kopesky, E. T.; Haddad, T. S.; Cohen, R. E.; McKinley, G. H. *Macromolecules* **2004**, *37,* 8992

(14) Soong, S. Y.; Cohen, R. E.; Boyce, M. C.; Mulliken, A. D. *Macromolecules* **2006**, *39,* 2900

(15) Xie, X. L.; Mai, Y. W.; Zhou, X. P. *Materials Science & Engineering R-Reports* **2005**, *49,* 89

(16) Zhao, Y. Q.; Schiraldi, D. A. *Polymer* **2005**, *46,* 11640

(17) Takahashi, S.; Paul, D. R. *Polymer* **2006**, *47,* 7519

(18) Haddad, T. S.; Lichtenhan, J. D. *Journal of Inorganic and Organometallic Polymers* **1995**, *5,* 237

(19) Joshi, M.; Butola, B. S. *Journal of Macromolecular Science-Polymer Reviews* **2004**, *C44,* 389

(20) Kopesky, E. T.; Boyes, S. G.; Treat, N.; Cohen, R. E.; McKinley, G. H. *Rheologica Acta* **2006**, *45,* 971

(21) Phillips, S. H.; Haddad, T. S.; Tomczak, S. J. *Current Opinion in Solid State & Materials Science* **2004**, *8,* 21

(22) Lichtenhan, J. D.; Schwab, J. J.; Reinerth, W. A. *Chemical Innovation* **2001**, *31,* 3

(23) Kremer, F.; Schönhals, A. In *Broadband Dielectric Relaxation Spectroscopy*,1. Ed.; Kremer, F and Schönhals, A. Eds. Verlag: Berlin, **2002**; Chapter 2, pp 35-56

(24) Schönhals, A.; Kremer, F. In *Broadband Dielectric Relaxation Spectroscopy*,1. Ed.; Kremer, F and Schönhals, A. Eds. Springer: Berlin, **2002**; Chapter 1, pp 1-32

(25) Schönhals, A.; Kremer, F. In *Broadband Dielectric Relaxation Spectroscopy*,1. Ed.; Kremer, F and Schönhals, A. Eds. Springer: Berlin, **2002**; Chapter 3, pp 59-96

(26) Schönhals, A. In *Broadband Dielectric Relaxation Spectroscopy*,1. Ed.; Kremer, F and Schönhals, A. Eds. Springer: Berlin, **2002**; Chapter 7, pp 225-286

(27) Lin, H. Q.; vanWagner, E.; Freeman, B. D.; Toy, L. G.; Gupta, R. P. *Science* **2006**, *31,* 639

(28) Merkel, T. C.; Freeman, B. D.; Spontak, R. J.; He, Z.; Pinnau, I.; Meakin, P.; Hill, A. J. *Chemistry of Materials* **2003**, *15,* 109

(29) Yampolskii, Y. P.; Korikov, A. P.; Shantarovich, V. P.; Nagai, K.; Freeman, B. D.; Masuda, T.; Teraguchi, M.; Kwak, G. *Macromolecules* **2001**, *34,* 1788

(30) Davis, S. R.; Brough, A. R.; Atkinson, A. *Journal of Non-Crystalline Solids* **2003**, *315,* 197

(31) Böhning, M.; Goering, H.; Hao, N.; Mach, R.; Schönhals, A. *Polymers for Advanced Technologies* **2005**, *16,* 262

(32) Böhning, M.; Goering, H.; Fritz, A.; Brzezinka, K. W.; Turky, G.; Schönhals, A.; Schartel, B. *Macromolecules* **2005**, *38,* 2764

(33) Heilmann, A. *Polymer Films with Embedded Metal Nanoparticles*; Springer: Berlin, **2003**

(34) Mitchell, C. A.; Bahr, J. L.; Arepalli, S.; Tour, J. M.; Krishnamoorti, R. *Macromolecules* **2002**, *35,* 8825

(35) Schmidt, G.; Malwitz, M. M. *Current Opinion in Colloid & Interface Science* **2003**, *8,* 103

(36) Blanski, R. L.; Phillips, S. H.; Lee, A. *Abstracts of Papers of the American Chemical Society* **2001**, *221,* U334

(37) Blanski, R. L.; Phillips, S. H.; Chaffee, K.; Lichtenhan, J.; Lee, A.; Geng, H. P. *Abstracts of Papers of the American Chemical Society* **2000**, *219,* U413

(38) Fina, A.; Abbenhuis, H. C. L.; Tabuani, D.; Camino, G. *Polymer Degradation and Stability* **2006**, *91,* 2275

(39) Fina, A.; Abbenhuis, H. C. L.; Tabuani, D.; Frache, A.; Camino, G. *Polymer Degradation and Stability* **2006**, *91,* 1064

(40) Fina, A.; Tabuani, D.; Carniato, F.; Frache, A.; Boccaleri, E.; Camino, G. *Thermochimica Acta* **2006**, *440,* 36

(41) Fina, A.; Tabuani, D.; Frache, A.; Camino, G. *Polymer* **2005**, *46,* 7855

(42) Hao, N., Böhning, M., Goering, H., and Schönhals, A. *Macromolecules* MA070036c

(43) Joshi, A.; Butola, B. S. *Polymer* **2004**, *45,* 4953

(44) Li, G. Z.; Wang, L.; Toghiani, H.; Daulton, T. L.; Pittman, C. U. *Polymer* **2002**, *43,* 4167

(45) Wu, C. Y.; Wicks, D. A. *Abstracts of Papers of the American Chemical Society* **2005**, *229,* U1161

(46) Zeng, J.; Kumar, S.; Iyer, S.; Schiraldi, D. A.; Gonzalez, R. I. *High Performance Polymers* **2005**, *17,* 403

(47) Scott, D. W. *Journal of the American Chemical Society* **1946**, *68,* 356

(48) Pracella, M.; Chionna, D.; Fina, A.; Tabuani, D.; Frache, A.; Camino, G. *Macromolecular Symposia* **2006**, *234,* 59

(49) Fu, B. X.; Yang, L.; Somani, R. H.; Zong, S. X.; Hsiao, B. S.; Phillips, S.; Blanski, R.; Ruth, P. *Journal of Polymer Science Part B-Polymer Physics* **2001**, *39,* 2727

(50) Schiraldi, D.; Iyer, S.; Somlai, A. P.; Zeng, J. J.; Kumar, S.; Bennett, C.; Jarrett, W. L.; Mathias, L. J. *Abstracts of Papers of the American Chemical Society* **2004**, *227,* U473

(51) Schiraldi, D.; Zeng, J. J.; Kumar, S.; Iyer, S.; Dong, F. *Abstracts of Papers of the American Chemical Society* **2003**, *225,* U59

(52) Lee, L. H.; Chen, W. C. *Polymer* **2005**, *46,* 2163

(53) Capaldi, F. M.; Rutledge, G. C.; Boyce, M. C. *Macromolecules* **2005**, *38,* 6700

(54) Sperling, L. H. *Physical Polymer Science*; John Wiley & Sons: New York, **1986**

(55) Hodge, I. M. *Journal of Non-Crystalline Solids* **1994**, *169,* 211

(56) Gehlsen, M. D.; Bates, F. S. *Macromolecules* **1993**, *26,* 4122

(57) Demoulin, C.; Montrose, C. J.; Ostrowsk, N. *Physical Review A* **1974**, *9,* 1740

(58) Mezei, F.; Knaak, W.; Farago, B. *Physical Review Letters* **1987**, *58,* 571

(59) Boehmer, R.; Kremer, F. In *Broadband Dielectric Relaxation Spectroscopy*,1. Ed.; Kremer, F and Schönhals, A. Eds. Springer: Berlin, **2002**; Chapter 17, pp 225-286

(60) Vogel, H. *Physikalische Zeitschrift* **1921**, *22,* 645

(61) Fulcher, G. S. *Journal of the American Ceramic Society* **1925**, *8,* 339

(62) Tammann, G.; Hesse, W. *Zeitschrift fur Anorganische und Allgemeine Chemie* **1926**, *156,* 245

(63) Kovacs, A. J. *Journal of Polymer Science* **1958**, *30,* 131

(64) Kremer, F.; Schönhals, A. In *Broadband Dielectric Relaxation Spectroscopy*,1. Ed.; Kremer, F and Schönhals, A. Eds. Verlag: Berlin, **2002**; Chapter 4, pp 99-129

(65) Eyring, H. *Journal of Chemical Physics* **1936**, *4,* 283

(66) Doolittle, A. K. *Journal of Applied Physics* **1951**, *22,* 1471

(67) Cohen, M. H.; Turnbull, D. *Journal of Chemical Physics* **1959**, *31,* 1164

(68) Fox, T. G.; Flory, P. J. *Journal of Polymer Science* **1954**, *14,* 315

(69) Fox, T. G.; Flory, P. J. *Journal of Applied Physics* **1950**, *21,* 581

(70) Donth, E. *Journal of Non-Crystalline Solids* **1982**, *53,* 325

(71) Stillinger, F. H. *Science* **1995**, *267,* 1935

(72) Leutheuser, E. *Physical Review A* **1984**, *29,* 2765

(73) Kivelson, D.; Kivelson, S. A.; Zhao, X. L.; Nussinov, Z.; Tarjus, G. *Physica A* **1995**, *219,* 27

(74) Onsager, L. *Journal of the American Chemical Society* **1936**, *58,* 1486

(75) Kirkwood, J. G. *Transactions of the Faraday Society* **1946**, *42A,* 7

(76) Fröhlich, H. *Theory of dielectrics*; Oxford University Press: London, **1958**

(77) Landau, L. D.; Lifschitz, E. M. *Textbook of Theoretical Physics*; Akademie-Verlag: Berlin, **1997**

(78) Debye, P. *Polar Molecules*; the Chemical Catalog Co. Inc.: New York, **1929**

(79) Kramers, H. A. *Nature* **1924**, *114,* 310

(80) Kronig, R. D. L. *Journal of the Optical Society of America and Review of Scientific Instruments* **1926**, *12,* 547

(81) Callen, H. B.; Welton, T. A. *Physical Review* **1951**, *83,* 34

(82) Cole, K. S.; Cole, R. H. *Journal of Chemical Physics* **1941**, *9,* 341

(83) Davidson, D. W.; Cole, R. H. *Journal of Chemical Physics* **1950**, *18,* 1417

(84) Jonscher, A. K. *Dielectric Relaxation in Solids*; Chelsea Dielectric Press: London, **1983**

(85) Havriliak, S.; Negami, S. *Polymer* **1967**, *8,* 161

(86) Havriliak, S.; Negami, S. *Polymer* **1969**, *10,* 859

(87) Havriliak, S.; Negami, S. *Journal of Polymer Science Part C-Polymer Symposium* **1966**, 99

(88) Steeman, P. A. M.; van Turnhout, J. In *Broadband Dielectric Relaxation Spectroscopy*,1. Ed.; Kremer, F and Schönhals, A. Eds. Springer: Berlin, **2002**; Chapter 13, pp 495-520

(89) Steeman, P. A. M.; Maurer, F. H. J.; Vanes, M. A. *Polymer* **1991**, *32,* 523

(90) Steeman, P. A. M.; Maurer, F. H. J. *Colloid and Polymer Science* **1990**, *268,* 315

(91) Wagner, R. W. *Arch.Elekrotech.* **1914**, *2,* 371

(92) Kharadly, M. M. Z.; Jackson, W. *Proceedings of the Institution of Electrical Engineers-London* **1953**, *100,* 199

(93) Dryden, J. S.; Meakins, R. J. *Discussions of the Faraday Society* **1957**, 39

(94) Fricke, H. *Journal of Physical Chemistry* **1954**, *57,* 934

(95) Bruggeman, D. A. G. *Annalen der Physik* **1935**, *24,* 636

(96) Hanai, T. *Kolloid-Zeitschrift and Zeitschrift fur Polymere* **1960**, *171,* 23

(97) Boned, C.; Peyrelasse, J. *Colloid and Polymer Science* **1983**, *261,* 600

(98) Mulder, M. *Basic Principles of Membrane Technology*; Kluweer Academic Publishers: Amsterdam, **1996**

(99) Graham, T. *Philos.Trans.Roy.Soc.* **1861**, *151,* 183

(100) Barrer, R. M. *Journal of the Chemical Society* **1934**, 378

(101) Barrer, R. M. *Journal of Physical Chemistry* **1957**, *61,* 178

(102) Fick, A. *Journal of Membrane Science* **1995**, *100,* 33

(103) Crank, J. *the Mathematics of Diffusion*; Clarendon Press: Oxford, **1975**

(104) Paul, D. R.; Koros, W. J. *Journal of Polymer Science Part B-Polymer Physics* **1976**, *14,* 675

(105) Koros, W. J.; Paul, D. R.; Rocha, A. A. *Journal of Polymer Science Part B-Polymer Physics* **1976**, *14,* 687

(106) Fujita, H.; Kishimoto, A. *Journal of Chemical Physics* **1961**, *34,* 393

(107) Comyn, J. *Polymer Permeability*; Elservier: Amsterdam, **1985**

(108) Crank, J.; Park, G. *Diffusion in Polymers*; Clarendon Press: Oxford, **1968**

(109) Barrer, R. M. *Nature* **1937**, *140,* 106

(110) Kumins, C. A.; Kwei, T. K. In *Diffusion in Polymers*. Ed.; Crank, J and Park, GS Eds. Academic Press: London, New York, **1968**

(111) Brandt, W. W. *Journal of Physical Chemistry* **1959**, *63,* 1080

(112) Dibenedetto, A. T.; Paul, D. R. *Journal of Polymer Science Part A-General Papers* **1964**, *2,* 1001

(113) Pace, R. J.; Datyner, A. *Polymer Engineering and Science* **1980**, *20,* 51

(114) Pace, R. J.; Datyner, A. *Journal of Polymer Science Part B-Polymer Physics* **1979**, *17,* 1675

(115) Pace, R. J.; Datyner, A. *Journal of Polymer Science Part B-Polymer Physics* **1979**, *17,* 1693

(116) Pace, R. J.; Datyner, A. *Journal of Polymer Science Part B-Polymer Physics* **1979**, *17,* 437

(117) Stern, S. A.; Trohalaki, S. *Acs Symposium Series* **1990**, *423,* 22

(118) Hofmann, D.; Fritz, L.; Ulbrich, J.; Schepers, C.; Böhning, M. *Macromolecular Theory and Simulations* **2000**, *9,* 293

(119) Pant, P. V. K.; Boyd, R. H. *Macromolecules* **1993**, *26,* 679

(120) Pant, P. V. K.; Boyd, R. H. *Macromolecules* **1992**, *25,* 494

(121) Sok, R. M.; Berendsen, H. J. C. *Abstracts of Papers of the American Chemical Society* **1992**, *203,* 619

(122) Hölck, O.; Siegert, M. R.; Heuchel, M.; Böhning, M. *Macromolecules* **2006**, *39,* 9590

(123) Barrie, J. A.; Williams, M. J. L.; Munday, K. *Polymer Engineering and Science* **1980**, *20,* 20

(124) Barrer, R. M.; Barrie, J. A. *Journal of Polymer Science* **1958**, *28,* 377

(125) Barrer, R. M.; Barrie, J. A.; Slater, J. *Journal of Polymer Science* **1958**, *27,* 177

(126) Vieth, W. R.; Sladek, K. J. *Journal of Colloid Science* **1965**, *20,* 1014

(127) Paul, D. R. *Berichte der Bunsen-Gesellschaft-Physical Chemistry Chemical Physics* **1979**, *83,* 294

(128) Uragami, T.; Hopfenberg, H. B.; Koros, W. J.; Yang, D. K.; Stannett, V. T.; Chern, R. T. *Journal of Polymer Science Part B-Polymer Physics* **1986**, *24,* 779

(129) Aminabhavi, T. M.; Cassidy, P. E.; Biradar, N. S. *Journal of Macromolecular Science-Reviews in Macromolecular Chemistry and Physics* **1987**, *C27,* 459

(130) Cain, E. J.; Wen, W. Y.; Jones, A. A.; Inglefield, P. T.; Cauley, B. J.; Bendler, J. T. *Journal of Polymer Science Part B-Polymer Physics* **1991**, *29,* 1009

(131) Bandis, A.; Cauley, B. J.; Inglefield, C. E.; Wen, W. Y.; Inglefield, P. T.; Jones, A. A.; Melcuk, A. *Journal of Polymer Science Part B-Polymer Physics* **1993**, *31,* 447

(132) Sefcik, M. D.; Schaefer, J.; May, F. L.; Raucher, D.; Dub, S. M. *Journal of Polymer Science Part B-Polymer Physics* **1983**, *21,* 1041

(133) Sefcik, M. D.; Schaefer, J. *Journal of Polymer Science Part B-Polymer Physics* **1983**, *21,* 1055

(134) Brolly, J. B.; Bower, D. I.; Ward, I. M. *Journal of Polymer Science Part B-Polymer Physics* **1996**, *34,* 761

(135) Brolly, J. B.; Bower, D. I.; Ward, I. M. *Journal of Polymer Science Part B-Polymer Physics* **1996**, *34,* 769

(136) Petropoulos, J. H. *Journal of Polymer Science Part A-2-Polymer Physics* **1970**, *8,* 1797

(137) Petropoulos, J. H.; Roussis, P. P. *Journal of Polymer Science Part A-2-Polymer Physics* **1970**, *8,* 1411

(138) Fredrickson, G. H.; Helfand, E. *Macromolecules* **1985**, *18,* 2201

(139) Stern, S. A.; Saxena, V. *Journal of Membrane Science* **1980**, *7,* 47

(140) Costello, L. M.; Koros, W. J. *Industrial & Engineering Chemistry Research* **1993**, *32,* 2277

(141) Meares, P. *Transactions of the Faraday Society* **1958**, *54,* 40

(142) Meares, P. *Journal of the American Chemical Society* **1954**, *76,* 3415

(143) Schaumburg, G. *Dielectric Newsletter* **1994**, *March,* 1

(144) Schaumburg, G. *Dielectric Newsletter* **1999**, *May,* 1

(145) Collin, R. E. *Fundations for Microwave Engineering*; McGraw-Hill: New York, **1996**

(146) Böhning, M.; Springer, J. *Polymer* **1998**, *39,* 5183

(147) Holck, O.; Siegert, M. R.; Heuchel, M.; Bohning, M. *Macromolecules* **2006**, *39,* 9590

(148) Berens, A. R.; Hopfenberg, H. B. *Polymer* **1978**, *19,* 498

(149) Holck, O.; Siegert, M. R.; Heuchel, M.; Bohning, M. *Macromolecules* **2006**, *39,* 9590

(150) Rikowski, E.; Marsmann, H. C. *Polyhedron* **1997**, *16,* 3357

(151) Mikhailkov, G. P.; Eidelnant, M. P. *Vysokomolekul.Soedin.* **1960**, *2,* 1772

(152) Illers, K. H.; Breuer, H. *Journal of Colloid Science* **1963**, *18,* 1

(153) Krum, F.; Muller, F. H. *Kolloid-Zeitschrift and Zeitschrift fur Polymere* **1959**, *164,* 81

(154) Schnell, H. *Angewandte Chemie-International Edition* **1956**, *68,* 633

(155) Pratt, G. J.; Smith, M. J. A. *Polymer International* **1996**, *40,* 239

(156) Matsuoka, S.; Ishida, Y. *Journal of Polymer Science Part C-Polymer Symposium* **1966**, 247

(157) Watts, D. C.; Perry, E. P. *Polymer* **1978**, *19,* 248

(158) Pratt, G. J.; Smith, M. J. A. *British Polymer Journal* **1986**, *18,* 105

(159) Pratt, G. J.; Smith, M. J. A. *Polymer International* **1997**, *43,* 137

(160) Pochan, J. M.; Gibson, H. W.; Froix, M. F.; Hinman, D. F. *Macromolecules* **1978**, *11,* 165

(161) Pochan, J. M.; Hinman, D. F.; Turner, S. R. *Journal of Applied Physics* **1976**, *47,* 4245

(162) Aoki, Y.; Brittain, J. O. *Journal of Applied Polymer Science* **1976**, *20,* 2879

(163) Aoki, Y.; Brittain, J. O. *Journal of Polymer Science Part B-Polymer Physics* **1976**, *14,* 1297

(164) Kochi, M.; Sasaki, T.; Kambe, H. *Polymer Journal* **1978**, *10,* 169

(165) Legrand, D. G.; Erhardt, P. F. *Journal of Applied Polymer Science* **1969**, *13,* 1707

(166) Carius, H. E.; Schönhals, A.; Guigner, D.; Sterzynski, T.; Brostow, W. *Macromolecules* **1996**, *29,* 5017

(167) Heijboer, J. *Journal of Polymer Science Part C-Polymer Symposium* **1968**, 3755

(168) Bauwenscrowet, C.; Bauwens, J. C. *Journal of Materials Science* **1979**, *14,* 1817

(169) Allen, G.; Mcainsh, J.; Jeffs, G. M. *Polymer* **1971**, *12,* 85

(170) Merenga, A. S.; Papadakis, C. M.; Kremer, F.; Liu, J.; Yee, A. F. *Macromolecules* **2001**, *34,* 76

(171) Golden, J. H.; Hammant, B. L.; Hazell, E. A. *Journal of Applied Polymer Science* **1967**, *11,* 1571

(172) Locati, G.; Tobolsky, A. V. *Advances in Molecular Relaxation Processes* **1970**, *1,* 375

(173) Pochan, J. M.; Gibson, H. W.; Pochan, D. L. F. *Macromolecules* **1982**, *15,* 1368

(174) Mehendru, P. C.; Jain, K.; Agarwal, J. P. *Journal of Physics D-Applied Physics* **1980**, *13,* 1497

(175) Linkens, A.; Vanderschueren, J. *Journal of Polymer Science Part C-Polymer Letters* **1977**, *15,* 41

(176) Aoki, Y.; Brittain, J. O. *Journal of Polymer Science Part B-Polymer Physics* **1977**, *15,* 199

(177) Nielsen, L. E. *Mechanical Properties of Polymers*; Reinhold: New York, **2007**

(178) Ito, E. *Journal of Polymer Science Part B-Polymer Physics* **1974**, *12,* 1477

(179) Floudas, G.; Higgins, J. S.; Meier, G.; Kremer, F.; Fischer, E. W. *Macromolecules* **1993**, *26,* 1676

(180) Alegria, A.; Mitxelena, O.; Colmenero, J. *Macromolecules* **2006**, *39,* 2691

(181) Sacher, E. *Journal of Macromolecular Science-Physics* **1975**, *B 11,* 403

(182) Sacher, E. *Journal of Macromolecular Science-Physics* **1974**, *B 10,* 319

(183) Sacher, E. *Journal of Macromolecular Science-Physics* **1974**, *B 9,* 163

(184) Chung, C. I.; Sauer, J. A. *Journal of Polymer Science Part A-2-Polymer Physics* **1971**, *9,* 1097

(185) Reding, F. P.; Whitman, R. D.; Faucher, J. A. *Journal of Polymer Science* **1961**, *54,* S56

(186) Sikka, S. *Polymer Bulletin* **1980**, *3,* 61

(187) Ito, E.; Hatakeyama, T. *Journal of Polymer Science Part B-Polymer Physics* **1975**, *13,* 2313

(188) Szwarc, M. *Nature* **1956**, *178,* 1168

(189) Cowie, J. M. G. *Polymers : Chemistry and Physics of Modern Materials*; CRC Press: London, **1991**

(190) von Hipper, A. R. *Dielectric Materials and Applications*; Artech House Publishers: MA, USA, **1995**

(191) Saito S; Nakajima T *Journal of Applied Polymer Science* **1959**, *2,* 93

(192) Sauer, J. A.; Kline, D. E. *Journal of Polymer Science* **1955**, *18,* 491

(193) Buchdahl, R.; Nielsen, L. E. *Journal of Polymer Science* **1955**, *15,* 1

(194) Baker, E. B.; Auty, R. P.; Ritenour, G. J. *Journal of Chemical Physics* **1953**, *21,* 159

(195) Illers, K. H.; Jenkel, E. *Rheologica Acta* **1958**, *1,*

(196) Tseng, C. R.; Wu, J. Y.; Lee, H. Y.; Chang, F. C. *Journal of Applied Polymer Science* **2002**, *85,* 1370

(197) Zhang, J. Z.; Wang, X.; Lu, L. D.; Li, D.; Yang, X. J. *Journal of Applied Polymer Science* **2003**, *87,* 381

(198) Kim, K. J.; White, J. L. *Polymer Engineering and Science* **1999**, *39,* 2189

(199) Li, G.; Mai, K. C.; Feng, K. C. *Journal of Applied Polymer Science* **2006**, *99,* 2138

(200) Yu, J.; Yu, J.; Guo, Z. X.; Gao, Y. F. *Macromolecular Rapid Communications* **2001**, *22,* 1261

(201) Hsiue, G. H.; Kuo, W. J.; Huang, Y. P.; Jeng, R. J. *Polymer* **2000**, *41,* 2813

(202) Ma, C. C. M.; Chen, Y. J.; Kuan, H. C. *Journal of Applied Polymer Science* **2006**, *100,* 508

(203) Vyazovkin, S.; Dranca, I.; Fan, X. W.; Advincula, R. *Journal of Physical Chemistry B* **2004**, *108,* 11672

(204) Bos, A.; Punt, I. G. M.; Wessling, M.; Strathmann, H. *Journal of Membrane Science* **1999**, *155,* 67

(205) Chen, S. H.; Lin, S. S.; Chang, D. J.; Chang, J. S. *Journal of Applied Polymer Science* **2000**, *77,* 89

(206) Dechant, J. *Ultrarotspektroskopische Untersuchungen an Polymeren*; Akademie-Verlag: **1972**

(207) Huang, X. B.; Ouyang, X. Y.; Ning, F. L.; Wang, J. Q. *Polymer Degradation and Stability* **2006**, *91,* 606

(208) Xiao, C.; Wu, J.; Yang, L.; Yee, A. F.; Xie, L.; Gidley, D.; Ngai, K. L.; Rizos, A. K. *Macromolecules* **1999**, *32,* 7913

(209) Breck, R. R. *Zeolite Molecular Sieves*; John Wiley & Sons: New York, **1974**

(210) Powell, C. E.; Qiao, G. G. *Journal of Membrane Science* **2006**, *279,* 1

(211) Sanders, E. S. *Journal of Membrane Science* **1988**, *37,* 63

(212) Ismail, A. F.; Lorna, W. *Separation and Purification Technology* **2002**, *27,* 173

(213) Norton, F. J. *Journal of Applied Polymer Science* **1963**, *7,* 1649

(214) Barrer, R. M.; Skirrow, G. *Journal of Polymer Science* **1948**, *3,* 564

(215) Barrer, R. M.; Skirrow, G. *Journal of Polymer Science* **1948**, *3,* 549

Curriculum Vita

Personal:

Name:	Hao, Ning
Date of Birth:	April 22. 1978
Place of Birth:	Beijing, P. R. China
Nationality:	Chinese

Education:

09/1993 – 07/1996	No. 55 Middle School of Beijing, Beijing, China
07/1996	National College Entrance Examination
09/1996 – 07/2000	Department of Material Science and Engineering, Beijing University of Chemical Technology, Beijing, China
07/2000	Bachelor Degree of Polymer/Composite Engineering
02/2001 – 07/2003	Joint Master Program of Polymer Science, Free University of Berlin, Berlin, Germany
07/2003	Master Degree of Polymer Science
08/2003 – Present	Ph. D. Research in Federal Institute of Materials Research and Testing (BAM), Berlin, Germany